

A MULTI-SCALE, MULTI-CONTINUUM AND MULTI-PHYSICS MODEL TO
SIMULATE COUPLED FLUID FLOW AND GEOMECHANICS
IN SHALE GAS RESERVOIRS

Cong Wang

November 2017

© Copyright 2017

by

Cong Wang

A thesis submitted to the Faculty and the Board of Trustees of the Colorado School of Mines in partial fulfillment of the requirements for the degree of Doctor Philosophy (Petroleum Engineering).

Golden, Colorado

Date _____

Signed: _____

Cong Wang

Signed: _____

Dr. Yu-Shu Wu
Thesis Advisor

Golden, Colorado

Date _____

Signed: _____

Dr. Erdal Ozkan
Professor and Department
Head of Petroleum Engineering

ABSTRACT

In this study, several efficient and accurate numerical solutions to unconventional reservoir development problems are developed. The first is the three-dimensional embedded discrete fracture method (3D-EDFM), which is able to simulate fluid flow with multiple 3D hydraulic fractures with arbitrary strike and dip angles, shapes, curvatures, conductivities and connections. The second is a multi-porosity and multi-physics fluid flow model, which can capture gas flow behaviors in shales complicated by highly heterogeneous and hierarchical rock structures (ranges from organic nanopores, inorganic nanopores, less permeable micro-fractures, more permeable macro-fractures to hydraulic fractures). The third is iterative numerical approach combining X-FEM and EDFM, which is developed for simulating the fluid-driven fracture propagation process in porous media.

Physical explanations and mathematical equations behind these numerical approaches are described in detail. Their advantages over alternative numerical methods are discussed. These numerical methods are incorporated into the in-house program through coding efforts. A series of synthetic but realistic cases are simulated. Simulated results meet our physical understandings qualitatively and match with available analytical solutions quantitatively. These novel computational mechanics solutions provide numerical approaches to understand complicated physical phenomena in developing unconventional reservoirs, thus they help in the better management of unconventional reservoirs.

TABLE OF CONTENTS

ABSTRACT.....	III
LIST OF FIGURES	VII
LIST OF TABLES.....	XI
ACKNOWLEDGEMENTS.....	X
CHAPTER 1 INTRODUCTION	2
CHAPTER 2 A GENERAL THREE-DIMENSIONAL EMBEDDED DISCRETE FRACTURE METHOD FOR RESERVOIR SIMULATION WITH COMPLICATED HYDRAULIC FRACTURES	6
2.1 Introduction.....	7
2.2 Governing Equations	10
2.3 Geometric Property Calculation	12
2.3.1 Connection Area	12
2.3.2 Connection Distances.....	17
2.3.3 Infinite and Finite Conductivity Fracture	20
2.3.4 Multiple Connected Fractures.....	21
2.4 Analytical Solutions for 1D Fluid Flow with a Fracture	23
2.4.1 General Analytical Solutions for 1D Fluid Flow with a Fracture.....	23
2.4.2 Steady or Pseudo-Steady State Analytical Solution	28
2.5 Model Validation	30
2.5.1 Single Fracture	31
2.5.2 Multiple Fractures.....	34
2.5.3 3D Circular Fracture	36
2.6 Application.....	38
2.6.1 The Multi-Layer Case	39

2.6.2 The Stress Shadow Case	41
2.6.3 The Natural Fracture Interaction Case	43
2.7 Summary	49
CHAPTER 3 A MULTI-POROSITY, MULTI-PHYSICS MODEL TO SIMULATE FLUID FLOW IN NUNCONVENTIONAL RESERVOIRS	51
3.1 Introduction.....	52
3.2 Various Fluid Flow Physics	55
3.2.1 Gas Slippage Effect.....	55
3.2.2 Gas Adsorption and Desorption.....	59
3.2.3 Non-Darcy Flow	60
3.3 Model Conceptualization	60
3.4 Mathematics and Numerical Method.....	62
3.4.1 Key Parameters for Fluid Flow among Various Continua	64
3.4.2 Fluid Flow Parameters Between Organic and Inorganic Matter	65
3.4.3 Governing Equations for Multiple Fluid Flow Physics	69
3.5 Model Applications.....	71
3.6 Summary	74
CHAPTER 4 COUPLED NUMERICAL APPROACH COMBINING X-FEM AND EDFM FOR THE FLUID-DRIVEN FRACTURE PROPAGATION PROCESS IN POROUS MEDIA	76
4.1 Introduction.....	76
4.2 Governing Equations and Numerical Formulations	80
4.3 The Coupling Principles	85
4.3.1 Solid Deformation on Fluid flow	86
4.3.2 Fluid Flow on Solid Deformation	88
4.3.3 Solid Deformation on Fracture Propagation	89

4.3.4 Fracture Propagation on Solid Deformation and Fluid Flow.....	90
4.3.5 Numerical Coupling Procedures	91
4.4 Validations	94
4.4.1 Solid Deformation Model Validations.....	95
4.4.2 Fluid Flow Model Validations	96
4.5 Numerical Results.....	98
4.5.1 Two Dimensional KGD Model.....	98
4.5.2 Three-Dimensional Penny-Shaped Fracture Model.....	102
4.6 Summary	109
LIST OF SYMBOLS	111
REFERENCES CITED.....	118
APPENDIX A: THE CODE STRUCTURE OF THE EDFM AND X-FEM COUPLING	128

LIST OF FIGURES

Figure 2-1 Schematic of the full intersection between a box and a fracture plane, leading to a polygon with 3 to 6 vertices	12
Figure 2-2 Flowchart to calculate 3D box and plane intersections.....	14
Figure 2-3 Point is inside the rectangle if and only if the sum of areas of four triangles equals to the rectangle area.....	15
Figure 2-4 Sort vertices in a clockwise order based on the direction angle between them and the central point.....	17
Figure 2-5 Demonstration of a 1D reservoir under production via a fracture with constant pressures	18
Figure 2-6 Ratio of two average distances with time for two different matrix permeability (1.0 mD and 0.01 mD) and three different matrix-block sizes (1m, 5m, and 10m)	20
Figure 2-7 Demonstrations of different numerical methods to handle infinite-conductivity fracture (left) and finite-conductivity fracture (right)	21
Figure 2-8 upper left: a 2D synthetic problem with two matrix blocks and three intersected fractures. Right: Numerical idealization for this problem, which includes two matrix elements and two fracture elements; Lower left: distance contour for matrix-fracture connections	22
Figure 2-9 Vertical fracture in an infinite slab reservoir	31
Figure 2-10 Comparisons of wellbore pressure vs. time between the analytical solution (“Cinco-Samaniego” type curve), and numerical solution with various fracture conductivities	33
Figure 2-11 Comparisons of wellbore pressure vs. time between the analytical solution, and numerical solution with various grid sizes for infinite fracture conductivity	33
Figure 2-12 Cases with various fracture directions and their associated EDFM grids (0, 15 and 30 degrees)	34

Figure 2-13 Comparisons of wellbore pressure vs. time between the analytical solution, and numerical solution with various fracture orientation for infinite fracture conductivity	34
Figure 2-14 Synthetic 2D model with 4 fracture branches	35
Figure 2-15 Space discretization for three different fracture simulation methods (from left to right: LGR, triangular grids, and EDFM).....	35
Figure 2-16 Oil production rate results for three solutions for synthetic 2D flow	35
Figure 2-17 Comparison of Jacobian matrix size and complexity of these three approaches (from left to right: LGR, triangular grids, and EDFM)	36
Figure 2-18 Space discretization for the 3D circular fracture (left: LGR methods, right: EDFM)	
37	
Figure 2-19 Simulated bottle hole pressure vs. time with LGR and EDFM methods	38
Figure 2-20 3D contour (a quarter view) of pressure change at 2,065s.....	38
Figure 2-21 Left: Illustrations of a hydraulic fracture with complicated shapes from geomechanics simulations. Three layers are selected to demonstrate our simulated flow patterns inside the reservoir. Right: Discretization grids for the reservoir and the embedded fracture	39
Figure 2-22 The lateral (y-z) view of the pressure distribution inside the fracture at 1.0 day	40
Figure 2-23 The top (x-y) view of contour lines of pressure for these three layers at 10.0 days .	41
Figure 2-24 left: Illustrations of four curved hydraulic fractures due to the stress shadow effect. right: Discretization grids for the reservoir and the embedded fractures	42
Figure 2-25 The top (x-y) view of the pressure distribution at 1.0 day and 1.0 month	42
Figure 2-26 Three DFN geometries (left) and corresponding 3D-EDFM grids (right).....	44
Figure 2-27 Horizontal slices of simulated pressure contours for case 1 at 1038s (left) and 12,960s (right)	46
Figure 2-28 Simulated production rate vs. time (log-log scale) for these three cases	46
Figure 2-29 Simulated area-normalized production rate vs. time (log-log scale)	47

Figure 2-30 Relative permeability and capillary pressure for two-phase flow simulation.....	48
Figure 2-31 Water saturation profiles after one-week well shut-in	48
Figure 2-32 Simulated gas production rate vs. time	49
Figure 2-33 Simulated cumulative water production vs. time	49
Figure 3-1 Multi-scale illustration of conventional reservoirs: gas flow network is relatively uniform and homogeneous inorganic porous medium	53
Figure 3-2 Multi-scale illustration of unconventional reservoirs: gas flow network includes hydraulic fracture, macro-scale natural fractures, micro-scale natural fractures, organic porous medium, and inorganic porous medium	54
Figure 3-3 Quantification of gas flow regimes in unconventional reservoir fractures, conventional reservoir pores, and unconventional reservoir pores based on microfluidics theory	59
Figure 3-4. (a) General fracture network, organic and inorganic matter in shale rocks based on statistical distributions of fracture and porous medium properties, conceptualized from SEM image. (b) The disintegration of the complicated and hierarchical shale rock structure into multiple components (from left to right: natural fractures, micro fractures, organic matter, and inorganic matter). (c) Idealization of each component using the average approach by capturing the key flow characteristics. (d) Recombination of the idealized components for numerical simulation	61
Figure 3-5 Conceptualization of global domain flow and local domain interactions among different geological constituents	62
Figure 3-6 Conceptualization of fluid flow between organic and inorganic matter	65
Figure 3-7 The reservoir model schematic and the mesh for simulation.....	72
Figure 3-8 Comparisons of the normalized gas production rate for these three models	74
Figure 3-9 Simulated pressure contours after one-year production for four continua in the multi-porosity and multi-physics model	74
Figure 4-1 Three strong coupling processes during the fluid-driven fracture propagations in porous media	77

Figure 4-2 Interactions among fluid flow, solid deformation and fracture growth	86
Figure 4-3 Sketch diagram for a two-dimensional body	87
Figure 4-4 The path and discretization nodes of a fracture before (left) and after (right) fracture propagation	91
Figure 4-5 A three-dimensional circular fracture (left), its representations by the EDFM (mid) and by the X-FEM (right).....	91
Figure 4-6 Average fracture width as a function of the iteration number with Picard coefficient equals to 0.5 and 1.0.....	93
Figure 4-7 The workflow of a two-stage coupling method for fluid flow, solid deformation and fracture growth simulation	94
Figure 4-8 Plane with a center fracture at angle β and simulated shear stress contours.....	95
Figure 4-9 Comparisons between numerical and analytical stress intensity factor	96
Figure 4-10 Plane with a centered fracture with angle β and simulated pressure contour after one minute of production	97
Figure 4-11 Comparisons between numerical and analytical dimensionless pressure	97
Figure 4-12 Illustration of a KGD model (left modified from Lisjak et al. 2015)) and its numerical setup in this study (right).....	98
Figure 4-13 Comparisons of the propagated fracture radius vs. time between the analytical solution and the numerical solution for the KGD fracture model	100
Figure 4-14 Comparisons of the fracture width at inlet vs. time between the analytical solution and the numerical solution for the KGD fracture model.....	101
Figure 4-15 Comparisons of the net pressure at inlet vs. time between the analytical solution and the numerical solution for the KGD fracture model.....	101
Figure 4-16 From left to right (contours of the normal stress in the x-direction, the normal stress in the y-direction and shear stress) when fracture length is 1.2m	102
Figure 4-17 Fracture geometry (half-width vs. length) at injection time of 2.5s, 5s and 10s....	102

Figure 4-18 Illustration of a 3D penny-shaped fracture (Lisjak et al. 2015) and associated modeling representations.....	103
Figure 4-19 Simulated fracture width distributions at six minutes and 16 minutes	105
Figure 4-20 Comparisons of the propagated fracture radius vs. time between the analytical solution and the numerical solution with various fracture toughness	105
Figure 4-21 Simulated fracture radius vs. time with various reservoir permeabilities	106
Figure 4-22 Simulated fracture geometry	107
Figure 4-23 Contours of fluid pressure at four horizontal layers.....	108
Figure 4-24 Contours of xx-normal stress at four horizontal layers	108
Figure 4-25 Contours of xy-shear stress at four horizontal layers.....	109

LIST OF TABLES

Table 2-1 Synthetic model parameters for numerical model validations	32
Table 2-2 Comparison of problem size and simulation times for these three approaches	36
Table 2-3 Information of the fracture geometry and EDFM gridding for these three cases	45
Table 3-1 Estimations of key parameters to determine gas flow regimes in unconventional reservoir fractures, unconventional pores, and conventional reservoir pores	58
Table 3-2 The contact interface and characteristic distances for these four connections	65
Table 3-3 Physical properties for different geological features.....	72
Table 4-1 Data in the KGD model.....	99
Table 4-2 Input parameters for the 3D penny-shaped fracture modeling.....	103

ACKNOWLEDGEMENTS

First of all, I would like to thank my supervisor, Dr. Yu-Shu Wu, who has been very patient with me throughout all these years. He led me into the fascinating world of reservoir simulation and offered me a great research platform to work on. With his guidance, I have learned the essentials of how to be a good researcher. I am grateful to him not only for his thoughtful guidance on my academic research, but also for his caring of my life. All these achievements are not possible without his support, inspirations and encouragements.

My sincere thanks also go to the rest of my committee members: Dr. Azra Tutuncu, Dr. D.V. Griffiths, Dr. Didier Yu Ding, Dr. Philip Winterfeld and Dr. Steve Sonnenberg, for reading drafts of this dissertation and providing many valuable suggestions and comments. What I learned from their courses, books and published journals are essentially valuable for completing this dissertation.

This work is supported by several funding agencies. Special acknowledgements are due to the EMG and UNGI Research Center in Colorado School of Mines, Foundation CMG and CNPC-USA, for granting my research funding.

Last but not least, I would like to thank my parents for their unconditional love and sacrifices. Thanks for their encouragements to achieve advanced educations and careers which are far away from home and thanks for their taking good care of each other when I am not along.

CHAPTER 1

INTRODUCTION

This PhD study explores a multi-scale, multi-continuum and multi-physics model to simulate coupled fluid flow and geomechanics in shale gas reservoirs. It is about developing computational-mechanics solutions to problems related to shale gas reservoir developments. Two major research categories are involved in this study: shale gas reservoirs and computational mechanics. In this chapter, these two key words are first introduced, followed by the statement of problems and the thesis outline.

Shale gas refers to the natural gas trapped in shale formations. And shale, more properly called mudstones, is a clastic sedimentary rock composed of fine-grained particles of which the major minerals are quartz, calcite, and clay. Shale gas formations are unconventional reservoirs - i.e., reservoirs requiring special recovery operations outside the conventional operating practices. These special recovery operations for shale gas reservoirs are horizontal well drilling plus multi-stage hydraulic fracturing. The shale gas resource is globally abundant and present on every continent, which is widely believed to be an important part of the future energy mix because it is affordable, resource-abundant, energy-efficient, and environment-friendly.

Computational mechanics, along with theory and lab experiment, are three major approaches to understanding and solving mechanical problems in science and engineering. It is concerned with using computer capabilities to study events governed by the principles of mechanics. This method starts from physics-based governing equations, transforms these equations into a form which can be solved by the computer, and applies solutions to a science or engineering problem. It provides both qualitative and quantitative insights into many phenomena that are too complex to be studied through the theoretical analysis and some phenomena that are too dangerous or too expensive to be conducted by the experimental research.

The applications of computational mechanics to conventional reservoir developments have solved many practical engineering problems. Take the reservoir simulation for example, which is about numerical modeling of fluid flow in porous and fractured media. It has been developed as a relatively mature technology since the 1950s. It helps reservoir development and

management by forecasting fluid production, optimizing well design and completion, identifying the needs of artificial lift at present or in future, and evaluating options of improved or enhanced oil recovery approaches. The computational mechanics about solid deformation also achieved enormous success for the conventional reservoir development, which provides insights from wellbore stability to full field geomechanical earth models.

For some problems in unconventional reservoirs, however, there are some limitations on the direct applications of the developed computational technologies, and current understandings and technologies used in this area are behind industry needs. In this PhD study, we discuss three such problems and give our developed numerical solutions to them.

The first problem is about the effective and flexible handling of hydraulic fractures in fluid flow simulations. Hydraulic fractures are well-known to be crucial to hydrocarbon productions in unconventional reservoirs, because they provide a high conductivity pathway for fluid flow from the tight matrix to producing wells. These hydraulic fractures will most likely deviate from conventional bi-wing, ideal planar patterns and have a more complex geometry, due to formation heterogeneities, stress shadow effect, and interactions with natural fractures.

In Chapter 2, we present a three-dimensional embedded discrete fracture method (3D-EDFM), which is applicable to numerical simulation of fluid flow with complicated, arbitrary 3D hydraulic fracture networks. Key features of this 3D-EDFM methodology consist of vertex-based geometric calculations, and polygons with three to six vertices from box-plane intersections can be captured with this algorithm. The 3D-EDFM has been implemented in reservoir simulators via the integral finite difference (IFD) method. Its numerical scheme and implementation are verified by comparisons with analytical solutions and other established numerical solutions. This method not only provides an effective approach of handling realistic hydraulic fractures, but also significantly improves computational efficiency, while keeping sufficient accuracy. For some extreme cases that the transient state flow lasts long (i.e., large-size matrix blocks with extremely low permeability), our numerical analysis indicates only one level of local grid refinement (LGR) is needed to retain the required accuracy. We also provide an analytical-solution based method to optimize this LGR grid size if needed.

The second problem is about gas flow in shales with highly heterogeneous and hierarchical rock structures, which ranges from organic nanopores, inorganic nanopores, less permeable micro-fractures, more permeable macro-fractures to hydraulic fractures. The dominant fluid flow mechanism varies in these different geological constituents because they vary in shapes, characteristic lengths, flow conductivity, spacing/density and host materials. Although traditional single-porosity and double-porosity models can simulate certain time range of reservoir performance with acceptable accuracy, they are not applicable for the long-term predictions and have limitations to a more detailed understanding of such fluid flows.

In Chapter 3, we present a multi-domain, multi-physics model, aiming to realistically simulate the fluid flow in shale gas reservoirs considering its heterogeneous and hierarchical rock structures. A more physics-based conceptual model has been developed, which contains five flow regions: organic nanopores, inorganic nanopores, local micro-fractures, global natural fractures, and hydraulic fractures. Fluid flow governing equations varies according to their different dominant mechanisms.

The third problem is about the fluid-driven fracture propagation in porous media. This physical process includes three strong coupling mechanics: fluid flow in fractures and porous media, solid deformation with fractures, and fracture propagations. It is a fundamental process to many applications in petroleum engineering, such as hydraulic fracturing, produced water reinjection, borehole integrity, and drill cuttings reinjection. Quantitative evaluations of relevant fracture parameters are essential for the design analysis of these engineering. In the majority of available models, however, flow and solid deformation governing equations are oversimplified for the unconventional reservoirs.

In Chapter 4, a coupled simulation strategy combining the embedded discrete fracture method (EDFM) and the extended finite element method (X-FEM) is developed to simulate the fluid driven fracture propagation process in porous media. The EDFM and X-FEM are used to simulate fracture-related fluid mechanics and solid mechanics, respectively, with information exchanged under the iterative numerical coupling scheme. Mathematical equations on how to link these independent modules as well as numerical techniques on how to accelerate the coupling convergence rate are discussed in detail. Both X-FEM and EDFM avoid the

cumbersome construction of unstructured grids to capture fracture paths and also avoid the remeshing for the fracture growth. They are first validated via benchmark problems individually and then are coupled to simulate fracture propagation problems in two dimensions and in three dimensions. Simulated multi-physics fields meet our understandings qualitatively, and simulated fracture parameters (length, width and net pressure) match with analytical solutions quantitatively.

Note that this PhD thesis summaries the continuous work following my master thesis research conducted in Colorado School of Mines (Wang 2013). For the purpose of concise and focused presentations, repeatable work will not be included. Some fundamental knowledge about computational mechanics in fluid flow and solid deformation will not be included as well. One can refer to the book by Wu (2015) for fluid flow simulations and books by Bathe (2006) and by Smith et al. (2013) for solid deformation simulations.

CHAPTER 2

A GENERAL THREE-DIMENSIONAL EMBEDDED DISCRETE FRACTURE METHOD FOR RESERVOIR SIMULATION WITH COMPLICATED HYDRAULIC FRACTURES

In this chapter, we present a three-dimensional embedded discrete fracture method (3D-EDFM), which is applicable to numerical simulation of fluid flow in unconventional reservoirs with complicated, arbitrary 3D hydraulic fracture networks. Key features of this 3D-EDFM methodology consist of vertex-based geometric calculations, and polygons with three to six vertices from box-plane intersections can be captured with this algorithm. The 3D-EDFM has been implemented in reservoir simulators via the integral finite difference (IFD) method. Its numerical scheme and implementation are verified by comparisons with analytical solutions and other established numerical solutions. This method not only provides an effective approach of handling realistic hydraulic fractures, but also significantly improves computational efficiency, while keeping sufficient accuracy. For some extreme cases that the transient state flow lasts long (i.e., large-size matrix blocks with extremely low permeability), our numerical analysis indicates only one level of local grid refinement (LGR) is needed to retain the required accuracy. We also provide an analytical-solution based method to optimize this LGR grid size if needed.

Our approach is more general than previous models in the literature and noticeably broader in scope. This enhanced method is able to handle multiple 3D hydraulic fractures with arbitrary strikes and dip angles, shapes, curvatures, conductivities, and connections. Therefore, the 3D-EDFM provides great flexibility to handle hydraulic-fracture input data, interpreted from geomechanics modeling as well as microseismic data, for reservoir simulation. We present illustrative application examples for three unconventional reservoir engineering problems of interest in practice: (1) a single fracture with a complicated shape due to multi-layer geological features, (2) multiple isolated fractures with curvatures due to the stress shadow effect, and (3) multiple fractures with complicated orientations caused by natural fracture interactions. The 3D-EDFM is demonstrated to capture all the key flow patterns dominated by the discrete fractures in these three cases.

2.1 Introduction

Numerical simulation is a widely practiced and accepted technique in reservoir engineering to study flow and transport processes in subsurface systems. It helps reservoir development and management by forecasting fluid production, optimizing well design and completion, identifying the needs of artificial lift at present or in future, and evaluating options of improved or enhanced oil recovery approaches. For unconventional reservoirs, however, there are some limitations on applications of reservoir simulation technology, and current understandings and reservoir simulation technologies used in this area are far behind industry needs. One of the major limitations is effective and flexible handling of hydraulic fractures, which are well-known to be crucial to hydrocarbon production from unconventional reservoirs, because they provide a high conductivity pathway for fluid flow from the tight matrix to producing wells. These hydraulic fractures will most likely deviate from conventional bi-wing, ideal planar patterns and have a more complex geometry, due to formation heterogeneities, stress shadow effect, and interactions with natural fractures.

Several methods have been developed and applied to quantify flow and transport in the porous medium with fractures. The first methodology is to represent the rock as dual continua (Warren and Root 1963; Kazemi 1969; Duguid and Lee 1977; Pruess 1985; Wu and Pruess 1988). The dual-continuum approach is applicable to a naturally fractured reservoir with a denser fracture network or under the condition that fractures can be represented as a continuum. It includes one rock matrix continuum (high storage capacity and low conductivity) and another overlapping fracture continuum (negligible storage capacity and high conductivity). Interactions between these two continua are accounted by fluid flow assumed at quasi-steady state under pressure differences. The double-porosity model assumes global flow only occurs in the fracture continuum, and the matrix continuum supports fractures locally. The dual permeability model, which is a more general version, accounts both fracture and matrix global connections.

Only two parameters (one governing inter-porosity flow and the other relating to matrix storage capacity) are additionally introduced in this dual-continuum method for fractures. These two parameters are typically inferred from the build-up well test by assuming fractures uniformly distributed in the reservoir scale (Warren and Root 1963; Neuman 2005). Hence this approach will inevitably miss some local dominant, discrete features, e.g., hydraulic fractures in

unconventional reservoirs. The second approach (discrete fracture method, DFM for short), which can capture these local dominant features, is thus widely used to handle hydraulic fractures.

The DFM is to depict a reservoir system as a network of discrete fractures together with the permeable or impermeable matrix. This method directly makes use of fracture geometry data by considering fracture locations, orientations, shapes, apertures, and sizes. Numerically, fractures are explicitly modeled using specifically designed grid systems. The first gridding approach refines structured grids intersected by fractures at the scale of fracture widths. Fractures are then represented by a set of small-size and high-permeability grids (Slough et al. 1999; Sadrpanah et al. 2006). This local grid refinement (LGR) method can reduce numerical errors to an acceptable level. However, the substantial differences or highly contrasting respect ratios between adjacent grids regarding their dimensions can lead to numerical convergence problems. To overcome this problem, an approach of combining regular size grid and “pseudoized” fracture permeability is proposed, making the fracture conductivity (the multiplication between the fracture permeability k_f and the fracture aperture A_f) in the simulation identical to the real fracture conductivity (Rubin 2010; Ding et al. 2014).

The second DFM approach is based on unstructured grids. The space domain is gridded by treating fractures as internal boundaries. To conform the fracture geometries, triangle or PEI grids are used for 2D simulations (Karimi et al. 2004; Sun and Schechter 2014), and 3D tetrahedral grids (Hui et al. 2007) are used for 3D simulations. Compared with the LGR method, this approach is more flexible to handle fractures with arbitrary directions. However, constructing such meshes is quite challenging, especially, in three-dimensional problems considering multiple connected fractures, because the mesh has to be built in a way that the grid edges/faces coincide with all fracture surfaces.

The EDFM is another numerical technique of the generalized discrete fracture method. This method is first introduced by Lee et. al (Lee et al. 2001) to simulate long fractures and further extended by Li and Lee (Li and Lee 2008) and Moinfar (Moinfar et al. 2014a). As its name implies, fractures are virtually embedded into the nearby matrix grid blocks. The fracture thickness is only considered in the computation domain for fracture volume calculations, but not

represented in the grid domain, because fracture thickness is several orders of magnitude smaller than a typical simulation grid size.

As an analogy, the idea of the EDFM is basically identical to the well handling method in traditional reservoir simulation (Peaceman 1978). The pressure inside a fracture, p_f , the discrete pressure in the grid block containing this fracture, p_i , and the volumetric flow rate, q_i are related by a fracture-index FI_i :

$$q_i = FI_i \frac{kk_r}{\mu} (p_i - p_f) \quad (2.1)$$

where k is the average (such as harmonic-weighted) absolute permeability at the interface; k_r is the relative permeability through the upstream weighting scheme; μ is the fluid phase dynamic viscosity; and the fracture-index FI_i is defined as:

$$FI_i = \frac{A_i}{d_m + d_f} \quad (2.2)$$

where A_i is the common interface area between the intersected block and the fracture; d_m and d_f are distances from inside the matrix grid block and the fracture to this interface according to EDFM assumptions.

This way, the mesh does not need to be specially processed to track the fracture path, which greatly reduces the number of grid cells and generate a Jacobian matrix with a similar sparsity pattern as the traditional reservoir simulation. Such features can significantly improve simulation efficiency, at least for the default solver in our simulator (DSLUCS, a Lanczos-type bi-conjugate gradient solver). Because localized features are not efficiently resolved by its mesh refinement, this method cannot avoid introducing numerical discretization errors in the local approximation space domain. To resolve the problem, accuracy evaluation is one of focus points in this study.

This paper summarizes our recent study of enhancing the EDFM to model fluid flow in unconventional reservoirs with arbitrary 3D hydraulic fractures. In particular, we develop a

vertex-based geometric algorithm to evaluate key parameters in the EDFM - the fracture index. Our approach is more general than the previous models in the literature and noticeably broader in scope for application. It is able to handle multiple 3D hydraulic fractures with arbitrary strike and dip angles, shapes, conductivities, and connections. Its numerical implementation is verified by comparison with both analytical solutions and other established numerical solutions. In addition, our analytical and simulation results conclude the EDFM can provide results with acceptable accuracy for practical engineering applications. For some extreme cases that the transient state flow lasts long (large-size matrix grids with extremely low permeability), only one level of local grid refinement is needed to guarantee accuracy. We provide an analytical solution based approach to optimize this grid size, if local grid refining is needed. To illustrate this new approach, we present several application examples of interest to unconventional reservoir simulation. We demonstrate that the 3D EDFM is capable of handling common problems in unconventional reservoirs with complicated fractures, caused by multi-scale heterogeneity, stress shadow effect, and interactions between hydraulic and natural fractures.

2.2 Governing Equations

In our previous work, we introduced a generalized framework model to simulate fluid flows in unconventional reservoirs (Wu 1998; Wang 2013; Wu et al. 2014; Wang and Wu 2015; Cai et al. 2015). The integral finite difference method (equivalent to the Finite Volume method) is chosen to discretize governing PDEs in the space domain (Narasimhan and Witherspoon 1976; Pruess et al. 1999). Two types of equations in this method will be briefly discussed in this section, because both are involved with geometric quantities. The first group is the discrete equation for mass conservation of multiphase, multi-component fluid flow at grid block or node i , which can be written in a general form.

$$\left\{ \left(\phi S_{\beta} \rho_{\beta} \right)_i^{k,n+1} - \left(S_{\beta} \rho_{\beta} \right)_i^{k,n} \right\} \frac{V_i}{\Delta t} = \sum_{j \in \eta_i} \text{flow}_{ij}^{k,n+1} + Q_i^{k,n+1} \quad (2.3)$$

$$(k = 1, 2, 3) \text{ and } (i = 1, 2, 3, \dots, N)$$

where ϕ is the effective porosity of porous or fractured media; S_{β} and ρ_{β} are the saturation and density of fluid β ; superscript k serves as an equation index for various phases with $k = 1$ (gas), 2 (water), and 3 (oil); superscript n and $n+1$ denote the previous time level and the current time

level; subscript i is the index of grid block i ; N is the total number of nodes or grid blocks; Δt is time step size; V_i is the node i volume; η_i contains neighboring nodes (j) of node i ; the component mass “flow” term between node i and j are further explained in Eq. (2.4); Q is the sink/source term at node i for phase k .

The second set of equation is the expanded form of the flow term in the right-hand side of Eq. (2.3). It represents the mass flux by multiphase flow or advective processes mainly, which are described by a discrete version of Darcy’s law or various non-Darcy flow models (Wu 2002). When Darcy’s law applies, the mass flux of fluid phase β along the connection in discrete mass conservation Eq. (2.3) is given by

$$\text{flow}_{\beta,ij} = \left(\frac{\rho_\beta k_{r\beta}}{\mu_\beta} \right)_{ij+1/2} \frac{A_{ij} k_{ij+1/2}}{d_i + d_j} (\Phi_{\beta j} - \Phi_{\beta i}) \quad (2.4)$$

where $k_{r\beta}$ and μ_β are the relative permeability and viscosity of fluid β ; A_{ij} is the node i and j common interface area; d_i is the distance between the center of block i and the common interface A_{ij} . $k_{ij+1/2}$ is an averaged (such as harmonic-weighted) absolute permeability. $\Phi_{\beta j}$ is the flow potential of fluid β in node j .

Three geometric quantities involved in these two sets of equations are the element volume V_i , the connection area A_{ij} , and the connection distances d_i , d_j . One attractive feature of the IFD method is that these geometric quantities are input directly instead of having them generated during the simulation. Therefore, great flexibility is achieved so that a computational volume element in any one continuum (fracture or matrix) can connect with another element in its own or other continuum. In other words, no specific programming changes are required in the simulator to distinguish fracture-fracture, matrix-matrix, and fracture-matrix connections. All these different types of connections are handled numerically in the same way once their geometric properties are prepared and defined in the input file.

From this point of view, the IFD (or FV) is general for implementing various conceptual models of fractured reservoirs, which includes the classical dual-porosity and dual-permeability model, multiple interacting continua (MINC) model, discrete fracture model (DFM), and

embedded discrete fracture model (EDFM). Therefore, the hybrid fracture model, which combines DFM, MINC, and a homogeneous porous medium, can be handled straightforwardly (Karsten Pruess 1985). The key is obtaining geometric features or properties (volume, distance, and interface area) based on the model approximations and assumptions.

2.3 Geometric Property Calculation

The method of the 3D-EDFM is conceptually similar to 2D cases (Lee, Lough, and Jensen 2001; Li and Lee 2008; X. Yan et al. 2016), of which the key is the appropriate preprocessing of geometrical information. But its practical implementation is more complicated. As shown in Figure 2-1, one full intersection between a box and a 3D plane could lead to a polygon with 3 to 6 vertices, not to mention if the plane partly penetrates the box, which makes the geometric calculation more complicated. In this section, some key geometry issues are described, aiming towards an accurate and robust implementation for multiple fractures with arbitrary shapes, directions, conductivities and connections.

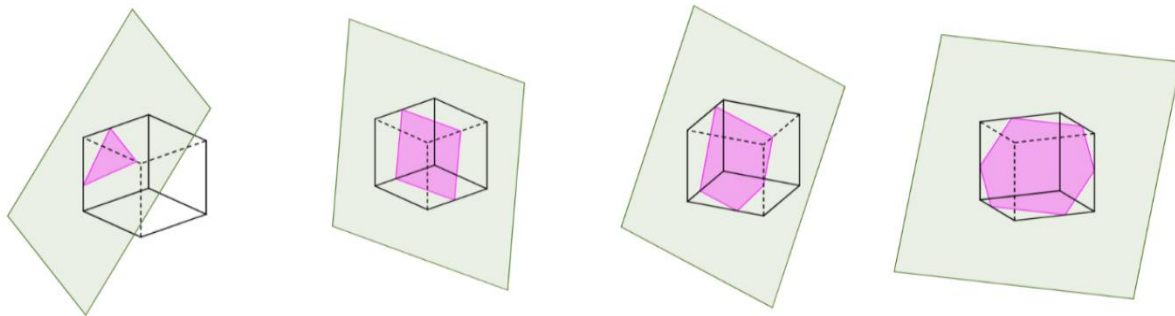


Figure 2-1 Schematic of the full intersection between a box and a fracture plane, leading to a polygon with 3 to 6 vertices

2.3.1 Connection Area

Our approach of computing the area of intersection polygons is based directly on vertices, which includes three major steps: 1) finding all vertices of the intersected polygon; 2) sorting all these vertices in the clockwise or counter-clockwise order; and 3) calculating the intersected polygon area based on the well-sorted vertices; Figure 2-2 shows the relevant flow chart, and the following sections introduce these major steps in detail.

To obtain all intersections in a fractured reservoir, we need to calculate the intersection between each fracture and each grid cell first, which starts from finding all vertices of the intersected polygon by checking:

1. if one or more of the fracture polygon points are inside the box;
2. if any of the box edges are intersected with the fracture polygon face; and
3. if any of the fracture polygon's edges are intersected with the box faces.

Calculating the intersection between the box edge and the polygon face or the intersection between the box face and polygon edge is easy. The general equation of a 3D plane is

$$ax + by + cz + D = 0 \quad (2.5)$$

Its Hessian normal form is

$$\hat{\mathbf{n}} \cdot \mathbf{x} = E \quad (2.6)$$

where $\hat{\mathbf{n}}$ is the unit normal vector, with components of $\hat{\mathbf{n}} = (n_x, n_y, n_z)$

$$n_x = \frac{a}{\sqrt{a^2 + b^2 + c^2}}, \quad n_y = \frac{b}{\sqrt{a^2 + b^2 + c^2}}, \quad n_z = \frac{c}{\sqrt{a^2 + b^2 + c^2}} \quad (2.7)$$

E is a constant

$$E = -\frac{D}{\sqrt{a^2 + b^2 + c^2}} \quad (2.8)$$

The line segment related to endpoints V_i and V_j can be expressed as:

$$\begin{aligned} E_{ij} &= V_i + \lambda(V_j - V_i) \\ &= V_i + \lambda e_{ij} \quad \text{with } \lambda \in [0, 1] \end{aligned} \quad (2.9)$$

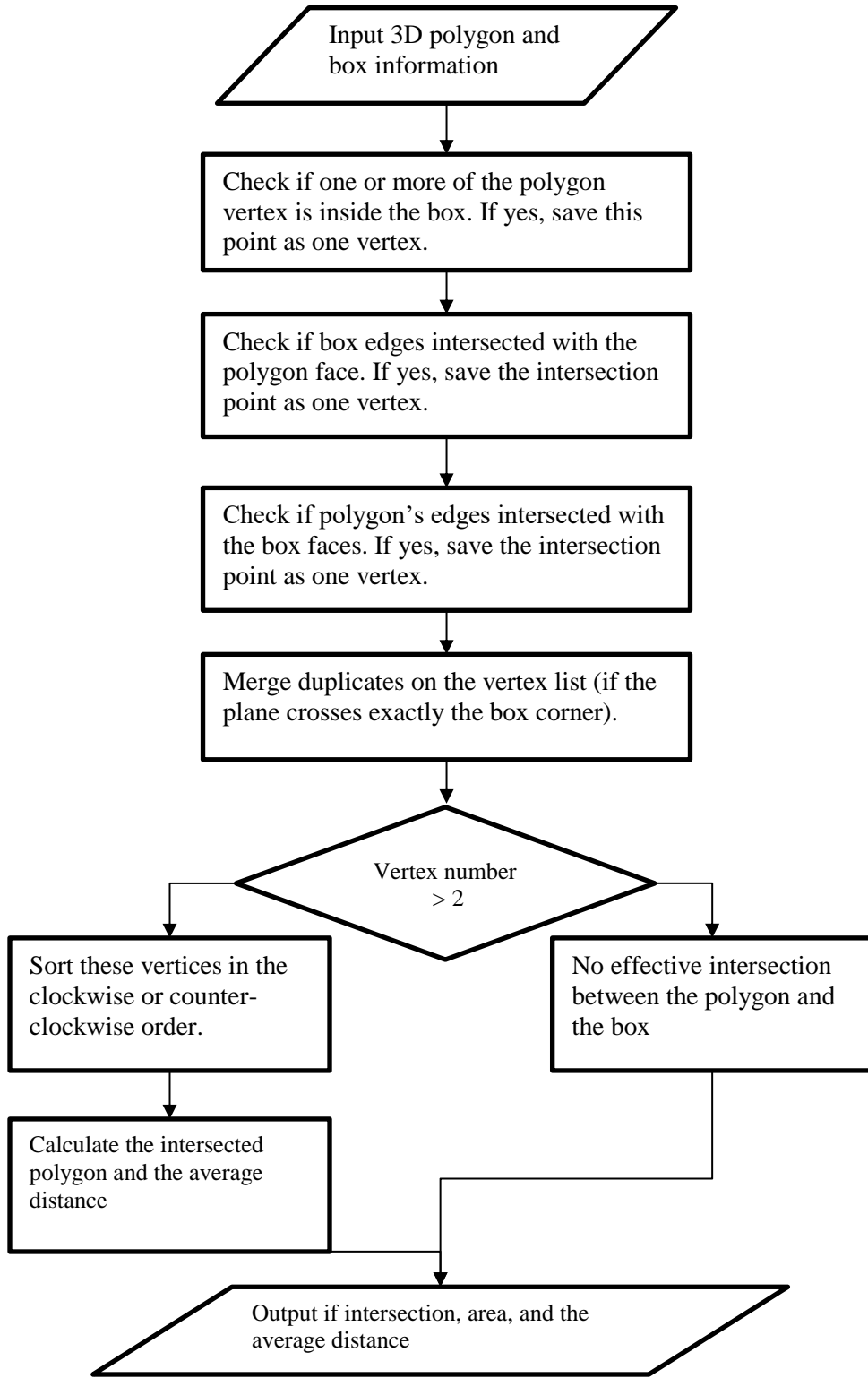


Figure 2-2 Flowchart to calculate 3D box and plane intersections

If the intersection between the plane and the straight line exists,

$$\hat{\mathbf{n}} \cdot (\mathbf{V}_i + \lambda \mathbf{e}_{ij}) = E \quad (2.10)$$

$$\lambda = \frac{E - \hat{\mathbf{n}} \cdot \mathbf{V}_i}{\hat{\mathbf{n}} \cdot \mathbf{e}_{ij}} \quad (2.11)$$

The intersection point \mathbf{P} is:

$$\mathbf{P} = \mathbf{V}_i + \lambda \mathbf{e}_{ij} \quad (2.12)$$

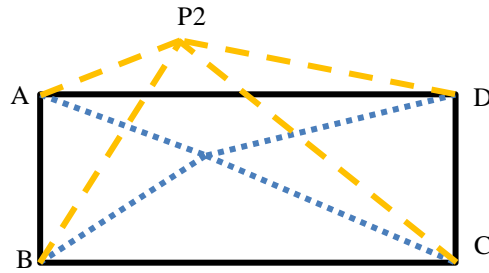


Figure 2-3 Point is inside the rectangle if and only if the sum of areas of four triangles equals to the rectangle area

This intersection is valid only if the intersection point is inside both the line segment and the polygon. The first condition is met when λ is in the range $[0,1]$. For the second condition, let the intersection point be $\mathbf{P}(x, y, z)$, and the rectangle is defined by four corner points $A(x_1, y_1, z_1)$, $B(x_2, y_2, z_2)$, $C(x_3, y_3, z_3)$, and $D(x_4, y_4, z_4)$. We first calculate the sum of areas of ΔAPB , ΔBPC , ΔCPD , and ΔDPA . If this sum is greater than the area of the rectangle, then $\mathbf{P}(x, y)$ is outside the rectangle. Else if the sum is equal to the area of the rectangle (it cannot be less than the latter), $\mathbf{P}(x, y)$ is on the rectangle or inside the rectangle (Figure 2-3). Notice that since data is stored using finite-precision arithmetic, the algorithm robustness needs to be maintained for small perturbations in the data.

In this process, Heron's formula is used to calculate the area of the 3D triangle, as it requires no arbitrary choice of the side as base or vertex as the origin. Take ΔAPB for example,

$$A_{\Delta APB} = \sqrt{s(s - l_{AP})(s - l_{PB})(s - l_{BA})} \quad (2.13)$$

where s is half of the perimeter $p_{\Delta APB} = l_{AP} + l_{PB} + l_{BA}$.

Sorting vertices in a clockwise or counter-clockwise order is essential for the calculation of the polygon area. In this study, the sorting is based on the direction angles of vectors between the polygon central point and these vertices. We use the central point $C(x_c, y_c, z_c)$ here because it's always inside the polygon, with components:

$$x_c = \frac{1}{n} \sum_{i=1}^n x_i; \quad y_c = \frac{1}{n} \sum_{i=1}^n y_i; \quad z_c = \frac{1}{n} \sum_{i=1}^n z_i \quad (2.14)$$

where n is the number of polygon vertexes; x_i , y_i , and z_i are coordinates of the i th vertex.

The atan2 function (Heckbert 1994), used in this study, considers the signs of both vectoral components and returns the four-quadrant inverse tangent value in the closed interval $[-\pi, \pi]$. In contrast, the normal inverse tangent function atan only returns values within the interval $[-\pi/2, \pi/2]$, which cannot tell the quadrant information. The direction based sorting method only applies for polygons in 2D space. For our problem, the polygon in 3D space needs to be first projected to a two-dimensional plane. If the projected polygon is not a line segment after the projection, the projected vertices remain their original order. In this study, if this polygon is not perpendicular to the x - y plane ($n_z \neq 0$), it is projected to the x - y plane; else if the polygon is not perpendicular to the y - z plane ($n_x \neq 0$), it is projected to the y - z plane; else it is projected to the x - z plane.

Once the vertex coordinate array and the vertex order are prepared, the area of the intersected polygon can be calculated by summing up a series of triangle areas.

$$A_{\text{polygon}} = \sum_{i=1}^n \Delta CE_i \quad (2.15)$$

where n is the number of polygon edges; C is the central point of the polygon as in Eq. (2.14); E is the i th edge of the polygon.

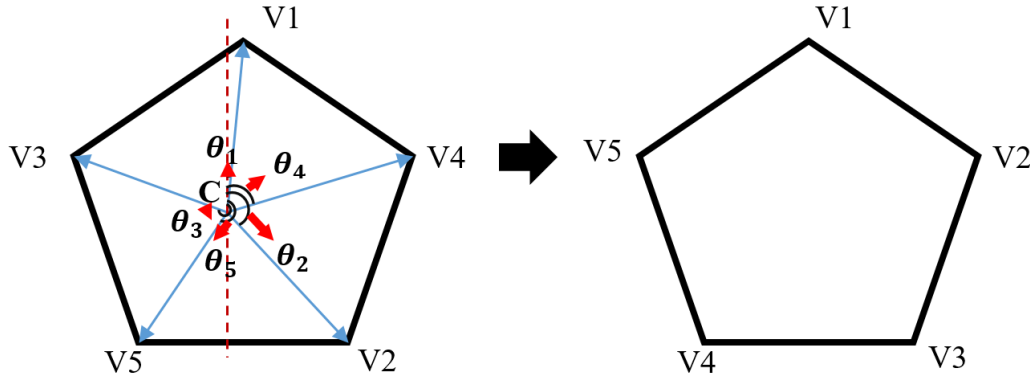


Figure 2-4 Sort vertices in a clockwise order based on the direction angle between them and the central point

2.3.2 Connection Distances

In this numerical method, the distance from the center of a fracture element to the fracture-matrix interface is set to zero, because the fracture width or aperture is negligible compared with a typical matrix block size, and the pressure within the fracture grid reaches equilibrium in the perpendicular direction to the fracture plane almost instantaneously. The distance from the computational center of the matrix element to the common interface is estimated by the numerical integration over the grid volume. This approximates the definite integral of a function, usually stated as a weighted sum of function values within the domain of integration at specified points (Davis and Rabinowitz 2007). Eq.(2.16) shows the numerical integration method to obtain the average distance.

$$d_{ave} = \sum_i \sum_j \sum_k \alpha_i \alpha_j \alpha_k d(i, j, k) \quad (2.16)$$

where i, j and k denote the integration points; α is the weight coefficient. d is the point-plane distance in 3D space

$$d = \frac{|ax_{(i,j,k)} + by_{(i,j,k)} + cz_{(i,j,k)} + d|}{\sqrt{a^2 + b^2 + c^2}} \quad (2.17)$$

It can be proven that this geometrical average distance equals to the fluid-flow average distance if flow inside the intersected grid block is in the steady and pseudo-steady state (Section

2.4.2). However, if fluid flow is in the transient state (e.g. only part of the grid volume is drained), the geometrical average distance cannot represent the fluid-flow average distance anymore. This situation usually happens at the beginning of productions or injections. A substantial amount of simulation errors can be expected if this transient-state situation lasts long, which possibly occurs for cases with large-size matrix blocks with extremely low matrix permeability. To quantify this effect and to optimize grid-block sizes for the EDFM, analytical solutions of a 1D fluid flow problem with single fracture (Figure 2-5) are derived.

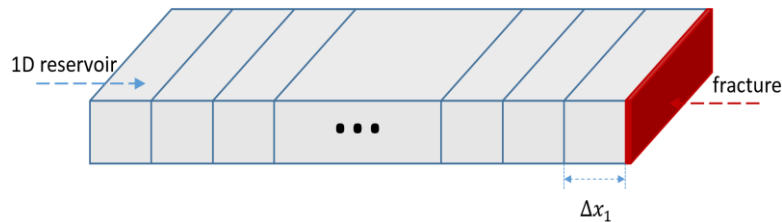


Figure 2-5 Demonstration of a 1D reservoir under production via a fracture with constant pressures

In the 1D problem, constant fracture pressure is applied on the right (Dirichlet condition), and closed boundary condition is applied on the left (Neumann condition). Eq. (2.18) gives its analytical solution. Details about the derivation are included in Section 2.4.1.

$$p(x, t) = p_f + \frac{2(p_i - p_f)}{\pi} \sum_{n=1}^{\infty} \frac{1}{\left(n - \frac{1}{2}\right)} \sin \left[\left(n - \frac{1}{2}\right) \pi \frac{x}{x_L} \right] \exp \left(-\left(n - 0.5\right)^2 \pi^2 \frac{k}{\phi \mu c x_L^2} t \right) \quad (2.18)$$

The geometrical average distance (d_{m-g}) for the fracture-intersected grid block (the first grid block in this problem) is half of the grid size. The fluid-flow average distance (d_{m-f}) is derived based on the analytical solution.

$$d_{m-g} = \frac{\Delta x_1}{2} \quad (2.19)$$

$$d_{m-f} = \frac{x_L^2 \sum_{n=1}^{\infty} \frac{1}{(n-0.5)^2} \left(1 - \cos \left[(n-0.5) \pi \frac{\Delta x_1}{x_L} \right] \right) \exp \left(-(n-0.5)^2 \pi^2 \frac{k}{\phi \mu c x_L^2} t \right)}{\Delta x_1 \pi^2 \sum_{n=1}^{\infty} \exp \left(-(n-0.5)^2 \pi^2 \frac{k}{\phi \mu c x_L^2} t \right)} \quad (2.20)$$

where the average distance d_{m-f} is a function of grid block size Δx_1 , reservoir/matrix permeability k , reservoir/matrix porosity ϕ , fluid viscosity μ , total compressibility c , time t , and reservoir size x_L . Further analysis indicates that d_{m-f} is most sensitive to reservoir/matrix permeability, grid block size, and time among all these parameters within physically reasonable ranges. We plot the ratio of these two average distances as a function of time with two different permeability (1.0 mD and 0.01 mD) and three different matrix grid-block sizes (1m, 5m, and 10m), as shown in Figure 2-6. For the matrix permeability of 1.0md, the geometrically calculated average distance with these three grid-block sizes is close to the analytically derived distance in early-, mid-, and late-stages. This means the numerical solution from the EDFM method will be in good agreement with the analytical (true) solution. For the permeability of 0.01 mD, however, cases with 5m and 10m blocks have a considerable discrepancy before 1.0 day. Numerical solutions with the EDFM method will have substantial errors in the early time correspondingly. The case with the 1m grid keeps close almost all the time.

Quantitative studies above indicate that the EDFM does not guarantee to provide accurate solutions under all conditions, which can be verified by simulation results in the later section. A quick evaluation of the grid size based on the analytical solution is thus suggested to perform before numerical simulations. For a specific reservoir simulation case, this grid size can be quantitatively determined given the simulation time step and the error tolerance of the distance ratio discussed above. Since the EDFM only introduces errors near the fracture in the space domain, i.e., grid blocks that are intersected by the fracture, we only need to refine these grids if the original grid-block size is too large, instead of applying the refined grid in the global reservoir domain.

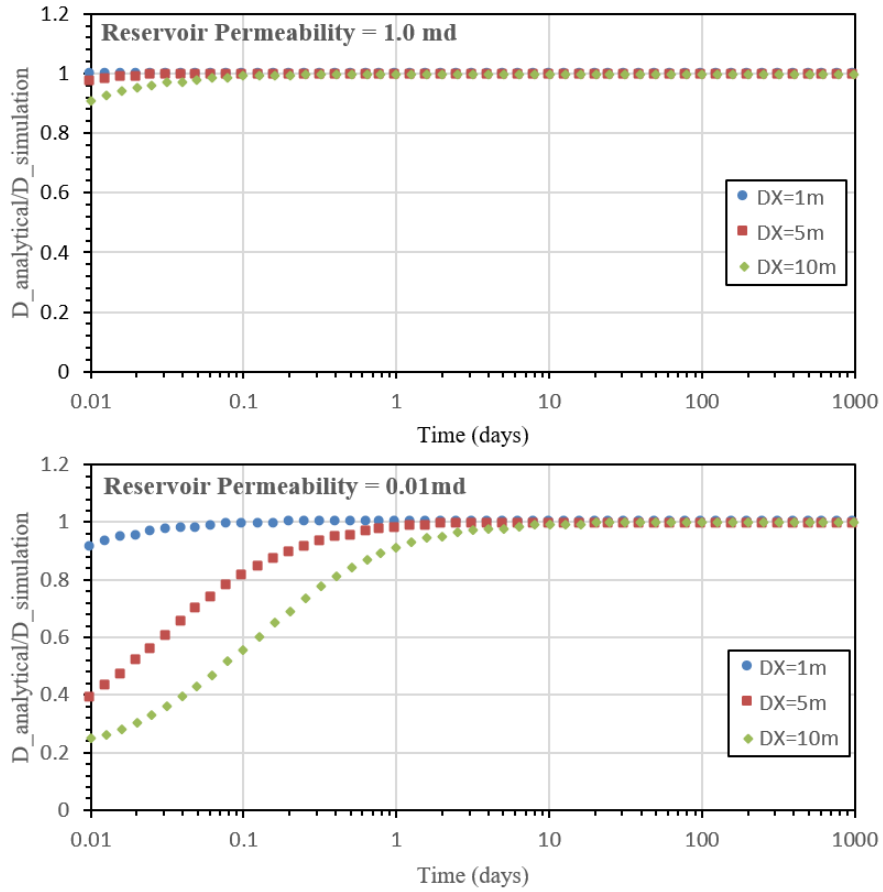


Figure 2-6 Ratio of two average distances with time for two different matrix permeability (1.0 mD and 0.01 mD) and three different matrix-block sizes (1m, 5m, and 10m)

2.3.3 Infinite and Finite Conductivity Fracture

Infinite conductivity fractures refer to fractures with zero pressure drop along the fracture during production or infinite large fracture permeability, while finite conductivity fractures are those with nonzero pressure drop along the fracture. The assumption of infinite fracture conductivity is valid if the dimensionless fracture conductivity $F_{cd} = (k_f w_f) / (k_m x_f)$ is larger than 300 (Cinco-Ley and Samaniego 1981). These two kinds of fractures are handled differently in this study. For the infinite-conductivity case, the fracture is represented by only one computational volume element, of which the volume is the total volume of the fracture (left one in Figure 2-7). This computational volume element connects to many matrix grid blocks. Calculations of the area and distances for each connection are discussed above. In this way, the pressure inside the fracture is the same.

For the finite-conductivity case, the fracture is further gridded into a set of fracture elements, as shown in the right plot of Figure 2-7. In addition to matrix-matrix connections and matrix-fracture connections, we have fracture-fracture connections as well. Fracture-fracture connections can be calculated geometrically by checking their shared edges. The effective intersection between the fracture and one grid block leads to one fracture element. Thus, each fracture element only connects to one matrix grid block or two (if the fracture plane is on the face of the grid box).

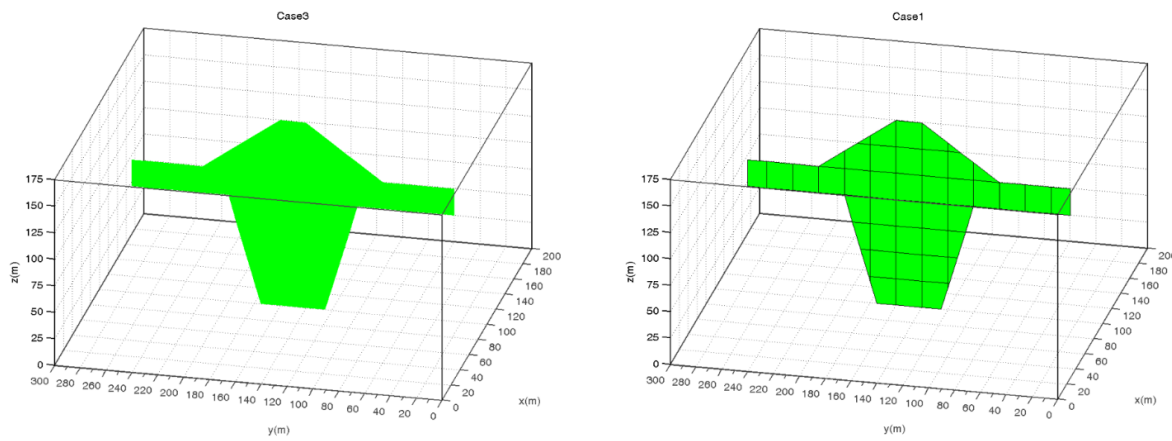


Figure 2-7 Demonstrations of different numerical methods to handle infinite-conductivity fracture (left) and finite-conductivity fracture (right)

2.3.4 Multiple Connected Fractures

Discussion above is about the processing of a single discrete fracture. For cases with multiple discrete fractures, if these fractures do not intersect, they are embedded in matrix grids separately as the single fracture. Otherwise, if there are intersections, special treatments need to be made for grids containing intersections (grids intersected with more than one fractures). Our solutions for this part are explained using a 2D synthetic problem for simple illustration, as shown in the upper left part of Figure 2-8. It includes two matrix blocks and three fractures. In this approach, multiple fracture segments intersected with the same grid are aggregated into one computational volume element. Thus, this problem is transferred into fluid flow among four computational volume elements (two matrix elements and two fracture elements). It includes one matrix-matrix, one fracture-fracture, and two matrix-fracture connections, as shown in the right part of Figure 2-8. This transformation follows the same idea as the classical double-permeability

model (Duguid and Lee 1977). It will not introduce significant numerical discretization errors, because pressure drops among various jointed fracture segments inside one grid block (especially in a locally refined grid) are negligible given their short connecting distance and high conductivities.

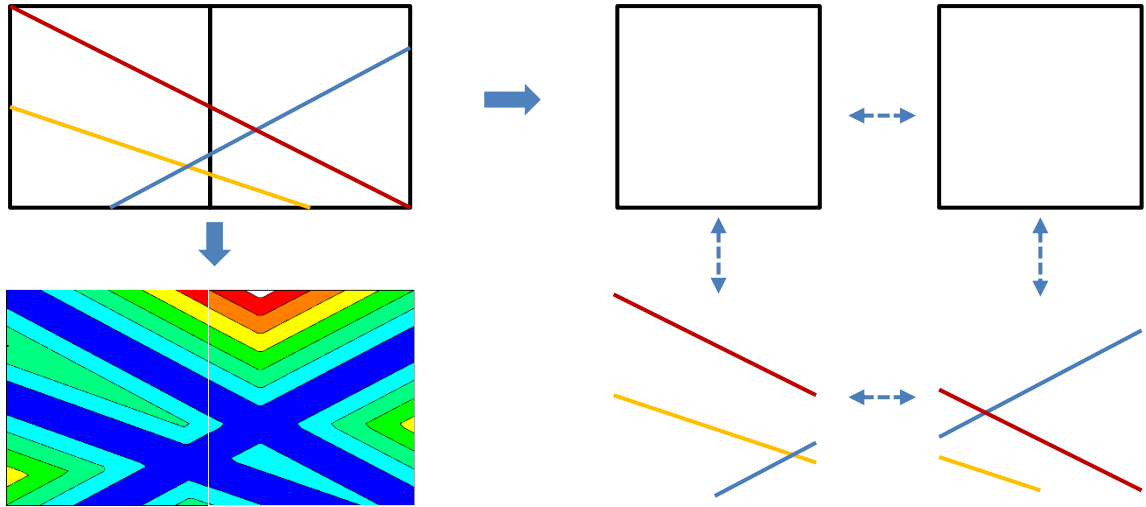


Figure 2-8 upper left: a 2D synthetic problem with two matrix blocks and three intersected fractures. Right: Numerical idealization for this problem, which includes two matrix elements and two fracture elements; Lower left: distance contour for matrix-fracture connections

Compared with other alternative treatment methods (Moinfar et al. 2014a), this local fracture-segment aggregation method reduces efforts of geometric calculations. The matrix-matrix and fracture-fracture connections can be obtained straightforwardly. For the matrix-fracture connections, the connection area is the sum of all intersected polygon area. The distance is calculated using the numerical integration following Eq. (2.16). Unlike the distance for the single-fracture intersection, $d(i, j, k)$ is the distance from the point (i, j, k) to the nearest fracture.

$$d(i, j, k) = \min_{t=1:m} [\text{distance}(P_{i,j,k}, \text{Fracture}_t)] \quad (2.21)$$

where m is the number of fractures intersected with this matrix grid. The lower left plot in Figure 2-8 shows the contour of this distance for two matrix-fracture connections in this problem.

2.4 Analytical Solutions for 1D Fluid Flow with a Fracture

Three analytical solutions are derived to support the matrix-fracture average distance used in our EDFM approach. All solve the governing equation of 1D fluid flow of a single-phase single-component slightly compressible fluid in a homogeneous porous medium with a fracture. For the first one, Dirichlet conditions on the left and Neumann conditions on the right are imposed. The derived analytical solution is able to capture all transient state, pseudo-steady state and steady state fluid flow. For the second and third ones, analytical solutions for fluid flow in pseudo-steady state and steady state are derived, respectively.

2.4.1 General Analytical Solutions for 1D Fluid Flow with a Fracture

The governing equation of 1D fluid flow of a single-phase single-component slightly compressible fluid in a homogeneous porous medium can be expressed as:

$$\frac{\partial p}{\partial t} = \frac{k}{\phi \mu c} \frac{\partial^2 p}{\partial x^2} \quad (2.22)$$

The corresponding initial conditions and boundary conditions (Dirichlet conditions on the left and Neumann conditions on the right) are:

$$p(x, 0) = p_i \quad (2.23)$$

$$p(0, t) = p_f, \quad p_f < p_i \quad (2.24)$$

$$\frac{\partial p}{\partial x}(x_L, t) = 0 \quad (2.25)$$

Introduce dimensionless variables

$$x_D = \frac{1}{x_L} x \quad (2.26)$$

$$t_D = \frac{k}{\phi \mu c x_L^2} t \quad (2.27)$$

$$p_D = \frac{(p - p_f)}{p_i} \quad (2.28)$$

From the chain rule,

$$\frac{\partial p}{\partial t} = \frac{\partial p}{\partial p_D} \frac{\partial p_D}{\partial t_D} \frac{\partial t_D}{\partial t} = p_i \frac{k}{\phi \mu c x_L^2} \frac{\partial p_D}{\partial t_D} \quad (2.29)$$

$$\frac{\partial^2 p}{\partial x^2} = \left(\frac{\partial x_D}{\partial x} \right)^2 \frac{\partial p}{\partial p_D} \frac{\partial^2 p_D}{\partial x_D^2} = \frac{1}{x_L^2} p_i \frac{\partial^2 p_D}{\partial x_D^2} \quad (2.30)$$

$$\frac{\partial p}{\partial x} = \frac{\partial p}{\partial p_D} \frac{\partial p_D}{\partial x_D} \frac{\partial x_D}{\partial x} = p_i \frac{1}{x_L} \frac{\partial p_D}{\partial x_D} \quad (2.31)$$

Substitute Eqs. (2.29) - (2.31) to Eqs. (2.22) - (2.25), we have the dimensionless form of 1D fluid flow in porous medium governing equations as well as its boundary and initial conditions:

$$\frac{\partial p_D}{\partial t_D} = \frac{\partial^2 p_D}{\partial x_D^2} \quad (2.32)$$

$$p_D(x_D, 0) = \frac{(p_i - p_f)}{p_i} \quad (2.33)$$

$$p_D(0, t_D) = 0 \quad (2.34)$$

$$\frac{\partial p_D}{\partial x_D}(1, t_D) = 0 \quad (2.35)$$

We look for a solution to the dimensionless diffusion Eqs. (2.32) - (2.35) in the from:

$$p_D(x_D, t_D) = X(x_D)T(t_D) \quad (2.36)$$

where the two-variable function p_D is expressed as the product of two single-variable functions. The partial differential equation Eq. (2.36) becomes

$$\frac{T'(t_D)}{T(t_D)} = \frac{X''(x_D)}{X(x_D)} \quad (2.37)$$

The left-hand side of Eq. (2.37) depends only on t_D and the right-hand side only depends on x_D . If this equation holds with various t_D and x_D , both the left- and right-hand side must be constant, which we set to $-\lambda$ by convention:

$$\frac{T'(t_D)}{T(t_D)} = \frac{X''(x_D)}{X(x_D)} = -\lambda, \quad \lambda = \text{constant} \quad (2.38)$$

The boundary conditions become,

$$X(0)T(t_D) = 0 \quad (2.39)$$

$$X'(l)T(t_D) = 0 \quad (2.40)$$

Taking $T(t_D) = 0$ would give $P_D = 0$ for all time and space (trivial solution) from Eq. (2.36), which does not apply physically for this problem. Hence Eq. (2.39) and Eq. (2.40) are only satisfied if

$$X(0) = X'(l) = 0 \quad (2.41)$$

Eq. (2.38) gives two separate differential equations in terms of time and space, respectively.

$$T'(t_D) = -\lambda T(t_D) \quad (2.42)$$

$$X''(x_D) = -\lambda X(x_D) \quad (2.43)$$

The general solution of Eq. (2.42) is

$$T(t_D) = e^{-\lambda t_D} \quad (2.44)$$

Eq. (2.43) is an example of a Sturm-Liouville problem. Cases with $\lambda < 0$ and $\lambda = 0$ lead to trivial solutions for this problem, which need to be discarded. For $\lambda > 0$, Eq. (2.43) is the simple harmonic equation of which the general solution is:

$$X(x_D) = A \sin(\sqrt{\lambda} x_D) + B \cos(\sqrt{\lambda} x_D) \quad (2.45)$$

The boundary conditions Eq.(2.41) implies

$$B = 0 \quad (2.46)$$

$$A\sqrt{\lambda} \cos\sqrt{\lambda} = 0 \quad (2.47)$$

To obtain a non-trivial solution,

$$\sqrt{\lambda} = \left(n - \frac{1}{2}\right)\pi \quad (2.48)$$

where n denotes any nonzero integer ($n = 1, 2, 3, \dots$). Thus, the eigenvalues of this Sturm-Liouville problem are

$$\lambda_n = \left(n - \frac{1}{2}\right)^2 \pi^2, \quad n=1,2,3,\dots \quad (2.49)$$

And the corresponding eigenfunctions of the Sturm-Liouville problem are

$$X_n(x_D) = A_n \sin\left[\left(n - \frac{1}{2}\right)\pi x_D\right], \quad n=1,2,3,\dots \quad (2.50)$$

Based on the superposition principle, the general solution of the dimensionless pressure is:

$$p_D(x_D, t_D) = \sum_{n=1}^{\infty} A_n \sin\left[\left(n - \frac{1}{2}\right)\pi x_D\right] \exp\left(-\left(n - 0.5\right)^2 \pi^2 t_D\right) \quad (2.51)$$

Now we apply the initial conditions in Eq. (2.33),

$$\frac{(p_i - p_f)}{p_i} = \sum_{n=1}^{\infty} A_n \sin \left[\left(n - \frac{1}{2} \right) \pi x_D \right] \quad (2.52)$$

The right-hand side is the Fourier Sine Series, and these eigenfunctions have the orthogonality property. These functions form orthogonal functions basis. The parameter A_n is

the projection of $\frac{(p_i - p_f)}{p_i}$ on the function basis $\sin \left[\left(n - \frac{1}{2} \right) \pi x_D \right]$:

$$A_n = \frac{\int_0^1 \frac{(p_i - p_f)}{p_i} \sin \left[\left(n - \frac{1}{2} \right) \pi x_D \right] dx_D}{\int_0^1 \sin^2 \left[\left(n - \frac{1}{2} \right) \pi x_D \right] dx_D} = \frac{2(p_i - p_f)}{p_i \left(n - \frac{1}{2} \right) \pi} \quad (2.53)$$

Once all parameters A_n are obtained, we have the dimensionless analytical solution for this 1D fluid flow problem as

$$p_D(x_D, t_D) = \frac{2(p_i - p_f)}{p_i \pi} \sum_{n=1}^{\infty} \frac{1}{\left(n - \frac{1}{2} \right)} \sin \left[\left(n - \frac{1}{2} \right) \pi x_D \right] \exp(- (n - 0.5)^2 \pi^2 t_D) \quad (2.54)$$

Correspondingly, the analytical solution of pressure as a function of time and space is

$$p(x, t) = p_f + \frac{2(p_i - p_f)}{\pi} \sum_{n=1}^{\infty} \frac{1}{\left(n - \frac{1}{2} \right)} \sin \left[\left(n - \frac{1}{2} \right) \pi \frac{x}{x_L} \right] \exp(- (n - 0.5)^2 \pi^2 \frac{k}{\phi \mu c x_L^2} t) \quad (2.55)$$

Production rate into the fracture can be derived based on Darcy's Law and Eq. (2.55):

$$q = A_f \frac{k}{\mu} \frac{\partial p}{\partial x}(0, t) = A_f \frac{k}{\mu} \frac{2(p_i - p_f)}{x_L} \sum_{n=1}^{\infty} \exp(- (n - 0.5)^2 \pi^2 \frac{k}{\phi \mu c x_L^2} t) \quad (2.56)$$

The average pressure in the first grid (with the width of Δx_1) is obtained by the integration over this grid volume:

$$\begin{aligned}
p_{ave}(0:\Delta x_1, t) &= \frac{\int_0^{\Delta x_1} p(x, t) A_f dx}{A_f \Delta x_1} \\
&= p_f + \frac{2x_L(p_i - p_f)}{\pi^2 \Delta x} \sum_{n=1}^{\infty} \frac{1}{(n-0.5)^2} \left(1 - \cos \left[(n-0.5)\pi \frac{\Delta x_1}{x_L} \right] \right) \\
&\quad \exp(- (n-0.5)^2 \pi^2 \frac{k}{\phi \mu c x_L^2} t)
\end{aligned} \tag{2.57}$$

For our simulation, discretized Darcy's law for the first grid is

$$q = A_f \frac{k}{\mu} \frac{p_{ave}(0:\Delta x_1, t) - p(0, t)}{d_{m-f}} \tag{2.58}$$

Thus, the equivalent average matrix-fracture distance in the first grid

$$\begin{aligned}
d_{m-f} &= \frac{p_{ave}(0:\Delta x_1, t) - p(0, t)}{A_f \frac{k}{\mu} Q} \\
&= \frac{x_L^2 \sum_{n=1}^{\infty} \frac{1}{(n-0.5)^2} \left(1 - \cos \left[(n-0.5)\pi \frac{\Delta x_1}{x_L} \right] \right) \exp(- (n-0.5)^2 \pi^2 \frac{k}{\phi \mu c x_L^2} t)}{\Delta x_1 \pi^2 \sum_{n=1}^{\infty} \exp(- (n-0.5)^2 \pi^2 \frac{k}{\phi \mu c x_L^2} t)}
\end{aligned} \tag{2.59}$$

2.4.2 Steady or Pseudo-Steady State Analytical Solution

The governing equation of 1D fluid flow of a single-phase single-component slightly compressible fluid in a homogeneous porous medium can be expressed as:

$$\frac{\partial p}{\partial t} = \frac{k}{\phi \mu c} \frac{\partial^2 p}{\partial x^2} \tag{2.60}$$

When fluids flow in this 1D reservoir reaches pseudo-steady state, the rate of pressure drop at each point is the same:

$$\frac{\partial p}{\partial t} = C \tag{2.61}$$

Substituting Eq. (2.61) into Eq. (2.60), we have:

$$\frac{\partial^2 p}{\partial x^2} = \frac{\phi \mu c}{k} C = B_1 \quad (2.62)$$

The general solution for differential equation Eq. (2.62) is

$$p(x, t) = \frac{B_1}{2} x^2 + B_2 x + B_3 + Ct \quad (2.63)$$

where B_1 , B_2 , B_3 and C are four constants.

The partial derivative of p with respect to x from Eq. (2.63) is

$$\frac{\partial p}{\partial x} = B_1 x + B_2 \quad (2.64)$$

At the right boundary, the pressure derivative is zero with the definition of pseudo-steady state:

$$\frac{\partial p}{\partial x}(x_L, t) = B_1 x_L + B_2 = 0 \quad (2.65)$$

Pressure at the left boundary is the fracture pressure:

$$p(0, t) = B_3 + Ct = p_f \quad (2.66)$$

Another boundary condition on the left is based on Darcy's law:

$$\frac{\partial p}{\partial x}(0, t) = B_2 = \frac{q \mu}{k A_f} \quad (2.67)$$

Combining Eq. (2.65) and Eq. (2.67), we have:

$$B_1 = -\frac{q \mu}{k A_f x_L} \quad (2.68)$$

The average pressure in the first grid (with the width of Δx_1) is obtained by the integration over this grid volume:

$$p_{ave}(0:\Delta x_1, t) = \frac{\int_0^{\Delta x_1} p(x, t) A_f dx}{A_f \Delta x_1} = \frac{B_1}{6} \Delta x_1^2 + \frac{B_2}{2} \Delta x_1 + p_f \quad (2.69)$$

Substitute Eq. (2.67) and Eq. (2.68) into Eq. (2.69), we have:

$$p_{ave}(0:\Delta x_1, t) - p_f = \left(-\frac{\Delta x_1}{3x_L} + 1 \right) \frac{q\mu}{kA_f} \frac{\Delta x_1}{2} \quad (2.70)$$

In Eq. (2.70), the ratio of Δx_1 (in the grid-size scale) and x_L (in the reservoir-size scale) is typically very small. Thus, the first term inside the bracket is negligible. By reformulating Eq. (2.70), we can obtain the equivalent average matrix-fracture distance in the first grid:

$$d_{m-f} = \frac{p_{ave}(0:\Delta x_1, t) - p(0, t)}{A_f \frac{k}{\mu} Q} = \frac{\Delta x_1}{2} \quad (2.71)$$

For the steady-state flow, the constant C in Eq. (2.61) becomes zero. The constant B_1 becomes zero correspondingly. In addition, the boundary condition on the right changes from Neumann conditions to Dirichlet conditions. Following the same procedure, we can obtain that the equivalent average matrix-fracture distance for the steady-state flow in the first grid is also half of the grid size.

2.5 Model Validation

Based on foregoing discussions, the calculated geometric information can be immediately implemented into our simulator by taking the advantage of the IFD method. In our developed simulator, the component mass-balance equations are discretized in space with the IFD concept, in which the upstreaming weighting method is applied to the mobility term and the harmonic mean method for the transmissivity term. Time discretization is carried out with a first-order, backward, fully implicit finite-difference method (or backward Euler method). The discrete nonlinear equations are solved via the Newton iteration method (Wu et al. 2014; Wang and Wu

2015; Xiong et al. 2015; Zhang et al. 2016). Three examples are designed, and several simulations are performed to examine the accuracy of the 3D-EDFM algorithm. The first example involves single 2D fracture; the second one contains multiple 2D connected fractures; and the third one is to study a 3D fracture. Benchmark solutions include the approximate analytical solutions from the literature (the first example) and simulation results from two other established numerical approaches (the second and third example).

2.5.1 Single Fracture

Figure 2-9 shows a schematic diagram of the first case. The system contains a horizontal, infinite-acting, homogeneous, and isotropic formation. One vertical well and one vertical hydraulic fracture are put inside this reservoir. The plane of the hydraulic fracture includes the wellbore. It totally penetrates the reservoir formation in the vertical direction. A single-phase, slightly compressible fluid is produced from the well at constant rate. For the infinite fracture conductivity case, the pressure along hydraulic fractures remains equal to the bottom-hole pressure. For the finite fracture conductivity case, the fracture permeability is calculated based on the fracture conductivity value. Parameters are given in Table 2-1. Analytical solution of the well pressure with the infinite- and finite-conductivity fracture are given by Gringarten et al. (Gringarten et al. 1974) and Cinco and Meng (Cinco-Ley and Samaniego 1981; Cinco-Ley and Meng 1988), respectively.

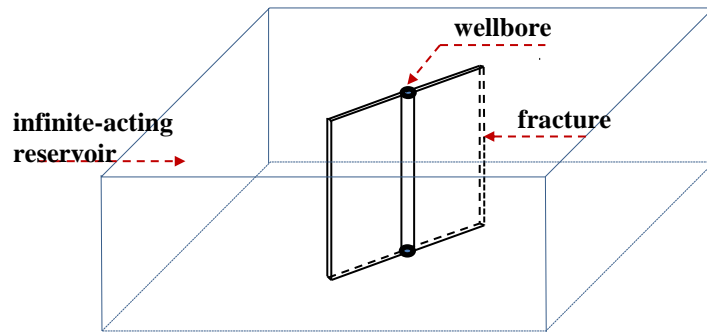


Figure 2-9 Vertical fracture in an infinite slab reservoir

Figure 2-10 presents comparisons between the numerical solutions and analytical (true) solutions with various fracture conductivities. It indicates from low conductivities ($C_{fd} = 0.5$) to high ones ($C_{fd} = 10,000$), all results from the EDFM are in good agreement with the analytical

solution. In numerical models, the reservoir length and width are fifteen times of the fracture length to approximate the “infinite-acting” set-up. The minor discrepancy for some cases in the very early time is because the fracture volume in the analytical approach is set to be zero, while this volume should be given a non-zero value in the numerical approach.

Table 2-1 Synthetic model parameters for numerical model validations

Parameters, Units	Values
Fracture half-length, m	5.00
Reservoir permeability, m ²	9.87E-16
Porosity	0.05
Fluid viscosity, Pa*S	8.90E-04
Total compressibility, 1/Pa	4.58E-10
Initial pressure, Pa	4.14E+07
Production rate, m ³ /s	2.00E-06
Reservoir length, m	150
Reservoir width, m	150
Reservoir thickness, m	1.0

Figure 2-11 shows the sensitivity analysis of the EDFM with respect to the grid size. Comparison results from Figure 2-11 indicate that numerical results are in good agreement with the analytical solution for this problem with a grid size of 1 m and 2 m. For the grid size of 5 m and 10 m, some discrepancies are observed when the dimensionless time is smaller than 0.2, which is 0.65s in real time for this problem. Numerical results are acceptable after this point of time. This discrepancy comes from the difference between transient state flow (real) and steady state flow (numerical approach assumption) inside the grids which contains fractures in the very early time. For most of the simulation cases, however, the interested time interval is far larger than this short time. In addition, this discrepancy can be eliminated if the local grids are refined with the 2m grid, as shown in the case of the 10 m grid with 2 m LGR in Figure 2-11.

Figure 2-13 shows simulation results by rotating the vertical fracture with various angles. Two-meter grid is used for all these simulation cases. Though the fracture geometry (length, width, and height) in these cases stay the same, the number of intersected grids, intersection areas for various grids, and the average distance in these numerical cases are different (see Figure 2-12). Simulation results are shown to be almost the same since the reservoir size is much larger than the fracture size. All these numerical simulation results are in good agreement with the analytical solution, which demonstrates the ability of the method to handle fractures with arbitrary directions.

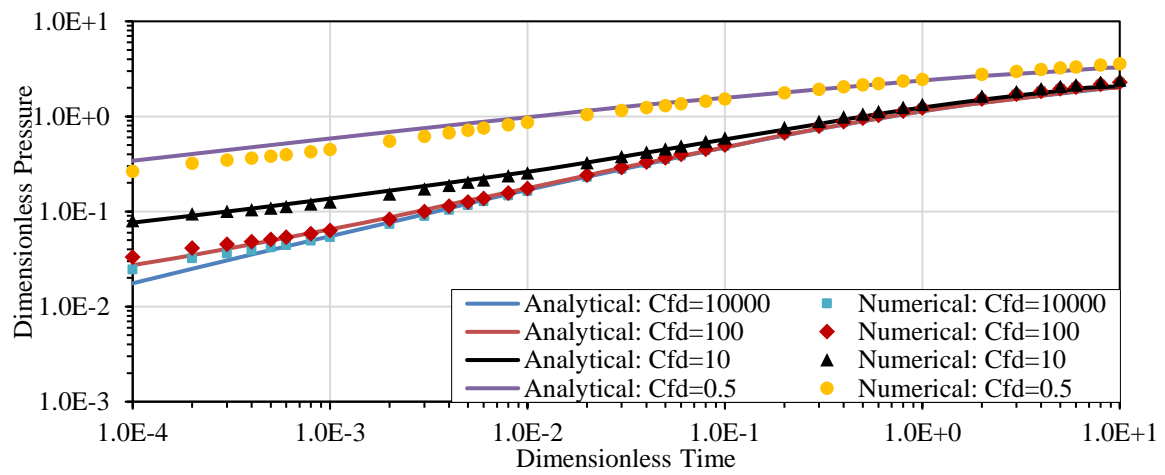


Figure 2-10 Comparisons of wellbore pressure vs. time between the analytical solution (“Cinco-Samaniego” type curve), and numerical solution with various fracture conductivities

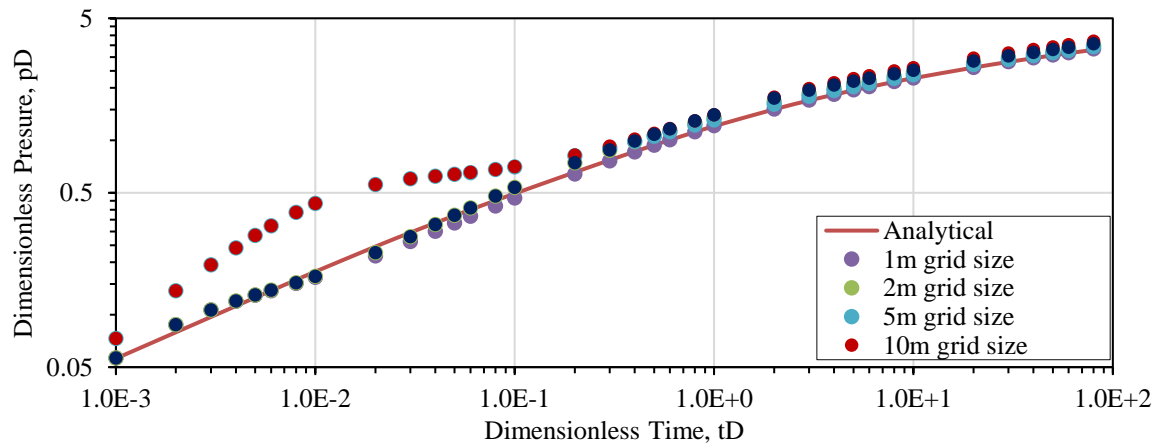


Figure 2-11 Comparisons of wellbore pressure vs. time between the analytical solution, and numerical solution with various grid sizes for infinite fracture conductivity

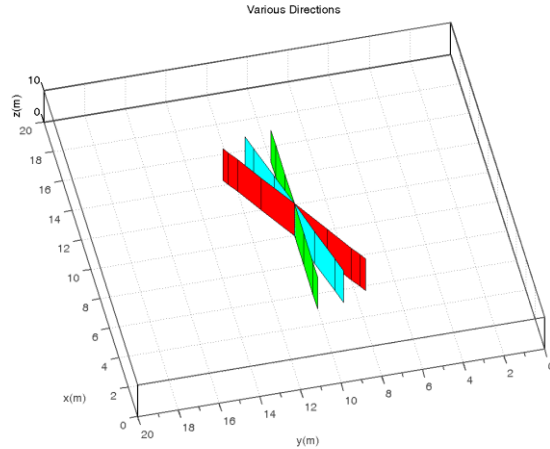


Figure 2-12 Cases with various fracture directions and their associated EDFM grids (0, 15 and 30 degrees)

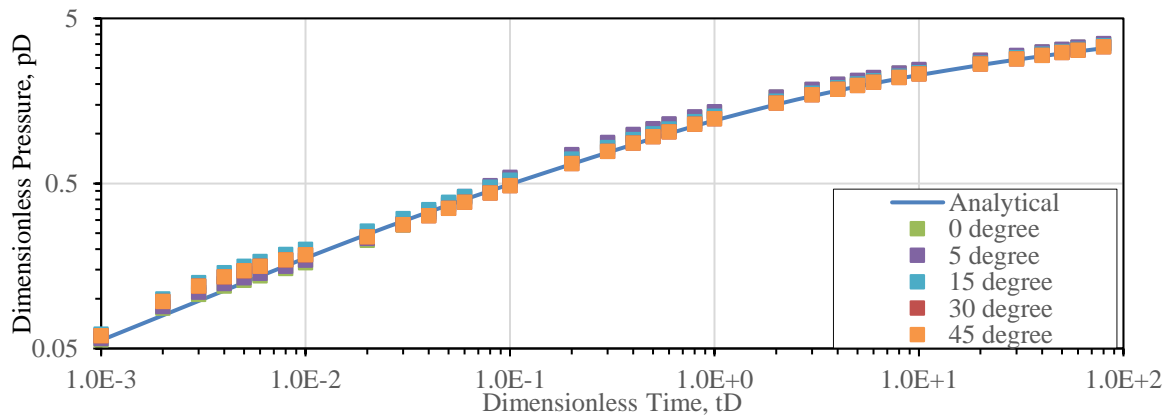


Figure 2-13 Comparisons of wellbore pressure vs. time between the analytical solution, and numerical solution with various fracture orientation for infinite fracture conductivity

2.5.2 Multiple Fractures

This section examines the validity of EDFM to handle multiple connected fractures. A simple synthetic 2D model containing four fracture branches (28 fractures in total) is built as shown in Figure 2-14. The infinite conductivity condition is assumed in this validation example. The initial reservoir pressure is 8,000 psi, and this reservoir is under production with constant BHP control (2,000 psi) for 30 months. For this problem, fractures are handled explicitly using three different approaches: the local grid refinement method, the unstructured grid method (triangular grids for 2D cases), and the EDFM (Figure 2-15). The first two approaches are well established as discussed in Section 2.1. Figure 2-16 displays the simulation results for these

cases. We observed that the EDFM results are nearly indistinguishable from the reference LGR and triangular grid methods.

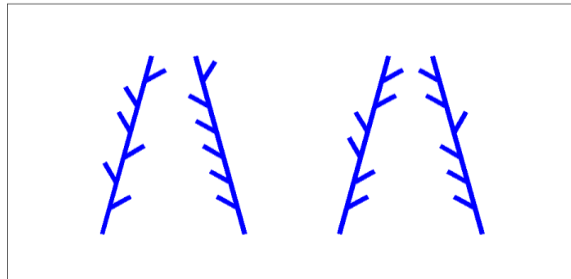


Figure 2-14 Synthetic 2D model with 4 fracture branches

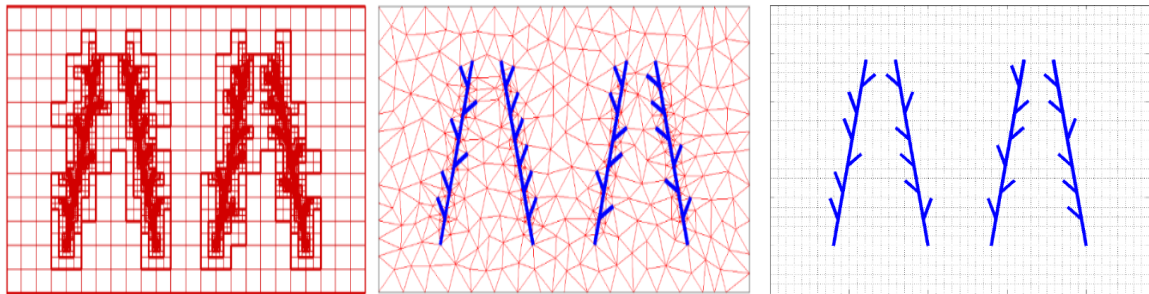


Figure 2-15 Space discretization for three different fracture simulation methods (from left to right: LGR, triangular grids, and EDFM)

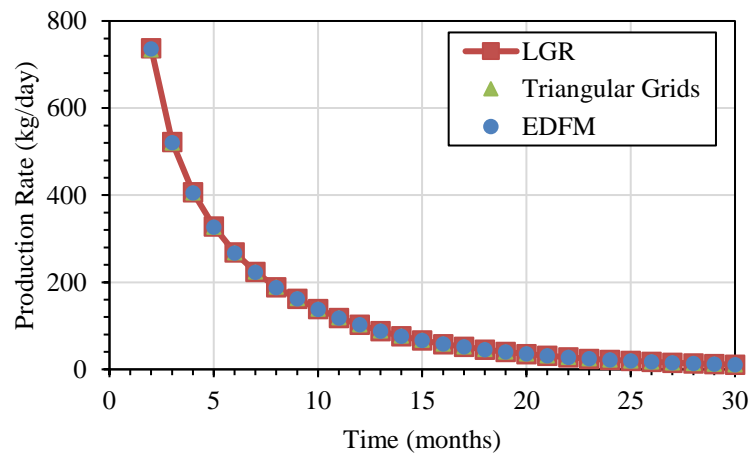


Figure 2-16 Oil production rate results for three solutions for synthetic 2D flow

In the problem, the EDFM shows a better computational efficiency for the simulation with the default solver in our simulator (DSLUCS, a Lanczos-type bi-conjugate gradient solver).

As shown in Table 2-2, the number of cells and connections for the EDFM is much less than other two methods. For this example, the EDFM provides about 15 times speed up relative to the reference LGR method and 3.6 times speed up relative to the triangular grid method. This enhanced performance results from the decrease of Jacobian matrix size and complexity. Solving the Jacobian matrix related linear algebra is the single-most time consuming part in reservoir simulation. As shown in Figure 2-17, the LGR method leads to an irregular seven band sparse Jacobian matrix with the size of $10,120 \times 10,120$. The triangular grid method has a relatively dense matrix with the size of $6,800 \times 6,800$. The EDFM has a five diagonal band sparse Jacobian matrix with the size of $1,601 \times 1,601$, which has a similar sparsity pattern with the traditional simulation approach.

Table 2-2 Comparison of problem size and simulation times for these three approaches

	Number of Cells	Number of Connections	Simulation Time (s)
LGR	10120	66482	435.16
Triangular Grids	6800	10480	101.55
EDFM	1601	8197	28.17

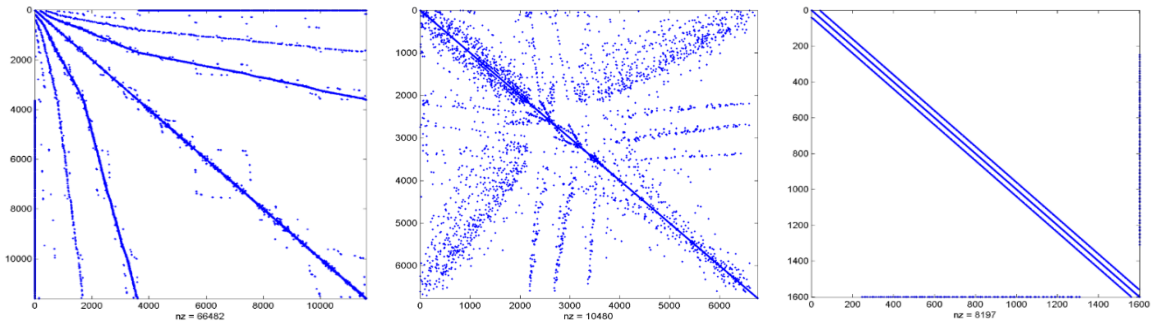


Figure 2-17 Comparison of Jacobian matrix size and complexity of these three approaches (from left to right: LGR, triangular grids, and EDFM)

2.5.3 3D Circular Fracture

In this section, we attempt to examine the validity of the proposed approach in computing fluid flow with 3D fractures, by comparing model results with those from the LGR approach.

Consider a circular fracture of radius $r = 5\text{m}$ inside a closed-boundary cube with dimensions of $40\text{m} \times 40\text{m} \times 40\text{m}$. This fracture has a uniform width of 0.01m and a permeability of $4.9345 \times 10^{-11}\text{m}^2$. Fluids are produced from the fracture center with constant rate $(5.0 \times 10^{-7}\text{ m}^3 / \text{s})$. All other simulation parameters keep the same with the first validation example as described in Table 2-1. Both 3D-EDFM and LGR meshes have grid refinement towards the fracture (Figure 2-18). In y- and z- directions, refiner grids are used in the LGR (0.5m) compared with those used by EDFM (1m), aiming to capture the fracture boundary. In x-direction (normal to the fracture plane), grid size starts from 0.01m (the fracture width) in the mid and grows exponentially on both sides in LGR; whereas the grid size in 3D-EDFM is 5.0m with a 1.0m refinement for grids containing the fracture. Figure 2-19 compares the absolute change of the pressure at the fracture center vs. time. The 3D-EDFM results are observed to be in a good agreement with the benchmark solution. Figure 2-20 shows the 3D contour of the simulated pressure profile at $2,065\text{s}$ through the 3D-EDFM approach.

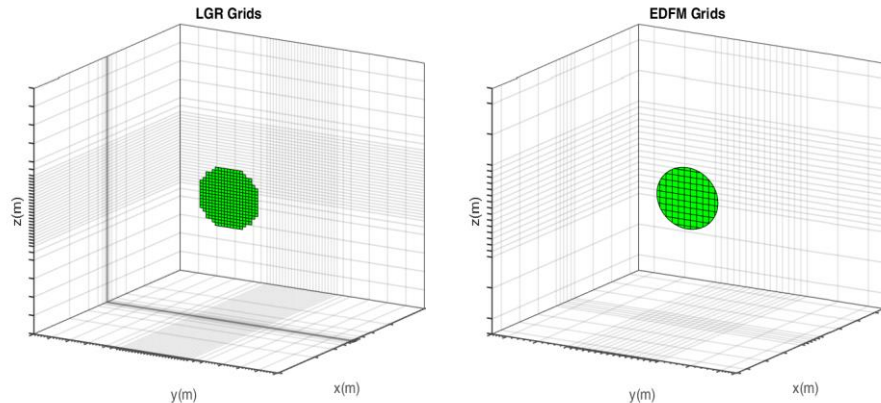


Figure 2-18 Space discretization for the 3D circular fracture (left: LGR methods, right: EDFM)

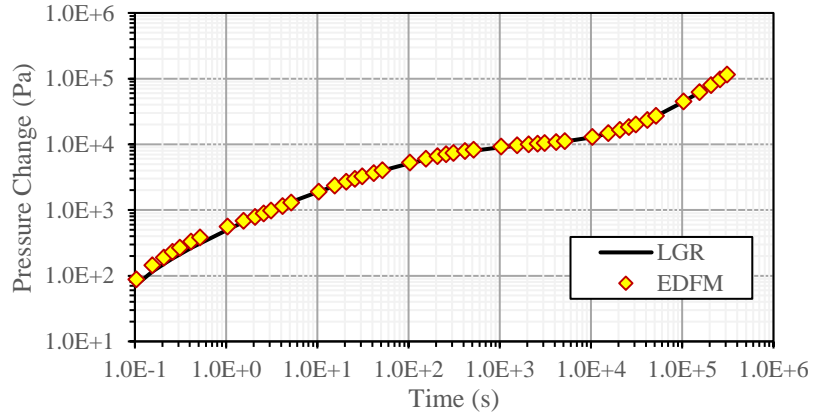


Figure 2-19 Simulated bottle hole pressure vs. time with LGR and EDFM methods

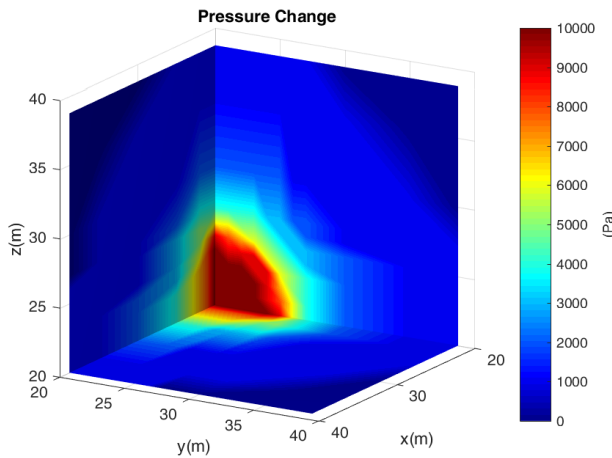


Figure 2-20 3D contour (a quarter view) of pressure change at 2,065s

2.6 Application

The EDFM method is here applied to three problems that are of special interest in unconventional reservoirs. We present simulations results with (1) fractures with complicated shapes due to the multi-layer features and vertical heterogeneity, (2) multiple curved fractures due to the stress shadow effect, and (3) multiple arbitrary-direction fractures with complicated connections due to the hydraulic fracture and natural fracture interactions. The first problem is described in detail, and the other two are relatively illustrative. The major objective of these three examples is to demonstrate the capacity of the EDFM to capture all of the common phenomena related to complicated fractures in developing unconventional reservoirs. Note that single-phase flow is involved in most simulated cases, a two-phase flow is added into the third

problem. The 3D-EDFM method can be directly applied for the first two cases with multi-phase fluid flow because gridding and handling fluid flow physics are two independent modules under our numerical scheme.

2.6.1 The Multi-Layer Case

The hydraulic fracture shape in unconventional reservoir formations will most likely deviate from the classical, ideal bi-wing shape in conventional reservoirs (Zhou 2016). This results from the multiple layer features or formation heterogeneity that are observed in many unconventional reservoirs (Passey et al. 2010; Donovan et al. 2012; Hart et al. 2013). Since the geomechanical and fracturing properties, such as elastic modulus, fracture toughness, and leak-off coefficients, vary distinctly among these layers, created hydraulic fracture widths and lengths in different layers are significantly different.

Figure 2-21 (the left part) shows such a hydraulic fracture with complicated shapes from geomechanics simulations (Zhai and Fonseca 2015; Geilikman et al. 2015). The color contour indicates local variations of the fracture width. As shown in the right part of Figure 2-21, the reservoir containing this fracture is assumed to be rectangular with dimensions of $200 \text{ m} \times 300 \text{ m} \times 120 \text{ m}$. This is a closed-boundary reservoir. It is subdivided into regular grids of 1,800 blocks with dimensions of $20 \text{ m} \times 20 \text{ m} \times 10 \text{ m}$. These grid blocks are visualized on the surfaces of the reservoir box.

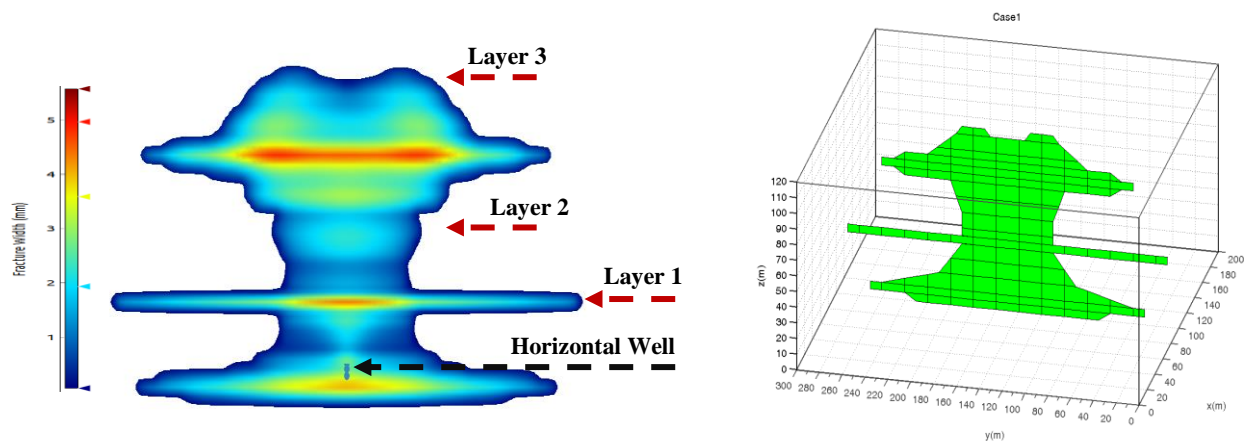


Figure 2-21 Left: Illustrations of a hydraulic fracture with complicated shapes from geomechanics simulations. Three layers are selected to demonstrate our simulated flow patterns inside the reservoir. Right: Discretization grids for the reservoir and the embedded fracture

The fracture is embedded into these regular grids, leading to 1,899 computational grids (1,800 matrix grids and 99 fracture grids), and 5,239 computational connections (4,950 matrix-matrix connections, 99 matrix-fracture connections, and 190 fracture-fracture connections). The horizontal well connects with one fracture grid in the mid-lower part, as illustrated in the left part of Figure 2-21.

In our simulation, the fracture permeability is correlated from the fracture width following the cubic law ($k_f = w_f^2 / 12$). The lateral reservoir permeability is given a value of 0.1mD. The vertical reservoir permeability is assumed to be one tenth of this value to account the layering effect. The estimation of the dimensionless fracture conductivity indicates that this fracture cannot be treated with infinite conductivities. The initial reservoir pressure is 6,000 psi, and this reservoir is depleted with a constant BHP of 1,000 psi. Fluids in this system are in the single phase with the viscosity of 1.0 cp and the compressibility of 4.58E-10 Pa⁻¹.

The lateral (y-z) view of the pressure distribution inside the fracture at 1.0 day is shown in Figure 2-22, which indicates fluids within the fractures travels towards the wellbore. It has a pseudo-radial flow pattern close to the wellbore and a linear flow pattern away from the wellbore. This flow pattern is controlled by both the distance from the wellbore and the fracture shape.

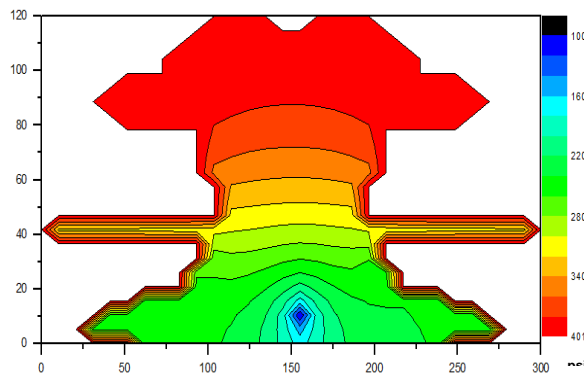


Figure 2-22 The lateral (y-z) view of the pressure distribution inside the fracture at 1.0 day

Fluid flow inside the fracture is feed by fluids from the reservoir. Three layers (shown in Figure 2-21) are selected to demonstrate our simulated flow patterns inside the reservoir. These three layers are penetrated with hydraulic fractures by different lengths. Figure 2-23 shows the

top (x-y) view of contour lines of pressure for these three layers at 10.0 days. For the first one, the fracture extends nearly to the reservoir drainage boundary. Our simulation results (the left one in Figure 2-23) tell this layer of reservoir feeds the fractures via linear flow instead of pseudo-radial flow. It matches the analytical study in literature (Wattenbarger et al. 1998). For the second layer, in which the fracture length is about one-third of the reservoir width, simulated contour lines inside can be described using an elliptical geometry (the mid one in Figure 2-23). This elliptical pattern of the propagating pressure transient matches the analytical solution by Hale and Evers (1981). The third layer connects with two relatively short fracture segments. Simulated pressure contour lines can be described as two sets of ellipses with shorter focal lengths surrounded by one set of longer focal-length ellipses (the right one in Figure 2-23). Furthermore, in this highly anisotropic reservoir, flow towards the hydraulic fracture is mainly along the horizontal direction, and there are little vertical flow crossing layers.

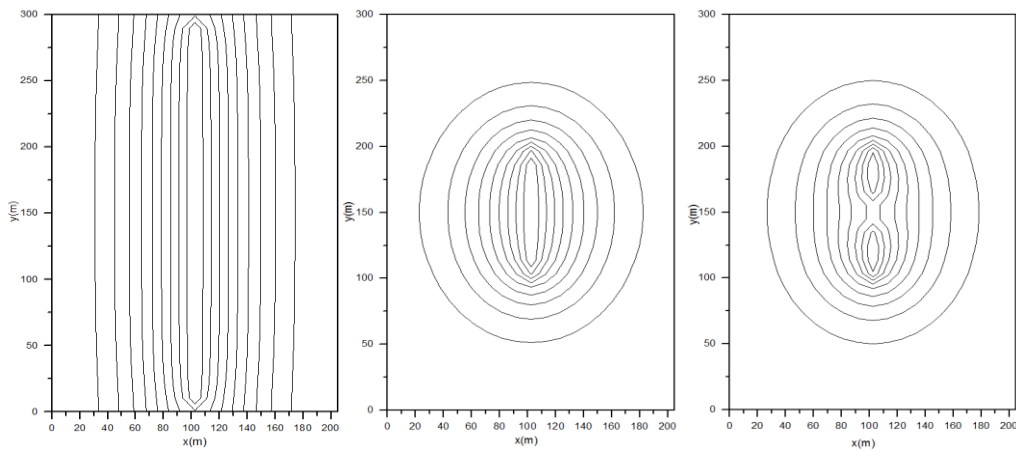


Figure 2-23 The top (x-y) view of contour lines of pressure for these three layers at 10.0 days

2.6.2 The Stress Shadow Case

Hydraulic fractures open in the minimum stress direction and extend perpendicular to this direction. For multistage hydraulic fracturing (fractures generated either simultaneously or sequentially), the creating and propping of other fractures will change the in-situ stress and create a corresponding stress-shadow regime. The direction of the minimum in-situ stress rotates in this stress-shadow regime. If one fracture is located inside the stress-shadow regime of a nearby fracture or nearby fractures, it will propagate following a curved track (Wong et al. 2013).

This example is to demonstrate the capability of the EDFM of handling curved fractures. Curved fractures can be represented by a set of connected 3D convex polygons. As shown in the left part of Figure 2-24, each hydraulic fracture is broken down to three rectangles. The discretized form of these four fractures after embedment is shown on the right part of Figure 2-24. These fractures full penetrate the reservoir in the vertical direction. If the fracture conductivity is infinite, this problem can be simplified into a 2D problem in numerical simulation. All other reservoir properties keep the same with the first case. Figure 2-25 shows the top view of simulated pressure distribution after one day and one month. From the simulation results, pressures in the inner reservoir part (the portion of the reservoir between two adjacent fractures) drop faster than that in the outer reservoir part.

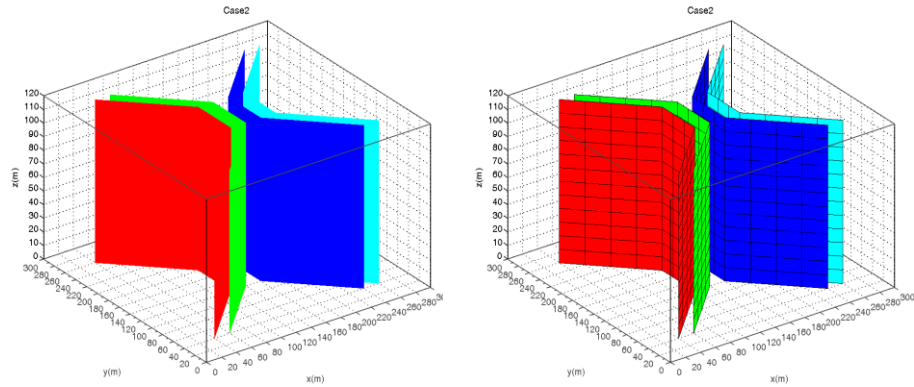


Figure 2-24 left: Illustrations of four curved hydraulic fractures due to the stress shadow effect.
right: Discretization grids for the reservoir and the embedded fractures

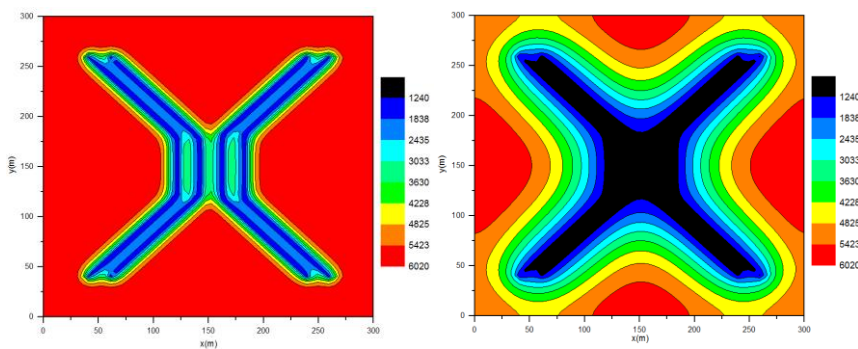


Figure 2-25 The top (x-y) view of the pressure distribution at 1.0 day and 1.0 month

2.6.3 The Natural Fracture Interaction Case

The microseismic data may give some information on that the fracture shape involves not only a single isolated planar fracture, but also has irregular traces with a fractured zone around (Fisher and Warpinski 2012; Geilikman et al. 2015). Small fractures in the fracture zone are originally natural fractures which are partly open or sealed under natural condition. The sealed fractures cannot contribute to permeability enhancement initially but act as planes of weakness and reactive during drilling or hydraulic fracturing (Gale et al. 2007; Olson and Taleghani 2009). Considering these complicated fracture geometries will improve simulation results in a more realistic and accurate way.

Figure 2-26 shows three DFNs generated from the same set of microseismic data considering distance uncertainties by use of Hough transforms (Yu et al. 2016). These DFNs are extracted from figures in Yu's publication. Complexities of this fracture network come from interactions with natural fractures during hydraulic fracture propagation. In this problem, all activated fractures are assumed to be propped and act as effective high-conductivity pathways for fluid production. Fracture widths are given a uniform value of 0.01m, and the effective fracture permeability is assumed to be $4.9345 \times 10^{-10} \text{ m}^2$. Matrix permeabilities in three directions are $9.87 \times 10^{-18} \text{ m}^2$. The reservoir under consideration is the area associated with only one stage of hydraulic fractures, which is represented by a closed-boundary rectangle, $20\text{m} \times 20\text{m} \times 14\text{m}$ in extent. Grid dimensions are $0.5\text{m} \times 0.5\text{m} \times 0.5\text{m}$. All other simulation input parameters keep the same with the case in section 5.1. Note that the two-dimensional (or 2.5D) fracture handling approach is not applicable for this case, because most fractures are not aligned with grid axes. The 3D-EDFM discretization of these fractures leads to a combination of triangles, quadrilaterals, pentagons and hexagons. Details about the discretization results are listed in Table 2-3.

Two sets of reservoir simulation studies are conducted. The first involves single-phase fluid flow with these three DFNs. Figure 2-27 presents horizontal slices of the simulated pressure-change contour for case 1 at 1,038s and 12,960s, which shows pressure depletion patterns with thirteen fractures are qualitatively captured.

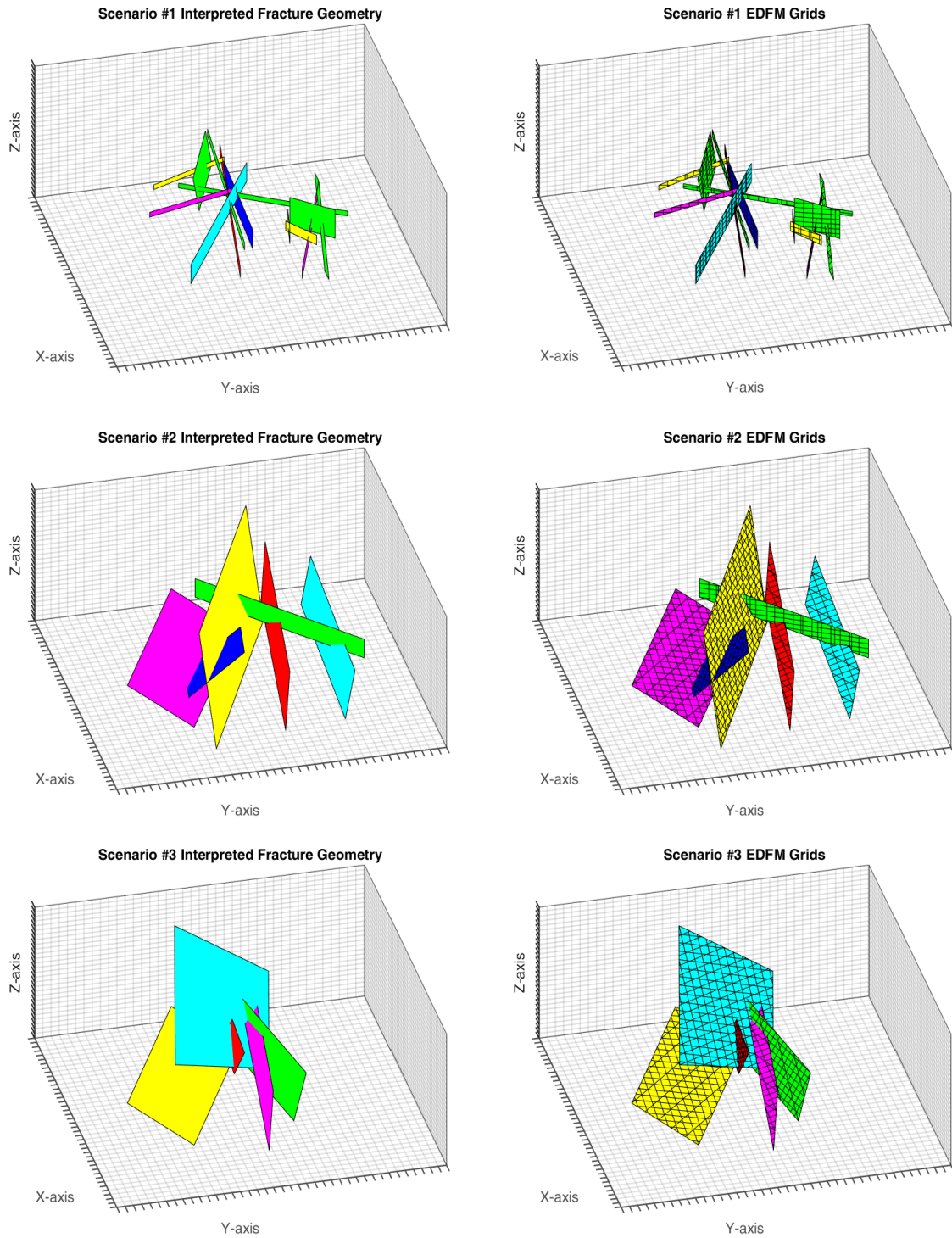


Figure 2-26 Three DFN geometries (left) and corresponding 3D-EDFM grids (right)

Quantitative analysis is presented in Figure 2-28 and Figure 2-29. Figure 2-28 plots the simulated production rate vs. time in the log-log scale, following the routine of rate transient analysis (RTA). Simulation results indicate that linear fracture flow is the dominate flow regime in the early time in these three cases (slopes of curves are close to -1/2), followed by a boundary dominated flow regime. This matches with physics, in turn, proves the effectiveness of the 3D-EDFM to handle complicated 3D fractures. Figure 2-29 plots the area-normalized production rate (production rate divided by the total fracture area) vs. time. Fracture area data can be referred in Table 2-3. These three curves coincide in the early time, and this coincidence indicates that the most sensitive parameter of hydraulic fractures to early transient fluid flow through extremely low permeability matrix rock is the fracture-matrix contacting area, no matter how complicated the fracture geometry is. Based on this observation, it is possible to use rate transient testing data to estimate the effective area of fractures even for 3D complicated fractures.

Table 2-3 Information of the fracture geometry and EDFM gridding for these three cases

Cases	Fracture Number	Fracture Area (m^2)	Fracture Connection Number		Fracture Grid Number			
			M-F	F-F	Trian	Quadra	Penta	Hexa
No. 1	13	100.3	707	1751	132	660	72	6
No. 2	6	225.7	1548	2931	602	516	483	35
No. 3	5	176.2	1125	2184	446	464	251	68

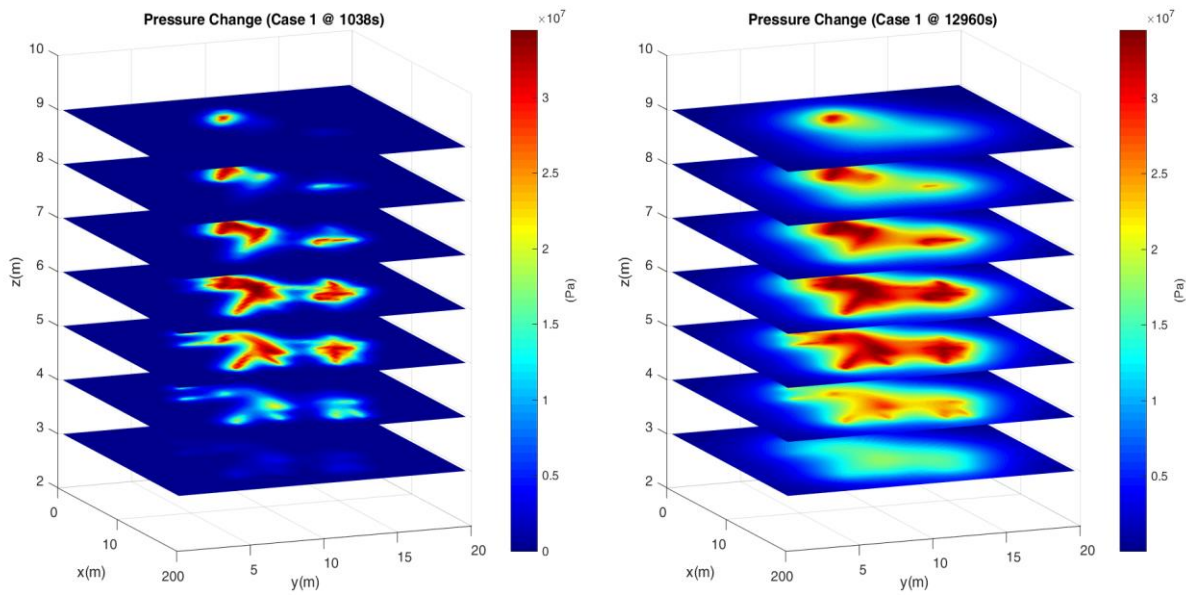


Figure 2-27 Horizontal slices of simulated pressure contours for case 1 at 1038s (left) and 12,960s (right)

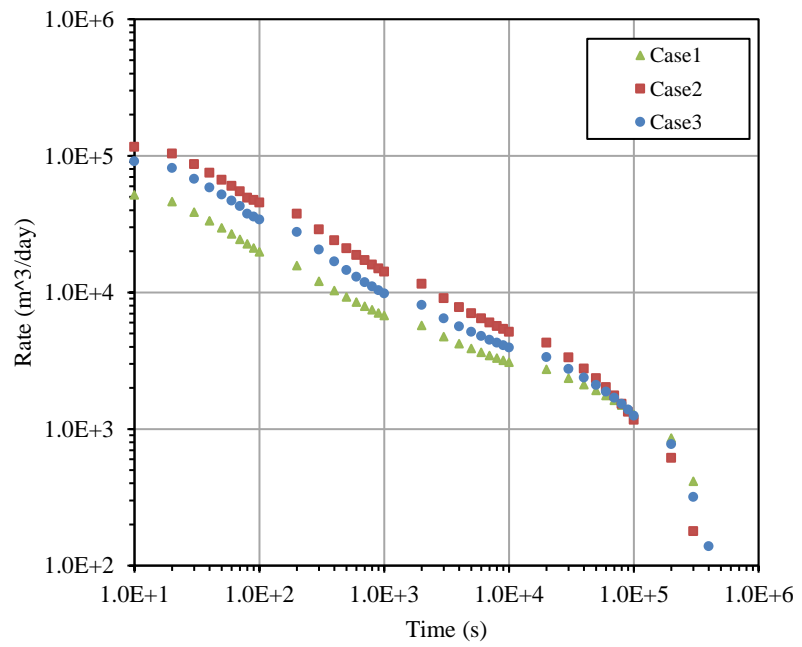


Figure 2-28 Simulated production rate vs. time (log-log scale) for these three cases

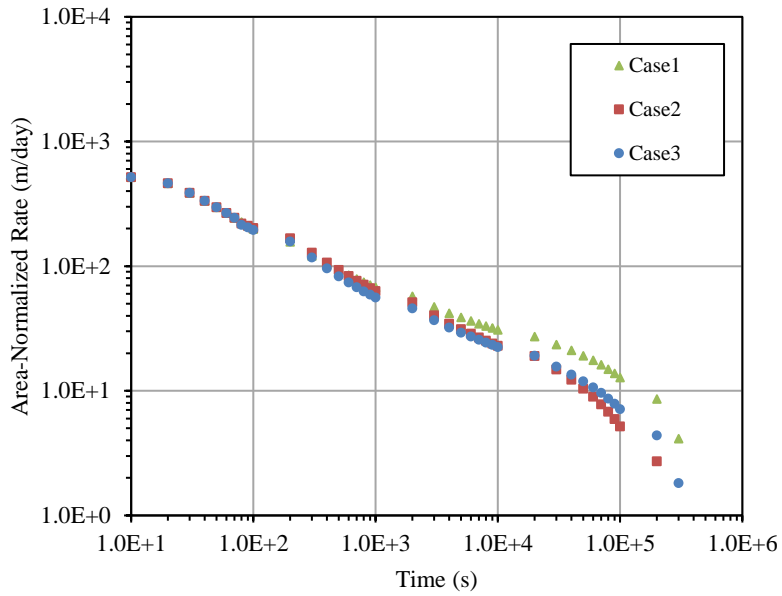


Figure 2-29 Simulated area-normalized production rate vs. time (log-log scale)

Two-phase flow (gas and water) is also investigated using the DFN in case 2. Two simulation cases are designed to evaluate the impact of spontaneous imbibition or injection into matrix of fracturing fluids on post-fracturing production. In these two cases, the initial water saturation in matrix is set at the residual value (0.45), while the water saturation in fractures is 1.0. Initial pressure in matrix and fractures keep the same. Reservoir rocks are assumed to be water-wet, which is modeled by capillary pressure and relative permeability as shown in Figure 2-30. The well is shut in for a while before turns on production with a constant BHP. Shut-in time varies in these two cases: no shut-in time in case 1 and one week in case 2. The simulated water saturation profile after one-week shut-in, with a range between 0.45 and 0.60, is shown in Figure 2-31. Simulated gas production rate and accumulative water production from these two cases are presented in Figure 2-32 and Figure 2-33, respectively. From Figure 2-32, the gas flow rate in case 2 is higher in the very early time. This is because most of the produced gas in this period is from fractures, and certain amounts of gas originally in matrix is displaced and flows into fractures by water imbibition during the shut-in (Fakcharoenphol et al. 2013). When gas produced from matrix becomes dominant, gas flow rate in case 1 becomes higher as the imbibed water forms a blockage by reducing the gas-phase relative permeability (Farah et al. 2017). From Figure 2-33, the simulated cumulative water production from case 2 is only about 50% of that

from case 1. This numerical simulation study supports observations from the field that typically only 10% to 50% of fracturing fluids can be recovered (Zhou et al. 2014).

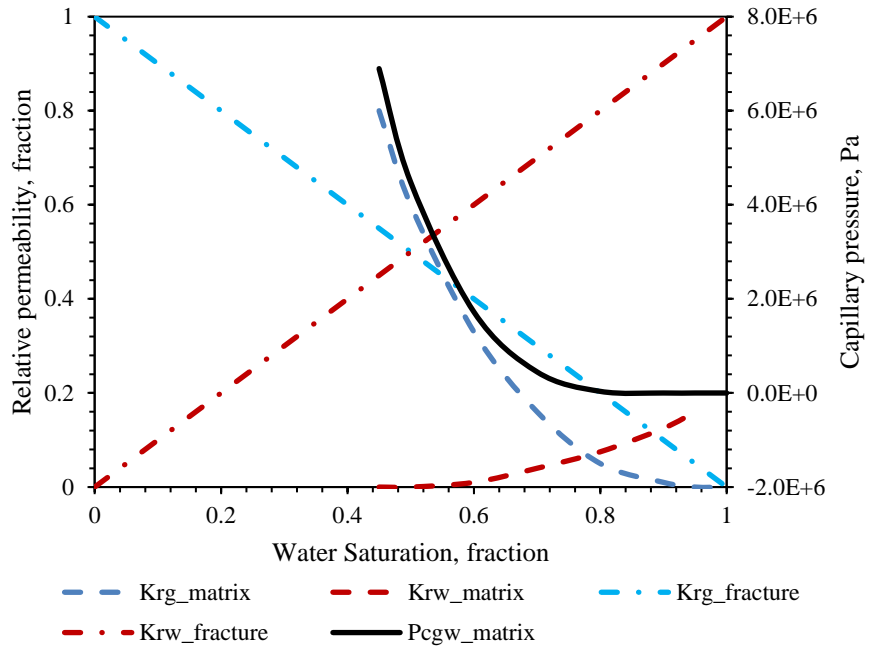


Figure 2-30 Relative permeability and capillary pressure for two-phase flow simulation

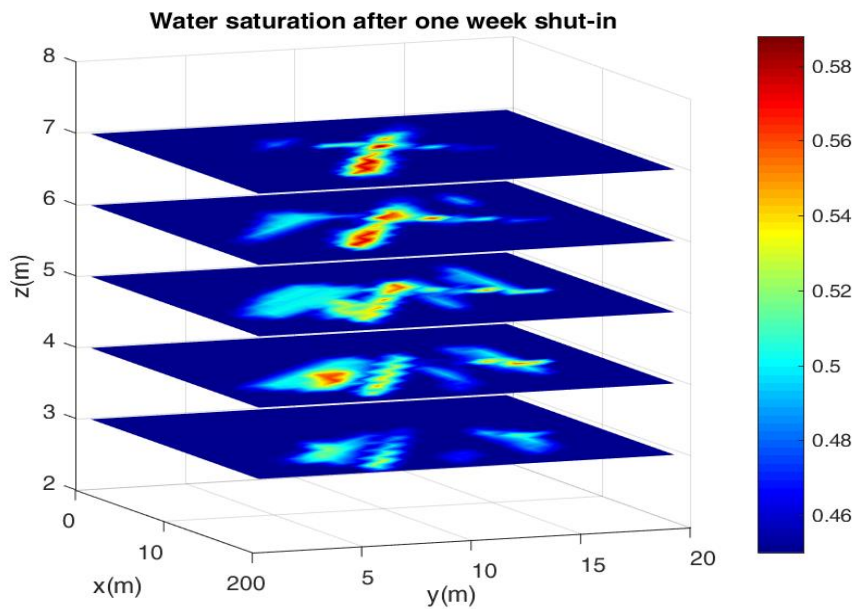


Figure 2-31 Water saturation profiles after one-week well shut-in

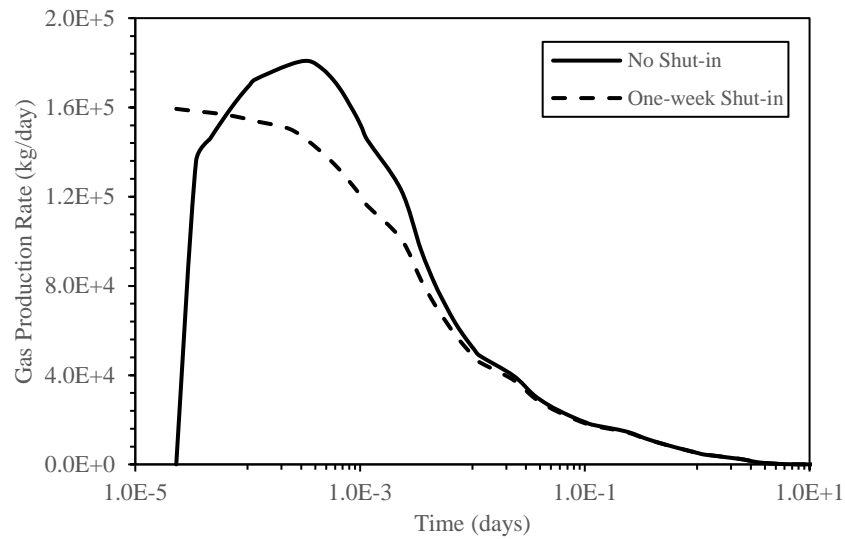


Figure 2-32 Simulated gas production rate vs. time

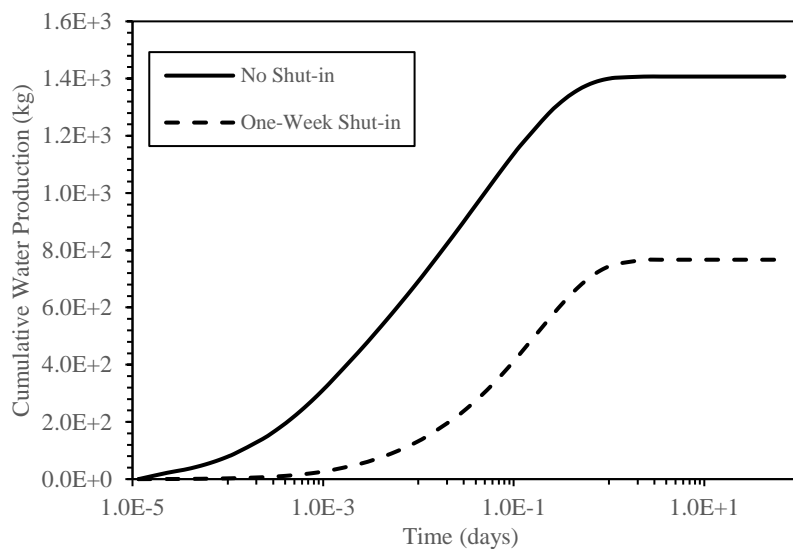


Figure 2-33 Simulated cumulative water production vs. time

2.7 Summary

1. In this chapter, we present a 3D-EDFM method, which is applicable of modeling 3D complicated hydraulic fractures in reservoir simulation. The 3D-EDFM is generally able to handle 3D hydraulic fractures with arbitrary strike and dip angles, shapes, curvatures, conductivities, connections, and number of discrete fractures. In addition, it provides

significant improvement in computational efficiency because of the decrease in Jacobian matrix size and the similarity in matrix sparsity pattern.

2. In the proposed 3D-EDFM, 3D complicated hydraulic fractures are handled by a geometric methodology in gridding for an unstructured-grid reservoir simulator. Our analysis indicates that the geometric-based parameters are reliable to represent flow-based parameters. With these preprocessed grid parameters, the 3D-EDFM can be directly implemented into reservoir simulators via the integral finite difference (IFD) method.
3. The 3D-EDFM is verified by comparison with the Gringarten analytical solution for fluid flow with a single fracture of infinite conductivity and arbitrary directions, with the Cinco-Samaniego type curves for fluid flow with a single fracture of finite conductivities, with two other DFM models for fluid flow with multiple connected fractures as well as with the LGR approach for 3D fractures.
4. The 3D-EDFM is flexible of handling hydraulic-fracture input data, as interpreted from geomechanics modelings as well as microseismic data. Several synthetic, but realistic testing cases are simulated. The 3D-EDFM captures key flow patterns qualitatively and quantitatively, inside both fractures and reservoirs, related to complicated fractures in these cases. For the layer in which the fracture extends nearly to the reservoir drainage boundary, fractures are feed via linear flow. For shorter fractures, pressure contour lines can be described using an elliptical geometry. In addition, the most sensitive parameter of hydraulic fractures to early transient fluid flow through extremely low permeability rock matrix is the fracture-matrix contacting area, no matter how complicated the fracture geometry is.

CHAPTER 3

A MULTI-POROSITY, MULTI-PHYSICS MODEL TO SIMULATE FLUID FLOW IN NUNCONVENTIONAL RESERVOIRS

Gas flow in shales is complicated by highly heterogeneous and hierarchical rock structures, which ranges from organic nanopores, inorganic nanopores, less permeable micro-fractures, more permeable macro-fractures to hydraulic fractures. The dominant fluid flow mechanism varies in these different regimes. Although traditional single-porosity and double-porosity models can simulate certain time range of reservoir performance with acceptable accuracy, they are not applicable for the long-term predictions and have limitations to a more detailed understanding of such fluid flows. In this chapter, we present a multi-domain, multi-physics model, aiming to realistically simulate the fluid flow in shale gas reservoirs considering its heterogeneous and hierarchical rock structures.

A more physics-based conceptual model has been developed, which contains five flow regions: organic nanopores, inorganic nanopores, local micro-fractures, global natural fractures, and hydraulic fractures. Fluid flow governing equations varies according to their different dominant mechanisms. For example, the apparent permeability, which is the intrinsic permeability multiplied by a correction factor, is used to account for the gas slippage effect for fluid flow through nano-scale porous media. On contrast, high-velocity fluid flows in natural fractures and hydraulic fractures are described by the non-Darcy flow equations. For another example, the organic and inorganic nanopores have different gas storage capacities considering gas adsorption/desorption effects.

Numerical studies with practical interests are discussed. One synthetic, but realistic test case is simulated. Input parameters in this case are evaluated using both the laboratory and theoretical analysis data. Our results demonstrate that this model can capture the typical production behavior of unconventional reservoirs: a great initial peak of the production rate, a sharp decline in the first few months, followed by a long flat production tail.

3.1 Introduction

Shale gas refers to the natural gas trapped in shale formations. With technical progresses in horizontal drillings and hydraulic fracturing, these previously unprofitable resources are converted into profitable ones with great commercial values, and they are believed to be an important part of the future energy mix within the US and around the world.

For these reservoirs, similar to conventional reservoirs, numerical modeling of fluid flow in subsurface is an effective tool for the reservoir management. The traditional reservoir simulation, which is a relatively mature technology since the 1960s, has been applied to shale gas reservoirs for this purpose. Although classical single-porosity and double-porosity models can simulate certain time range of reservoir performances with acceptable accuracy, they are not generally applicable for the prediction of long-term performance.

Gas flow in shales is complicated by the highly heterogeneous and hierarchical rock structures (i.e., ranging from organic nanopores, inorganic nanopores, less permeable micro-fractures, more permeable macro-fractures to hydraulic fractures). Figure 3-1 and Figure 3-2 illustrates gas flow pathways in multiple scales for conventional reservoirs and shale gas reservoirs, respectively. Compared with conventional reservoirs, shale gas reservoirs are much more heterogeneous and hierarchical. Its gas flow network consists of different constituents that communicate with each other, which includes hydraulic fractures, macro-scale natural fractures, micro-scale natural fractures, organic porous media, and inorganic porous media. These constituents vary in shapes, characteristic lengths, flow conductivity, spacing/density and host materials, and thus they contribute to the gas flow with different levels of importance. Key geological parameters of these constituents are introduced in the following parts.

Hydraulic fractures dominate gas flow regimes in the reservoir scale. These human-made fractures are typically one or two orders of magnitude larger than naturally existed fractures regarding lengths and heights. Effective (producing) hydraulic fracture length is estimated to be several hundred meters by various characterization techniques (e.g., fracture modeling, PDA, PTA, and reservoir simulation) (Fisher et al. 2004; Cipolla et al. 2008; Wang and Wu 2015). Fracture heights are in the same length scale and varies in different shale formations (Abou-Sayed, and Clifton 1978; Jeffrey and Bunger 2009). Fracture shape involves not only a single

isolated planar fracture but has irregular traces with a fractured zone around it (Warpinski, 2011; Geilikman et al. 2015).

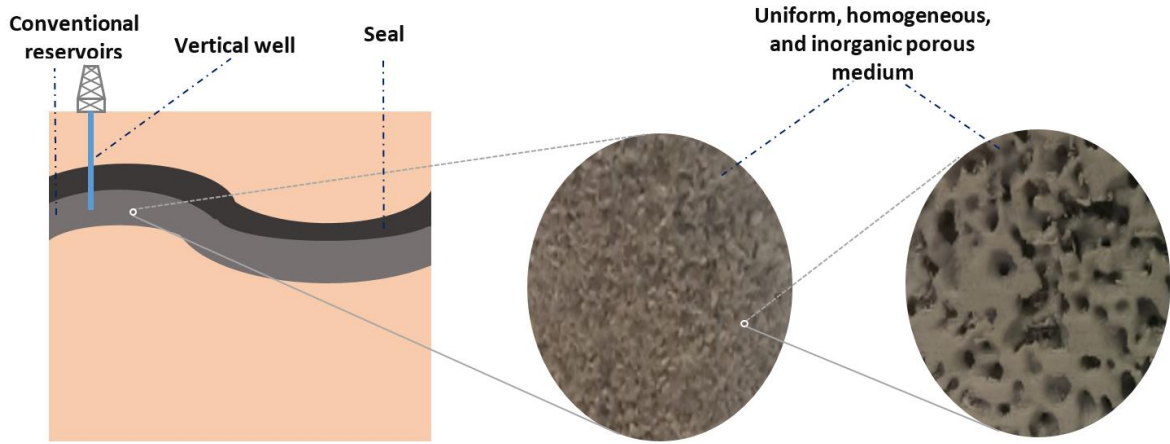


Figure 3-1 Multi-scale illustration of conventional reservoirs: gas flow network is relatively uniform and homogeneous inorganic porous medium

Macroscale natural fractures are ubiquitous in shale gas reservoirs based on two evidences. First, these fractures are observed in most shale outcrops, cores, and image logs (Gale et al. 2007; Ahmed et al. 1991; Bryant and Flint 2009). Secondly, numerical modeling typically requires the apparent permeability 2 to 4 orders of magnitude higher than the core permeability to match rates and ultimate recoveries (Walton and McLennan 2013). For macroscale natural fractures in various shales, their spacing is reported to be between 0.5m and 10m (Engelder, et al. 2019). Fracture aperture sizes are measured to follow a power-law distribution and are in the considerably narrow size range of between 30 um and 1 mm (Gale et al. 2014). These narrow fractures can be partly open or sealed under natural conditions. The sealed fractures cannot contribute to permeability enhancement initially but can act as planes of weakness and reactive during drilling or hydraulic fracturing (Gale et al. 2007; Olson and Taleghani 2009). Though macroscale natural fractures contribute negligibly to the pore volume of the reservoirs (cumulative fracture porosity ranges from 0.0003 – 0.0005%), their presence is one of the most critical factors in defining the economics of shale gas play (Walton and McLennan 2013). This is because macroscale natural fractures provide a high-conductivity path to convey hydrocarbons from the tight matrix to producing wells.

Microfractures refer to fractures visible only under magnification. Their lengths are in the scale of millimeters, and widths are typically less than 0.1 mm (Anders et al. 2014). Different with macroscale natural fractures and hydraulic fractures, these small-scale fractures do not contribute directly to global flow but only locally connected with global flow paths (Wu et al. 2004). They could potentially impact the flow process by increasing the connection between pore networks and macro-scale fractures (Wang and Reed 2009).

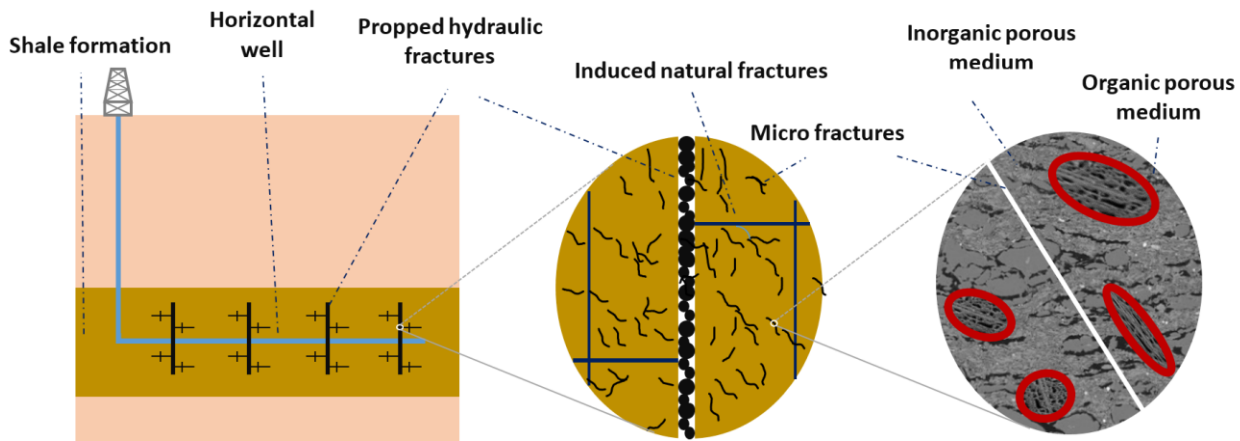


Figure 3-2 Multi-scale illustration of unconventional reservoirs: gas flow network includes hydraulic fracture, macro-scale natural fractures, micro-scale natural fractures, organic porous medium, and inorganic porous medium

The matrix in unconventional reservoirs is much tighter compared with that in conventional reservoirs. Many techniques (e.g. SEM, FE-SEM, MICP, and NMR) have been used to analyze pores in rocks from different shale plays (Loucks et al. 2012; Loucks et al. 2009; Nelson, 2009). They show that a combination of nanopore networks connected to micrometer pore networks controls the gas flow in shale, and the dominate pores are in the scale of nanometers. Nelson (2009) summarized the measurement work from different researchers about the width of pore and pore-throat in different siliciclastic rocks, along with the size of hydrocarbon molecules and the diameter of solid particles. For most shales, the pore throat sizes fall in the 10^{-2} and $10^{-1}\mu\text{m}$ range and slight discrepancies exist among them. This pore-throat size is almost the same as the size of asphaltene molecule, 50 times larger than the size of light oil molecular, and 100 times greater than the size of methane molecule. The sandstones are typically 3 or 4 orders of magnitude larger than the shales on the pore throat size.

The presence of organic porosity is another distinctive feature of shale gas reservoirs from conventional reservoirs. Most shale gas reservoirs are self-sourced rocks containing a significant amount of organic matters, and the total organic carbon (TOC) is highly variable among different shales (X. Gu et al. 2016). Organic pores with a high degree of connectivity are reported to exist in most of these plays in addition to inorganic pores (Curtis et al., 2012; Wang and Reed, 2009). Depending on the content of TOC, these organic matters may be sparsely scattered in the inorganic matrix or may be joined to form an organic matter production fairway, and shale can show a dominance of one pore system or a combination of both. As a result, gas flow through these two porous media is predominantly either in series or parallel (Loucks et al. 2009, 2012). Organic pores are typically one or two orders of magnitude smaller than those of inorganic pores (Wang et al. 2014; Yang et al. 2016), and thus the flow conductivity (permeability in reservoir simulation) for organic porous media is smaller. In addition, due to the difference in host materials, fluid-solid interactions for flow in this porous media also vary considerably. Organic pores are strongly oil-wet, while inorganic pores are water-wet (M. Xu and Dehghanpour 2014).

3.2 Various Fluid Flow Physics

Because of the highly heterogeneous and hierarchical geological features, traditional understandings of gas flow and storage mechanism in conventional reservoirs have limitations for their direct applications in shale gas reservoirs. Gas flow in unconventional-reservoir porous and fractured media is subject to a more nonlinear flow process, which includes but not limited to: gas slippage effect, gas adsorption/desorption, and non-Darcy flow at high flow rate. In addition, these non-linear flow mechanisms do not occur in all geological constituents, but only in specific ones. Conceptually we can divide the gas movement into a four-stage process: (1) high-rate non-Darcy flow in hydraulic fractures; (2) Darcy flow in natural fractures and sufficiently large pores; (3) slippage flow in extremely small pores; and (4) gas desorption off the internal organic matter surfaces. This part explains the physics behind these nonlinear flow processes and briefly analyzes them in a quantitative approach.

3.2.1 Gas Slippage Effect

The slippage effect is significant for gas flow in extremely small-size porous medium, and this can be explained by fluid flow mechanism in microscale. In microfluidics, Knudsen

number (K_n) is used to measure the deviation of the fluid-flow state from the continuum flow. Four fluid flow regimes can be distinguished based on this number, which includes continuum flow ($Kn < 0.01$), slip flow ($0.01 < Kn < 0.1$), transition region flow ($0.1 < Kn < 10$) and molecular flow ($10 < Kn$) (Javadpour et al. 2007). With reasonable estimations of the pore radius in unconventional reservoirs, pore radius in conventional reservoirs, and fracture widths in unconventional reservoirs, gas flow regimes in these media can be quantified. Details of this analysis are discussed in Section 3.1.1.1. As demonstrated in Figure 3-3, slip flow occurs in most unconventional reservoir pores and some conventional reservoir pores. On contrast, gas flow in unconventional reservoir fractures is subject only to continuum flow. The continuum flow from this microfluidics analysis can be described using the standard Navier-Stokes governing equations with a “no-slip” wall conditions on the macroscopic scale (Roy et al. 2003). This equation leads to Darcy’s law with a constant permeability in the Poiseuille’s flow in a capillary (Soulaine, 2016). For a complicated porous medium, this permeability is still a constant by accounting the aggregate complexities in cross-section area and connectedness of the reservoir pores (Wang et al. 2007). As a comparison, the macroscale governing equations for the slip flow is the Navier-Stokes governing equation with a slip-wall condition. The apparent permeability (gas permeability) considering gas slippage in a porous medium is not constant anymore. It depends on the pressure and is higher compared to the intrinsic permeability (Chen et al. 2015).

Many first-order and second-order approximations are proposed to describe gas flow in these micro- and nanoflow channels (Klinkenberg and 1941; Civan et al. 2010; Zhang et al. 2012; Chen et al. 2015). In this study, we used the gas permeability correlation by Civan et al. (Civan et al. 2010) which incorporates the suite of continuum, slip, transition, and Knudsen flow regimes in one equation:

$$k_a = k_{in} \left(1 + cK_n\right) \left(1 + \frac{4K_n}{1 - bK_n}\right) \quad (3.1)$$

where k_a is the apparent gas permeability; k_{in} is the rock intrinsic permeability; c is the dimensionless rarefaction coefficient and the slip coefficient b is an empirical parameter. Its value can be determined by the linearized Boltzmann equation.

3.2.1.1 Estimations of Gas Flow Regimes in Unconventional Reservoir Pores, Unconventional Reservoir Fractures and Conventional Reservoir Pores

Knudsen number is defined as the ratio of mean free path to the characteristic length,

$$Kn = \frac{\bar{\lambda}}{d} \quad (3.2)$$

The characteristic length of the fluid flow medium is radius for pores and width for fractures. The mean free path is the average particle-travelling distance between collisions. For collisions of identical particles, the following applies for the mean free path

$$\bar{\lambda} = \frac{RT}{\sqrt{2\pi PN_a d_m^2}} \quad (3.3)$$

where R is the gas constant, T is temperature, P is the pressure, N_a is the Avogadro's number and d_m is the nominal molecular diameter.

Here we introduce the gas molecule density n and the gas molecule density at the reference state n_0 . Pressure and temperature at this reference state are 1atm and 273 K respectively.

$$n = \frac{P}{RT} \quad (3.4)$$

Substitute Eq. (3.3) and Eq. (3.4) into Equation (3.2), a linear relationship can be obtained between the logarithm of the characteristic length and the logarithm of the relative gas molecule density given a constant Knudsen number.

$$\log(d) = -\log\left(\frac{n}{n_0}\right) + \log\left(\frac{R}{\sqrt{2\pi N_a d_m^2}} \frac{T_0}{P_0}\right) - \log(Kn) \quad (3.5)$$

By plotting three curves with Knudsen number of 10.0, 0.1, and 0.01 in the $\log(d)$ vs. $\log\left(\frac{n}{n_0}\right)$ figure, the whole domain can be divided into four gas flow regimes: continuum flow, slip flow, transitional flow, and free molecular flow.

Pressure and temperature ranges for conventional and unconventional reservoirs are estimated based on the typical pressure gradient range (0.4 psi/ft – 0.8 psi/ft), reservoir depth range (500 ft – 15000ft for conventional reservoirs and 5000 ft – 10000ft for unconventional reservoirs), and geothermal gradient (1F/70ft). Fracture widths are estimated to be in the range between 10 μm and 600 μm (Huy et al. 2010; Liang et al. 2016). The estimation of pore size range for unconventional reservoirs and conventional reservoirs are 5nm-60nm and 0.5 μm -10 μm , respectively (L. Chen et al. 2015; Nelson 2009). Table 3-1 lists details of this estimation. With these ranges, we can calculate the area of gas flow regimes for conventional reservoir pores, unconventional reservoir pores, and unconventional reservoir fractures. Results of the calculated area are plotted in Figure 3-3.

Table 3-1 Estimations of key parameters to determine gas flow regimes in unconventional reservoir fractures, unconventional pores, and conventional reservoir pores

Parameters (unit)	Values
Pore radius for unconventional reservoirs (μm)	0.01-0.06
Pore radius for conventional reservoirs (μm)	0.5-10
Fracture width for conventional and unconventional reservoirs (μm)	10-600
Temperature for conventional reservoirs (F)	75-280
Pressure in conventional reservoirs (psi)	200-12000
Temperature for unconventional reservoirs (F)	140-210
Pressure in unconventional reservoirs (psi)	2000 - 8000

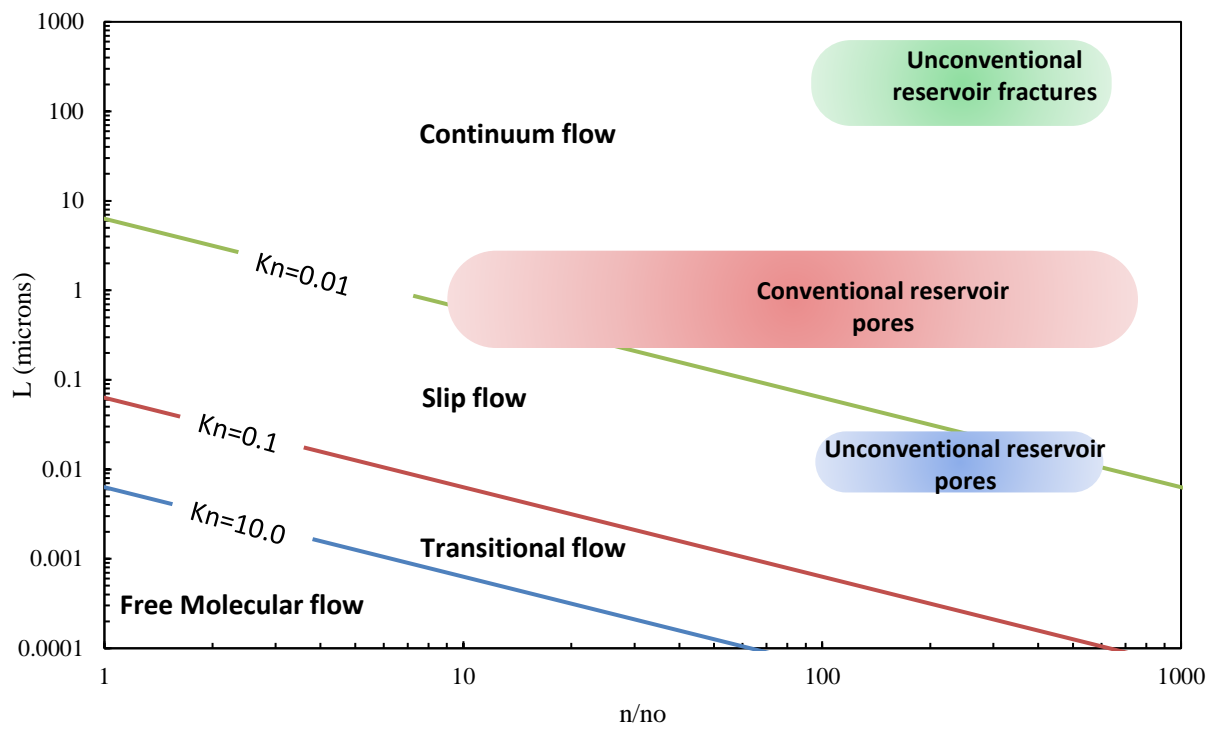


Figure 3-3 Quantification of gas flow regimes in unconventional reservoir fractures, conventional reservoir pores, and unconventional reservoir pores based on microfluidics theory

3.2.2 Gas Adsorption and Desorption

Organic matters in shale have a much higher adsorption capacity compared with the inorganic matter because of its physical and chemical properties. Gases tends to adsorb on the surface of organic pores, as indicated by the experimental data that the total amount of adsorbed gas has a strong linear correlation with the organic matter content (Zhang et al. 2012). This adsorption phenomenon provides another mechanism of gas storage in addition to free compressed gas and dissolved gas. Because the time of the desorption process is negligible compared to that of the diffusion and flow process, adsorbed gas can always be regarded in static equilibrium with the free gas (Crosdale et al. 1998). The Langmuir's isotherm (Langmuir 1918) is used to describe this static equilibrium. The gas content, VE , typically measured as cubic feet of gas per ton of net shale (EIA, 2011; Mengal and Wattenbarger, 2011) can be expressed as,

$$V_E = V_L \frac{P}{P + P_L} \quad (3.6)$$

where VE is the gas content or Langmuir's volume in scf/ton (or standard volume adsorbed per unit rock mass); P is reservoir gas pressure; and PL is Langmuir's pressure, the pressure at which 50% of the gas is desorbed. In general, Langmuir's volume, VL, is a function of the organic richness (or TOC) and thermal maturity of the shale.

3.2.3 Non-Darcy Flow

Unconventional reservoir dynamics is characterized by highly nonlinear behavior of multiphase flow in extremely low-permeability rock, coupled by many co-existing physical processes, e.g., non-Darcy flow. Blasingame (2008) and Moridis et al. (2010) provide comprehensive review of flow mechanisms in unconventional shale gas reservoirs. Both studies point out that non-laminar/non-Darcy flow concept of high-velocity may turn out to be important in shale gas production. The non-laminar/non-Darcy flow concept of high-velocity flow of gas flow in shale gas reservoirs may not be represented by Darcy's law and the Forchheimer equation is probably sufficient for many applications.

3.3 Model Conceptualization

An idealized physical model is built to incorporate various geological and flow-mechanism characteristics as discussed above. All available characterization data about hydraulic fractures, macro-scale natural fractures, micro-scale natural fractures, organic matter, and inorganic matter porous medium can be incorporated in this model.

Conceptually we divide the complex and hierarchical rock structures (Figure 3-4.a) into several continua, and each continuum represents either a porous medium or a fractured medium, as shown in Figure 3-4.b. The thermodynamic equilibrium does not always exist between different media which are even close to each other, and therefore the key fluid-flow and thermodynamic properties (pressure, temperature, and concentration) vary (Wang 2013; Wu et al. 2014). Catching all geological details (e.g. size, direction, shape) for the numerical study of the whole reservoir is computationally impossible. For reservoir-scale engineering studies, we instead assume each of these porous or fractured media homogeneous, and only capture its key fluid flow characteristics as demonstrated in Figure 3-4.c. This idea follows the classical double porosity model to study natural fractured reservoirs by Warren and Root (Warren and Root 1963). This approach is practical and able to capture the key flow characteristics, which include

volume fraction of each constituents, fracture spacing, organic matter size, and total organic matter content. In this homogenized model, macroscale natural fractures are assumed to be continuous and are idealized to be orthogonal 3D planes which are parallel to the principal axis of permeability; microscale natural fractures are regarded as discontinuous planes intersected with macroscale natural fractures. Organic matters are represented by spheres embedded in the inorganic matter.

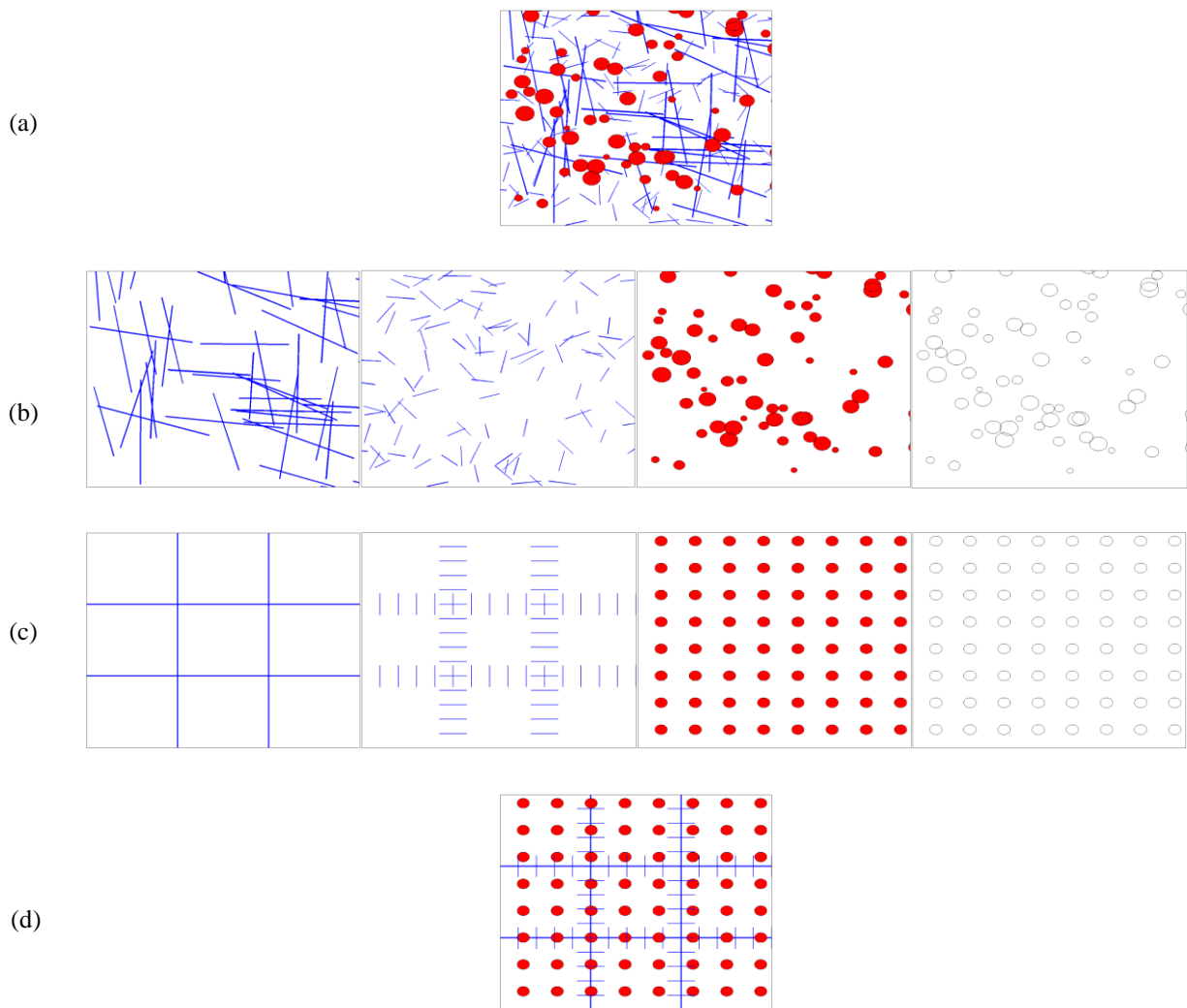


Figure 3-4. (a) General fracture network, organic and inorganic matter in shale rocks based on statistical distributions of fracture and porous medium properties, conceptualized from SEM image. (b) The disintegration of the complicated and hierarchical shale rock structure into multiple components (from left to right: natural fractures, micro fractures, organic matter, and inorganic matter). (c) Idealization of each component using the average approach by capturing the key flow characteristics. (d) Recombination of the idealized components for numerical simulation

We further assume fluid flow in the global domain is dominated by the connection of macro-scale fractures. Locally these macro-scale fractures connect to micro-scale fractures and inorganic matters. Gas stored in organic matter transports to production wells through inorganic matter, micro-scale fractures and intermediate-scale fractures sequentially. The schematic of the multi-porosity conceptualization for handling multi-component nature and multi-scale behaviors of shale rocks is demonstrated in Figure 3-5. In the next section, we will explain how this conceptualized model is built within our numerical framework. The key challenge is to generate a mesh system that can capture key characteristics of this multi-porosity system.

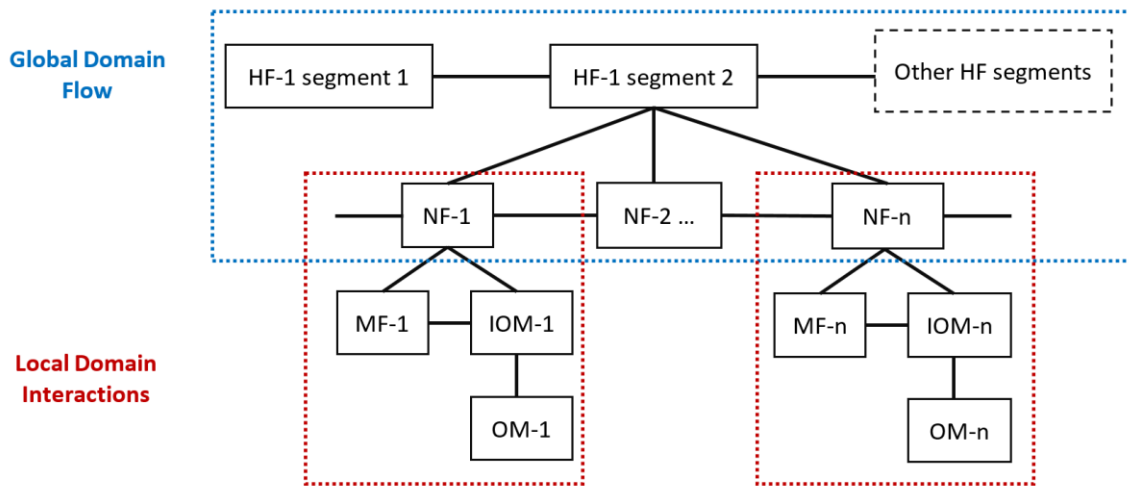


Figure 3-5 Conceptualization of global domain flow and local domain interactions among different geological constituents

3.4 Mathematics and Numerical Method

We adopted a numerical framework into which the multi-porosity, the multi-physics model can be implemented (Pruess et al. 1999; Pruess 2004; Wu and Pruess 1998; Xiong et al. 2015). Versatility and scalability are two important features of this framework. This framework has been successfully applied for large-scale numerical simulation of nuclear waste disposal, environmental remediation problems, energy production from geothermal, oil and gas reservoirs, geological carbon sequestration, etc. In this section, we will briefly discuss several key features for this function. This mathematical model starts from the integral form of mass conservation equations rather than the partial differential form.

$$\frac{d}{dt} \int_{V_n} M_\beta dV_n = \int_{\Gamma_n} F_\beta \cdot n d\Gamma_n + \int_{V_n} q_\beta dV_n \quad (3.7)$$

where V_n is an arbitrary subdomain for integration bounded by the close surface Γ_n . The quantity M , F , and q denote the accumulation term (mass per volume), mass flux term, and sink/source term respectively. n is a normal vector on surface pointing inward into the element. β labels the fluid phase.

In the mass flux term, F_β can be extended by Darcy's law for multiphase flow:

$$F_\beta = \nabla \cdot \left(\rho_\beta \frac{k k_{r\beta}}{\mu_\beta} \nabla \psi_\beta \right) \quad (3.8)$$

where ρ_β is the density of phase β ; μ_β is the phase viscosity; k and $k_{r\beta}$ are the intrinsic permeability of the porous medium and relative permeability of the β phase, respectively; ψ_β is the β phase flow potential.

The governing integral equations for continuity are handled using the integral finite difference numerical method for spatial discretization and the time domain is discretized using the first order difference, which gives the discretized form of the flux term

$$\int_{\Gamma_n} F_\beta \cdot n d\Gamma_n = \sum_{j \in \eta_i} \left(\bar{\rho}_\beta \lambda_\beta \right)_{ij+1/2}^{n+1} \gamma_{ij} \left[\psi_{\beta j}^{n+1} - \psi_{\beta j}^n \right] \quad (3.9)$$

where η_i contains the set of neighbor elements (j) or nodes of element i to which element i is directly connected; λ_β is the mobility of phase β :

$$\lambda_\beta = \frac{k_{r\beta}}{\mu_\beta} \quad (3.10)$$

and the transmissivity of flow terms is defined as

$$\gamma_{ij} = \frac{A_{ij} k_{ij+1/2}}{d_i + d_j} \quad (3.11)$$

In Eq. (3.11), A_{ij} is the common interface area between connected elements i and j ; d_i and d_j are distances from the center of element i and j to the interface between elements i and j ;

As seen in Eq. (3.9), the integral finite difference approach avoids references to the global coordinates, requiring only local connection information. So it can easily deal with regular and irregular grids. And through this approach the double- or multi-porosity models can be implemented into reservoir simulation in the pre-processing section. Numerically, these double- or multi-porosity models are characterized by several overlaid computational grid layers. In practice, each primary grid is extended to multiple grids, which share the same location in the physical domain. Unlike the local grid refinement method (Yan et al. 2016), the connection information among these generated multi-grids is obtained via the analytical solution for fluid flow in pseudo-steady state. These grids can be inter-connected within one continuum or intra-connected among different continuum according to model assumptions.

3.4.1 Key Parameters for Fluid Flow among Various Continua

The key to handle double- or multi-porosity models is obtaining the average interface area and distances between different continuum. In this study, they are connections between:

- 1) Macroscale natural fractures and microscale natural fractures;
- 2) Macroscale natural fractures and inorganic matrix;
- 3) Microscale natural fractures and inorganic matrix;
- 4) Inorganic matrix and organic matrix.

Wu et al. (2004) extended Warrant and Root's approach (Warren and Root 1963) and calculated characteristic distances for evaluating flow terms for the first three kinds of connections. In this study, parameters for the fourth connections are derived analytically. The organic matter is conceptualized to be a sphere embedded in the inorganic matrix. Fluid flow between the organic and inorganic matter is assumed to be in the pseudo-steady state. Details of this derivation can be referenced below. Table 3-2 summarizes the interface and characteristic distance for these four connections.

Table 3-2 The contact interface and characteristic distances for these four connections

3D	NF-IOM		MF-IOM		NF-MF		IOM-OM	
	NF	IOM	MF	IOM	NF	MF	IOM	OM
Characteristic Distance d_i, d_j	0	$\frac{l_f}{10}$	0	$\frac{l_f}{10}$	0	$\frac{l_f}{2}$	$r_o \left(-\frac{3}{2} \frac{(TOC)^{1/3} - TOC}{1 - TOC} + 1 \right)$	$\frac{r_o}{5}$
Contact Area A_{ij}	$\frac{6V_{block}}{L_f}$		$\frac{6V_{block}}{L_f}$		$\frac{\phi_{MF}\phi_{NF}V_{block}}{L_f}$		$\frac{3V_{block}}{r_o}$	

Note in Table 3-2, subscript NF represents macroscale fractures, MF, micro-scale fractures, OM, organic matter, respectively. L is the characteristic distance, l is the fracture spacing, r_o is the radius of organic matter, TOC is the total organic content.

3.4.2 Fluid Flow Parameters Between Organic and Inorganic Matter

This section derives the connection details between the embedded organic matter and inorganic matter using analytical solutions. The TOC volume and the average organic matter size are required as input in this approach. Its objective is to derive the contact area and the distance between inorganic matter and organic matter given the TOC (volume) and the average organic matter size.

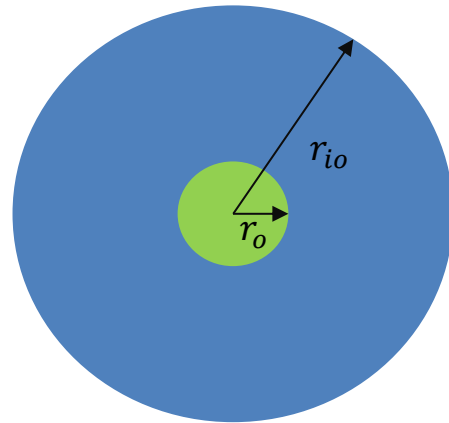


Figure 3-6 Conceptualization of fluid flow between organic and inorganic matter

In this derivation, the average size of organic matter (r_o) and the total organic content (TOC) in volume fraction are assumed to be given. Based on the definition of TOC in volume, the average radius of inorganic matter is:

$$r_{io} = \frac{r_o}{\sqrt[3]{TOC}} \quad (3.12)$$

The primary differential equation for 3D spherical transient flow of a single-phase slightly compressible fluid in porous media is:

$$\frac{1}{r^2} \frac{\partial}{\partial r} \left(r^2 \frac{\partial P}{\partial r} \right) = \frac{\phi c_t \mu}{k} \frac{\partial P}{\partial t} \quad (3.13)$$

In the organic matter, fluid flow is assumed to reach pseudo-steady state (same to the assumption in Warren-Root model). Thus, the rate of pressure drop at any location is the same:

$$\frac{\partial P}{\partial t} = C \quad (3.14)$$

Substituting Eq. (3.14) into Eq. (3.13), we have:

$$\frac{1}{r^2} \frac{\partial}{\partial r} \left(r^2 \frac{\partial P}{\partial r} \right) = B \quad (3.15)$$

where B is a constant and defined as

$$B = \frac{\phi c_t \mu}{k} C \quad (3.16)$$

The general solution for the partial differential equation (3.15) is:

$$P(r, t) = \frac{B}{6} r^2 - \frac{C_1}{r} + C_2 + C t \quad (3.17)$$

The partial derivative of P with respect to r is:

$$\frac{\partial P}{\partial r} = \frac{B}{3} r + \frac{C_1}{r^2} \quad (3.18)$$

For the flow regime, we have the inner boundary condition (center of the organic matter) and outer boundary condition (surface of the organic matter) as:

$$\left. \frac{\partial P}{\partial r} \right|_{r=0} = 0 \quad (3.19)$$

and

$$\left. \frac{\partial P}{\partial r} \right|_{r=r_o} = -\frac{q\mu}{Ak} \quad (3.20)$$

and

$$P(r = r_o, t) = P_{io} \quad (3.21)$$

where A is the area of the circular surface between organic and inorganic matter ($A = 4\pi r_o^2$).

Combining Eq. (3.18)– Eq. (3.21), we have:

$$B = -\frac{3q\mu}{Akr_e} \quad (3.22)$$

$$C_1 = 0 \quad (3.23)$$

And

$$C_2 + Ct = P_{io} - \frac{B}{6}r_o^2 \quad (3.24)$$

Substituting Eq. (3.22)- Eq. (3.24) into Eq. (3.17), we can have the pressure distribution inside the organic matter for the pseudo-steady state fluid flow:

$$P(r, t) = P_{io} + \frac{B}{6}(r^2 - r_e^2) \quad (3.25)$$

The average pressure inside the organic matter can be calculated using the following definition:

$$\overline{P_m} = \frac{\int_0^{r_o} P(r, t) 4\pi r^2 dr}{\frac{4\pi}{3} r_o^3} \quad (3.26)$$

Thus, we can have:

$$q = -\frac{k}{\mu} \frac{A}{r_o/5} \left(P_{io} - \overline{P_m} \right) \quad (3.27)$$

Similar approaches can be used to derive the equivalent length for the inorganic matter.

With the semi-steady state assumption,

$$r^2 \frac{\partial P}{\partial r} = C_4 = \frac{q\mu}{4\pi k} \quad (3.28)$$

Let the dimensionless pressure be

$$P_D = -\frac{4\pi r_o^2 (P - P_o) k}{q \mu r_o} \quad (3.29)$$

And the dimensionless radius as

$$r_D = \frac{r}{r_o} \quad (3.30)$$

Substitute Eq. (3.29) and Eq. (3.30), we have

$$r_D^2 \frac{\partial P_D}{\partial r_D} = 1 \quad (3.31)$$

Solve the above partial differential equation and apply the boundary condition $P_D|_{r_D=1} = 0$,

we have

$$P_D = -\frac{1}{r_D} + 1 \quad (3.32)$$

The average dimensionless pressure for the inorganic matter is:

$$\bar{P}_D = \frac{\int_1^{r_{io}/r_o} 4\pi r_D^2 P_D dr_D}{\int_1^{r_{io}/r_o} 4\pi r_D^2 dr_D} = -\frac{3}{2} \frac{r_D^2 \Big|_{1}^{\frac{r_{io}}{r_o}}}{r_D^3 \Big|_1^{\frac{r_{io}}{r_o}}} + 1 = -\frac{3}{2} \frac{\left(\frac{r_{io}}{r_o}\right)^2 - 1}{\left(\frac{r_{io}}{r_o}\right)^3 - 1} + 1 \quad (3.33)$$

Based on Eq. (3.33)

$$-\frac{3}{2} \frac{\left(\frac{r_{io}}{r_o}\right)^2 - 1}{\left(\frac{r_{io}}{r_o}\right)^3 - 1} + 1 = -\frac{3}{2} \frac{\left(\frac{1}{TOC}\right)^{2/3} - 1}{\frac{1}{TOC} - 1} + 1 \quad (3.34)$$

Let

$$f(TOC) = -\frac{3}{2} \frac{\left(\frac{1}{TOC}\right)^{2/3} - 1}{\frac{1}{TOC} - 1} + 1 = -\frac{3}{2} \frac{(TOC)^{1/3} - TOC}{1 - TOC} + 1 \quad (3.35)$$

Substitute Eq. (3.34) and Eq. (3.35) into the definition of dimensionless pressure (3.29), we have

$$q = -\frac{k}{\mu} \frac{A}{r_o f(TOC)} (\bar{P} - P_o) \quad (3.36)$$

3.4.3 Governing Equations for Multiple Fluid Flow Physics

As mentioned above, gas flow and storage mechanism vary in different geological constituents. Correspondingly, equations about flow and accumulation terms have different forms for different continuum. For the accumulation term,

$$M_{\beta}^{\alpha} = \begin{cases} \phi S_{\beta} \rho_{\beta}, & \alpha = \text{IOM} \\ \phi S_{\beta} \rho_{\beta} + \rho_{\beta} V_L \frac{P}{P+P_L}, & \alpha = \text{OM} \\ \phi (\sigma_m) S_{\beta} \rho_{\beta}, & \alpha = \text{NF, MF, HF} \end{cases} \quad (3.37)$$

For the flow term,

$$F_{\beta}^{\alpha} = \begin{cases} -\rho_{\beta} k_{in} \left(1 + cK_n\right) \left(1 + \frac{4K_n}{1 - bK_n}\right) \frac{k_{r\beta,\alpha}}{\mu_{\beta}} (\nabla P_{\beta} - \rho_{\beta} g), & \alpha = \text{IOM, OM} \\ -\rho_{\beta} k_{in} \frac{k_{r\beta,\alpha}}{\mu_{\beta}} (\nabla P_{\beta} - \rho_{\beta} g), & \alpha = \text{NF, MF} \\ -\rho_{\beta} \left[\frac{\mu_{\beta}}{k_{in} k_{r\beta}} + \sqrt{\left(\frac{\mu_{\beta}}{k_{in} k_{r\beta}}\right)^2 - 4\gamma\rho_{\beta} (\nabla P_{\beta} - \rho_{\beta} g)} \right] / 2\gamma, & \alpha = \text{HF} \end{cases} \quad (3.38)$$

Different governing equations considering these physics, however, all follow the mass conservation law in general and thus can be handled uniformly under one numerical framework. Variables involved in the simulation are divided into two groups, primary variables and secondary variables. The simulator essentially solves mass conservation equations for primary variables as a function of time with the knowledge of initial conditions. At each time step, once the primary variables are obtained, secondary variables can be updated through the constitutive law. In solving these nonlinear equations, the Jacobian matrix are constructed using numerical methods. Eq. (3.39) demonstrates the Jacobian matrix structure for the case in Figure 3-5, in which the hydraulic fracture connects with two local units.

$$\begin{array}{c}
 \left[\begin{array}{ccc|c} \times & \times & & \times \\ \times & \times & \times & \times \\ & \times & \times & \times \\ & & \times & \times \\ & & & \times \\ \hline & & & \times \\ \times & \times & & \times & \times \\ & & \times & \times & \times \\ & & & \times & \times \\ & & & & \times \end{array} \right] \times \left[\begin{array}{c} \Delta P_{HF} \\ \Delta P_{1_nf} \\ \Delta P_{1_mf} \\ \Delta P_{1_im} \\ \Delta P_{1_om} \\ \Delta P_{2_nf} \\ \Delta P_{2_mf} \\ \Delta P_{2_im} \\ \Delta P_{2_om} \end{array} \right] = \left[\begin{array}{c} R_{HF} \\ R_{1_nf} \\ R_{1_mf} \\ R_{1_im} \\ R_{1_om} \\ R_{2_nf} \\ R_{2_mf} \\ R_{2_im} \\ R_{2_om} \end{array} \right]
 \end{array} \quad (3.39)$$

3.5 Model Applications

In this section, we applied the multi-porosity, multi-physics model to simulate fluid flow in a synthetic but realistic case. We also simulated two other cases based on the single-porosity model and the double-porosity model. The shale gas reservoir model is built considering one horizontal well and multiple hydraulic fractures. The reservoir thickness is 20m. Hydraulic fractures have a half-length of 250m and a uniform spacing of 40m. We assume all hydraulic fractures penetrates this formation vertically, and thus this 3D problem can be simplified into a 2D model. We further assume the reservoir is symmetric along the horizontal well as well as hydraulic fractures. In this way the model can be further simplified by simulating only one-quarter of the area between two adjacent hydraulic fractures. Figure 3-7 shows the schematic of this reservoir model, as described above. It also presents the mesh for this extracted area with the corresponding hydraulic fracture. All grid blocks are processed to have four overlaying porosities, as discussed in Section 3.3, which include natural fractures, micro fractures, organic matter and inorganic matter. The hydraulic fractures is simulated explicitly by a set of small-scale grid blocks with high-permeability and high-porosity. Physical properties for different geological features are summarized in Table 3-3.

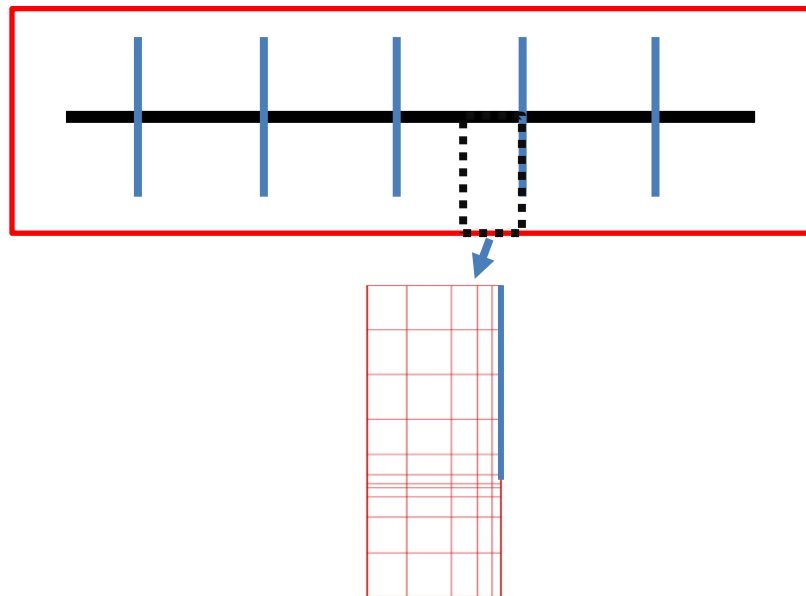


Figure 3-7 The reservoir model schematic and the mesh for simulation

Table 3-3 Physical properties for different geological features

Parameter	Value	Unit
Matrix porosity	$\phi_M = 0.1$	
Large-fracture porosity	$\phi_F = 0.001$	
Small-fracture porosity	$\phi_f = 0.01$	
Total organic volume	TOC = 0.2	
Large-fracture spacing	$l_F = 5$	m
Small-fracture spacing	$l_f = 0.5$	m
Large-fracture characteristics length	$L_F = 3.5$	m
Small-fracture characteristics length	$L_f = 0.1$	m
Organic matter characteristics length	$r_o = 0.01$	m
Large-fracture permeability	$k_F = 1.4 \times 10^{-13}$	m^2
Small-fracture permeability	$k_f = 1.4 \times 10^{-15}$	m^2
Inorganic matter matrix permeability	$k_{IM} = 1.4 \times 10^{-17}$	m^2
Organic matter matrix permeability	$k_{OM} = 1.4 \times 10^{-19}$	m^2
Inorganic matter Klinkenberg coefficient	$b = 8.6 \times 10^5$	Pa

Organic matter Klinkenberg coefficient	$b = 1.03 \times 10^6$	Pa
Adsorption parameter in organic matter	$V_L = 2.2 \times 10^{-3}$	m^2 / kg
Water production rate	$q = 20$	m^3/day
Total compressibility of four media	$C_F = C_f = C_{OM} = C_{IM} = 1.0 \times 10^{-9}$	$1/Pa$
Formation thickness	$h = 20$	m

This reservoir is produced with a constant BHP of 1.5×10^8 Pa for 10 years. The initial reservoir pressure is assumed to be at 2.0×10^8 Pa. Figure 3-8 compares the simulated gas production rates from these three models. It can be clearly seen that only the multiple-porosity model proposed in this study can capture behaviors for the whole life of production: a great initial peak, a sharp decline in the first few months, followed by a long flat production tail. The single-porosity model or the double-porosity model could only capture early-time behaviors, i.e., an initial production peak followed by a sharp decline. Their simulated production rate drops to zero after four years and six years, respectively.

The behavior of a long flat tail in the late-time can be explained through our proposed multi-porosity, multi-physics model. It is due to the gas desorption in organic pores. In our model assumptions, adsorption/desorption processes primarily occur in organic matters, and this organic matter does not connect with the natural fractures. As a result, pressure drops inside organic matters in the early time are insignificant (Figure 3-9), and contributions from gases stored in organic matters is little. Considerable amounts of gases in organic matters begin to desorb and flow only when a certain pressure difference exists between the organic matter and inorganic matter, which occurs in the late time. Gases from this source contributes major parts to the total production in this period, but in a relatively slow and steady way.

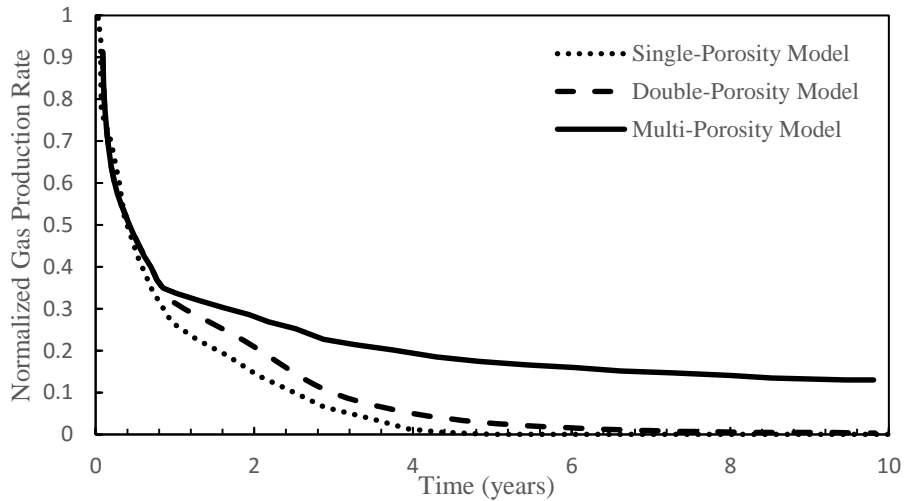


Figure 3-8 Comparisons of the normalized gas production rate for these three models

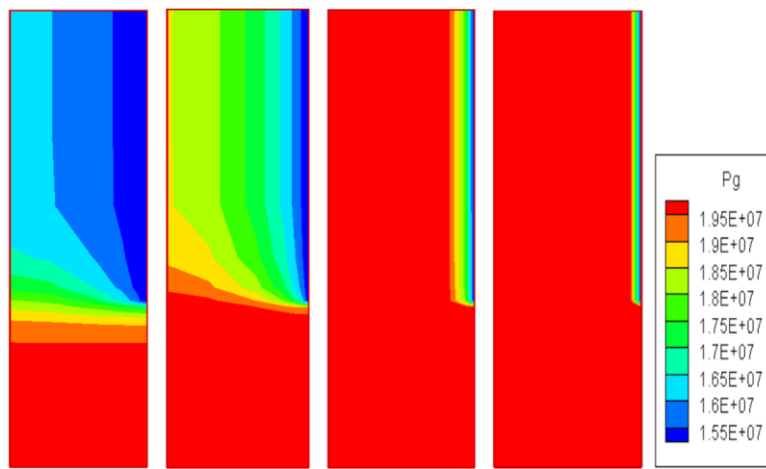


Figure 3-9 Simulated pressure contours after one-year production for four continua in the multi-porosity and multi-physics model

3.6 Summary

In this chapter, we present a multi-domain, multi-physics model, aiming to more realistically simulate the fluid flow in shale gas reservoirs. The complicated and hierarchical shale rock structures are decomposed into five geological constituents: organic nanopores, inorganic nanopores, local micro-fractures, global natural fractures, and hydraulic fractures. Fluid flow governing equations in this model vary according to the different dominant fluid flow mechanism in different regions. We introduced a general numerical framework into which this model can be implemented. We also discussed how to evaluate key parameters this numerical

model. Model applications with practical interests are given. One synthetic, but realistic, test cases is simulated. Our results demonstrate that this model can capture typical production behaviors of unconventional reservoirs that traditional numerical approaches cannot: a great initial peak, the sharp decline in the first few months, followed by a long flat production tail.

CHAPTER 4

COUPLED NUMERICAL APPROACH COMBINING X-FEM AND EDFM FOR THE FLUID-DRIVEN FRACTURE PROPAGATION PROCESS IN POROUS MEDIA

In this chapter, a coupled simulation strategy combining the embedded discrete fracture method (EDFM) and the extended finite element method (X-FEM) is developed to simulate the fluid driven fracture propagation process in porous media. This physical process includes three strong coupling mechanics: fluid flow in fractures and porous media, solid deformation with fractures, and fracture propagations. The EDFM and X-FEM are used to simulate fracture-related fluid mechanics and solid mechanics, respectively, with information exchanged under the iterative numerical coupling scheme. Mathematical equations on how to link these independent modules as well as numerical techniques on how to accelerate the coupling convergence rate are discussed in detail.

Both X-FEM and EDFM avoid the cumbersome construction of unstructured grids to capture fracture paths and also avoid the remeshing for the fracture growth. They are first validated via benchmark problems individually and then are coupled to simulate fracture propagation problems in two dimensions and in three dimensions. Simulated multi-physics fields meet understandings qualitatively, and simulated fracture parameters (length, width and net pressure) match with analytical solutions quantitatively.

4.1 Introduction

The fluid-driven fracture propagation in porous media is a fundamental process to many applications in petroleum engineering, such as hydraulic fracturing, produced water reinjection, borehole integrity, and drill cuttings reinjection. Quantitative evaluations of relevant fracture parameters are essential for the design analysis of these engineering. However, modeling such a process is not an easy task because at least three strong coupling mechanics (Figure 4-1) need to be accounted for: 1) fluid flow in fractures and porous media, 2) solid deformation, and 3) fracture propagations (Shlyapobersky 1985). These three mechanics have entirely different natures and are governed by equations with different forms.

The pioneering contributors tried solving these coupled non-linear integral-differential equations by an analytical approach. Several classic fracturing models (PKN, KGD and Penny-shaped fracture model) were developed (Zheltonov 1955; Perkins and Kern 1961; Geertsma and De Klerk 1969; Detournay 1999; Savitski and Detournay 2002). With some strong assumptions of simple geometry, these analytical solutions can capture the critical physics in this process, which contributes significantly to understanding the mechanism and physical effects of parameters in these equations. However, these analytical solutions have limitations to solving complex fracture problems, both physically and geometrically.

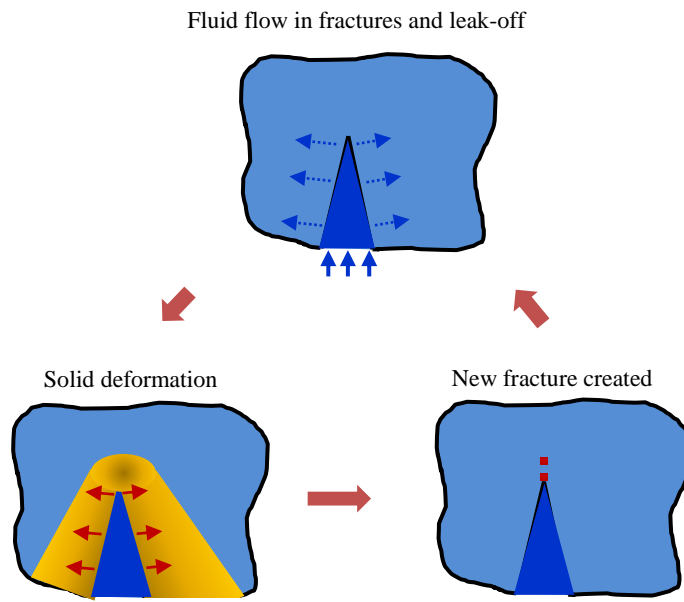


Figure 4-1 Three strong coupling processes during the fluid-driven fracture propagations in porous media

Later on, some pseudo-3D numerical tools were developed to simulate complex geometry problems with various finite element-based methods (Clifton and Abou-Sayed 1981; H. Gu and Yew 1988; G. Xu and Ortiz 1993). These tools were able to give more realistic estimates of fracture geometry/dimensions and thus achieved great success for conventional reservoirs. However, in the majority of available models, flow and solid deformation governing equations are oversimplified for the unconventional reservoirs. Fluid flow and rock deformation equations for 3D reservoirs are transferred into semi-analytical solutions for 2D fractures. The rock elastic behaviors in these numerical models are described by a singular integral equation relating the

fracture opening to the traction (Bui 1977). This equation was derived by assuming a planar fracture in an infinite homogeneous three-dimensional elastic body, which has limited applications for layered strata characterized by different mechanical properties and/or in-situ stresses.

$$\frac{G}{4\pi(1-v)} \int_{\Omega} \left[\frac{\partial}{\partial x} \left(\frac{1}{r} \right) \frac{\partial w}{\partial x} + \frac{\partial}{\partial y} \left(\frac{1}{r} \right) \frac{\partial w}{\partial y} \right] dx dy = T(x, y) \quad (4.1)$$

where $r = \left[(x - x')^2 + (y - y')^2 \right]^{1/2}$, and $T(x, y)$ is the normal traction on the fracture surface at local (x, y) , w is the fracture width; G is the shear modulus; v is Poisson's ratio of the material, and Ω is the fracture surface.

Fluid leakoff rate through fracture surfaces into the porous media in these numerical tools is quantified by (Howard and Fast 1957)

$$q_l = \frac{2c_1}{\sqrt{t - \tau(x, y)}} \quad (4.2)$$

where constant c_1 is an empirical fluid leak-off coefficient, and $\tau(x, y)$ is the time at which the fluid leak-off begins at location (x, y) on the fracture surface. This leak-off equation is derived by assuming a steady-state one-dimensional fluid flow, which has limitations for unconventional reservoirs with two following considerations. First, the transient-state flow may last long when the permeability is extremely low. And second, the pressure interferences from nearby fractures is inevitable for complex fracture networks.

The finite element method (FEM) (Chan et al. 1970; Bathe 2006; Smith et al. 2013; Salimzadeh et al. 2017) and the discrete fracture method (DFM) based on the finite volume method (FVM) (Kim and Deo 2000; Karimi-Fard et al. 2004) provide a more general solution for handling fracture-related solid- and fluid-mechanics, respectively. These two numerical methods start from most fundamental equations governing the physics of fluid flow (the continuity equation) and solid deformation (the stress equilibrium equation) and thus avoid the above-mentioned over simplifications. In these two methods, fractures are represented by one or one set of small-size grids which conform to the fracture paths. Fluid and solid mechanics behaviors are

captured by assigning these grids with fracture-related properties. However, developing these numerical models is challenging with following considerations. First, the mesh needs to be built in a way that the grid edges/faces coincide with all fracture surfaces, which requires the deployment of unstructured grids. Constructing such meshes is cumbersome especially for three-dimensional problems; second, in the finite element method, quadratic shape functions instead of linear shape functions are needed for the fracture tip grids to approximate the stress tip singularity; and third, remeshing is required at each time step for the fracture growth simulation.

The embedded discrete fracture method (EDFM) (Lee et al. 2001; Li and Lee 2008; Moinfar et al. 2014b; Wang et al. 2017) and the extended finite element method (X-FEM) (Moës et al. 1999; Sukumar et al. 2000) are two modeling techniques which extend the FEM and the DFM, respectively. In the EDFM, fractures are conceptualized to be virtually embedded into nearby matrix grid blocks by treating the fractures as single or several additional computational volume elements. In the X-FEM, the near fracture area is enriched by two additional groups of virtual nodes to incorporate both discontinuous fields and the near-tip asymptotic fields. Both methods (EDFM and X-FEM) allow for fracture simulations with structured grids, because the vital input features related to fractures in these two algorithms can be obtained directly via the geometrical calculation. Therefore, the three shortcomings regarding the FEM and DFM as discussed above can be alleviated.

A few recent efforts have been reported towards simulating the fracture propagation process based on the X-FEM. Lecampion investigated how to consider the presence of an internal pressure inside the fracture (Lecampion 2009). Chen discussed the implication of the X-FEM into ABAQUS via a new type of finite element (Chen 2013). Shi et al. developed an algorithm to couple the X-FEM based hydraulic fracturing simulations with proppant transport (Shi et al. 2016). Youn applied the X-FEM for randomized rock formations and performed a risk analysis (Youn 2016). However, to the best of our knowledge, there have been no studies on simulations of the solid deformation and fluid flow for both fractures and the porous media. In addition, no publications mentioned above discussed their applications for 3D problems.

The objective of the present research is to construct a coupled numerical approach combining X-FEM and EDFM to simulate both 2D and 3D fluid-driven fracture propagation

processes in the porous media. This study will also demonstrate the effectiveness of the simulation technique in predicting the complex processes. This paper is arranged as follows. Governing equations, numerical discretization approaches as well as the EDFM and X-FEM principles are briefly introduced in Section 4.2. In Section 4.3, key techniques to couple these independent modules are described. In Section 4.4, several typical problems are simulated to validate the accuracy of our developed EDFM and X-FEM models. In Section 4.5, the coupled simulation is performed for both 2D and 3D fracture propagation problems. The matching of our numerical solutions with benchmark analytical solutions indicates this method produces correct results.

4.2 Governing Equations and Numerical Formulations

Simulations in this study aims to understand the coupling between fluid flow and solid deformation during fluid-driven fracture propagations in porous media. These two physical processes have entirely different natures and behaviors, and thus they are characterized by different governing equations. Correspondingly, two different numerical schemes are adopted to solve these two sets of equations. The finite volume method (also known as the integral finite difference method) is preferred for discretizing fluid flow PDEs because it captures local conservations naturally, while the finite element method is adopted for solid mechanics because it is intuitive for the displacement compatibility.

The process of the single-phase fluid flow in porous and fractured media is governed by the mass conservation equation along with Darcy's law:

$$\frac{\partial}{\partial t}(\rho\phi) + \operatorname{div}(\rho\mathbf{v}) = q \quad (4.3)$$

where ρ is the fluid density; ϕ represents the porosity; \mathbf{v} is the Darcy velocity, and q is the sink/source per unit volume per unit time.

The Darcy velocity is calculated via Darcy's law:

$$\mathbf{v} = -\frac{k}{\mu}(\nabla p + \rho g) \quad (4.4)$$

where p is the fluid pressure; \mathbf{k} is the permeability tensor; μ is the fluid viscosity; \mathbf{g} denotes the acceleration due to gravity;

The discrete nonlinear equations at node i are as follows (Wu 1998; Pruess et al. 1999):

$$\frac{1}{\Delta t} \left[(\phi p V)_i^{n+1} - (\phi p V)_i^n \right] = \sum_{j \in \eta_i} \left(\frac{\rho}{\mu} \right)_{ij+1/2}^{n+1} \gamma_{ij} (\psi_j^{n+1} - \psi_i^{n+1}) + Q_i^{n+1} \quad (4.5)$$

where the superscript n and $n+1$ denote the previous time level and the current time level, respectively; V_i is the volume of element i ; Δt is the time step size; η_i contains the set of neighboring elements (j) connecting to element i ; subscript $ij+1/2$ denotes a proper averaging of properties at the interface between elements i and j ; Q_i^{n+1} is the mass sink/source term at element i . γ_{ij} is the defined transmissivity of flow terms.

$$\gamma_{ij} = \frac{A_{ij} k_{ij+1/2}}{d_i + d_j} \quad (4.6)$$

where A_{ij} is the common interface area between two elements; d_i and d_j are distances from the element center (i and j) to the common interface. $k_{ij+1/2}$ is an averaged absolute permeability along this direction. The flow potential in Eq. (4.5) is

$$\psi_i^{n+1} = P_i^{n+1} - \rho g D_i \quad (4.7)$$

where D_i is the depth of the center of element i ;

For the process of solid deformation, the governing equation is the linearized momentum balance equation by assuming the quasi-static equilibrium condition:

$$\mathbf{D}^T \boldsymbol{\sigma} = 0 \quad (4.8)$$

where $\boldsymbol{\sigma}$ denotes the stress vector, and \mathbf{D}^T is the transpose of the symmetric gradient operator. For a 2D case

$$\mathbf{D}^T = \begin{bmatrix} \partial/\partial x & & \partial/\partial y \\ 0 & \partial/\partial y & \partial/\partial x \end{bmatrix} \quad (4.9)$$

The stress field is connected with the strain field via the constitutive equations in linear elasticity

$$\boldsymbol{\sigma} = \mathbf{C}\boldsymbol{\epsilon} \quad (4.10)$$

where $\boldsymbol{\epsilon}$ is the strain vector; \mathbf{C} denotes the 3×3 stiffness matrix for 2D isotropic linear materials:

$$\mathbf{C} = \frac{E}{1-v^2} \begin{bmatrix} 1 & v & 0 \\ v & 1 & 0 \\ 0 & 0 & (1-v)/2 \end{bmatrix} \quad (4.11)$$

where E is Young's modulus; and v is Poisson's ratio.

The weak form of the stress equilibrium equation provides us with the principle of virtual displacements:

$$\int_V \bar{\boldsymbol{\epsilon}}^T \boldsymbol{\sigma} dV = \int_{\Gamma_t} \bar{\mathbf{U}}^t{}^T \mathbf{f}^t d\Gamma_t + \int_{\Gamma_c} \bar{\mathbf{U}}^c{}^T \mathbf{f}^c d\Gamma_c \quad (4.12)$$

where $\bar{\boldsymbol{\epsilon}}$, $\bar{\mathbf{U}}^t$ and $\bar{\mathbf{U}}^c$ are the virtual strain, virtual external boundary displacements, and virtual internal displacements at specific concentrated points, respectively; \mathbf{f}^t and \mathbf{f}^c are forces on boundaries; Γ_t and Γ_c are outer and internal boundaries for this object;

Rewrite Eq. (4.12) as a sum of integrations over all elements and substitute the strain-displacement, strain-stress relations into the equation, we have (Bathe 2006; Smith, Griffiths, and Margetts 2013)

$$\left[\sum_m \int_{V^{(m)}} \mathbf{B}^{(m)T} \mathbf{C}^{(m)} \mathbf{B}^{(m)} dV^{(m)} \right] \mathbf{U} = \sum_m \int_{\Gamma_c^{(m)}} \mathbf{h}^{c(m)T} \mathbf{f}^{c(m)} d\Gamma_c^{(m)} + \sum_m \int_{\Gamma_t^{(m)}} \mathbf{h}^{t(m)T} \mathbf{f}^{t(m)} d\Gamma_t^{(m)} \quad (4.13)$$

where $\mathbf{B}^{(m)}$ is the strain-displacement matrix for the element m , $\mathbf{C}^{(m)}$ is the stiffness matrix as defined in Eq. (4.11), and $\mathbf{h}^{(m)}$ is the displacement interpolation matrix.

Eq. (4.13) is a set of linear equations with the node displacement vector \mathbf{U} to be solved. It can be rewritten in the following form for the convention:

$$\mathbf{K}\mathbf{U} = \mathbf{R} \quad (4.14)$$

where

$$\mathbf{K} = \sum_m \int_{V^{(m)}} \mathbf{B}^{(m)T} \mathbf{C}^{(m)} \mathbf{B}^{(m)} dV^{(m)} \quad (4.15)$$

$$\mathbf{R} = \sum_m \int_{\Gamma_c^{(m)}} \mathbf{h}^{c(m)T} \mathbf{f}^{c(m)} d\Gamma_c^{(m)} + \sum_m \int_{\Gamma_t^{(m)}} \mathbf{h}^{t(m)T} \mathbf{f}^{t(m)} d\Gamma_t^{(m)} \quad (4.16)$$

In Eq. (4.14), \mathbf{K} is the global stiffness matrix; \mathbf{R} is the residual vector related boundary conditions.

The embedded discrete fracture method (EDFM) and the extended finite element method (X-FEM) are two modeling techniques based on the finite volume method and the finite element method, respectively, for the fracture-related mechanical analysis. Both methods allow for the simulation related to fractures with structured grids. Thus, considerable flexibility is achieved by avoiding the construction of unstructured grids which is quite challenging for complex three-dimensional fractures.

In the EDFM, fractures are conceptualized to be virtually embedded into nearby matrix grid blocks by treating them as a single or as several additional computational volume elements (Lee et al. 2001; Li and Lee 2008; Moinfar et al. 2014). The fracture thickness is only considered in the computational domain for fracture volume calculations, but not represented in the grid domain, because fracture thickness is several orders of magnitude smaller than the grid size. These fracture volume elements connect to nearby matrix elements as well as connecting to adjacent fracture elements. Such connection information can be directly obtained through geometric processes, which calculate two critical parameters: the fracture-matrix contacting area and the average distance, as required in Eq. In our previous work, we described a general

geometrical calculation algorithm for complicated 3D fractures, proved this approach is accurate to handle steady and pseudo-steady state flow and validated the EDFM approach by several numerical experiments (Wang et al. 2017).

The idea of incorporating the EDFM is identical to the well handling method in traditional reservoir simulations (Peaceman 1978; Wu 2000). The pressure inside fracture, p_f , the discrete pressure in the grid block containing this fracture, p_i , and the volumetric flow rate, q_i between these two, are related by a fracture-index FI_i :

$$q_i = FI_i \frac{kk_r}{\mu} (p_i - p_f) \quad (4.17)$$

where k is the average (such as harmonic-weighted) absolute permeability at the interface; k_r is the average fluid phase relative permeability through the upstream weighting scheme; μ is the fluid phase dynamic viscosity, and the fracture-index FI_i is defined as:

$$FI_i = \frac{A_i}{d_m + d_f} \quad (4.18)$$

where A_i is the common interface area between the intersected block and the fracture; d_m and d_f are distances from the matrix grid block and the fracture to this interface according to EDFM assumptions.

In the X-FEM method, in addition to local element nodes according to the finite element method, the near fracture area is enriched by incorporating both discontinuous fields and the near-tip asymptotic fields (Moës et al. 1999; Sukumar et al. 2000). The discretized displacement can be expressed as follows:

$$\mathbf{u}(\mathbf{x}) = \sum_{i \in I} \mathbf{u}_i h_i + \sum_{j \in J} \mathbf{b}_j h_j H(\mathbf{x}) + \sum_{k \in K} h_k \left(\sum_{l=1}^4 \mathbf{c}_k^l F_l(\mathbf{x}) \right) \quad (4.19)$$

where $\mathbf{u}(\mathbf{x})$ is the displacement at the location \mathbf{x} ; The set I consists of local element nodes; The set K includes those nodes of which the closure support the crack front, and the set J is the

set of nodes which support crack and do not belong to \mathbf{K} . The vector \mathbf{u}_i , \mathbf{b}_j and \mathbf{c}_k^l are the displacement at nodes i , j and k , respectively; \mathbf{h} is the displacement interpolation function; $H(\mathbf{x})$ is the discontinuous Heaviside function:

$$H(x) = \begin{cases} -1 & \text{if } x > 0 \\ +1 & \text{if } x < 0 \end{cases} \quad (4.20)$$

$F_l(\mathbf{x})$ is the asymptotic crack tip functions based on the asymptotic features of the displacement field at the crack tip:

$$F_l(\mathbf{x}) = \left\{ \sqrt{r} \sin\left(\frac{\theta}{2}\right), \sqrt{r} \cos\left(\frac{\theta}{2}\right), \sqrt{r} \sin\left(\frac{\theta}{2}\right) \sin(\theta), \sqrt{r} \cos\left(\frac{\theta}{2}\right) \sin(\theta) \right\} \quad (4.21)$$

where (r, θ) are the local polar coordinates at the tip.

4.3 The Coupling Principles

Strong fluid-solid coupling mechanics makes the simulation of fluid-driven fracture propagation processes quite challenging. As demonstrated in Figure 4-2, at least three physical processes (fluid flow, solid deformation, and fracture growth) and six relationships need to be considered (Shlyapobersky 1985). Each arrow in this illustration represents a relationship described by numbers:

1. Solid deformation changes the width of fractures and thus affects the effective fracture permeability as well as the fracture volume;
2. Fluid flow induces solid deformation by the hydraulic loadings on crack surfaces;
3. Fracture propagates when the stress state near the fracture tip meets the propagation criterion;
4. The growth of fractures causes the redistribution of the stress and strain fields;
5. Fluid flow is affected by the fracture growth since fractures provide a high-conductivity pathway;
6. Fluid flow does not influence fracture growth directly but via the solid deformation as analyzed above.

In this section, we describe physical explanations and mathematical equations on how to link these independent modules, which is the critical task and major difficulty in the coupling. The link from fluid flow to solid deformation treats the fluid pressure force on the fracture surface as an internal boundary. The converse link takes the calculated fracture widths and corrects fracture permeability and the fracture volume. The geomechanics effect in the porous media caused by the change of pore pressure is not included in this study; one can refer to other literature for this part (Rutqvist et al. 2002; Minkoff et al. 2003; Hu et al. 2013).

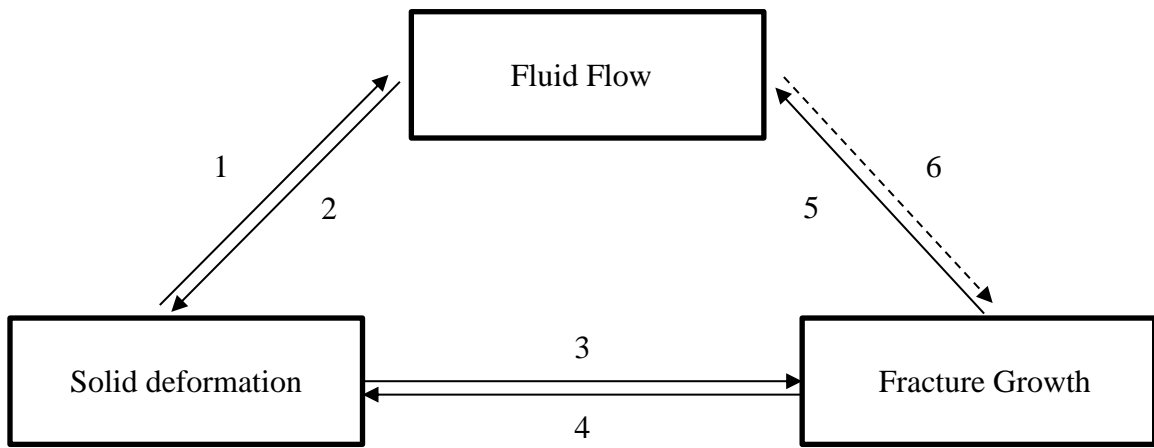


Figure 4-2 Interactions among fluid flow, solid deformation and fracture growth

4.3.1 Solid Deformation on Fluid flow

Solid deformation affects fluid flow by changing fracture widths, which determines the fracture permeability as well as the fracture volume. The crack opening displacement, as shown in **Error! Reference source not found.**, equals to the difference between two internal displacements on both sides of the fracture:

$$w = \bar{U}^{c+} - \bar{U}^{c-} \quad (4.22)$$

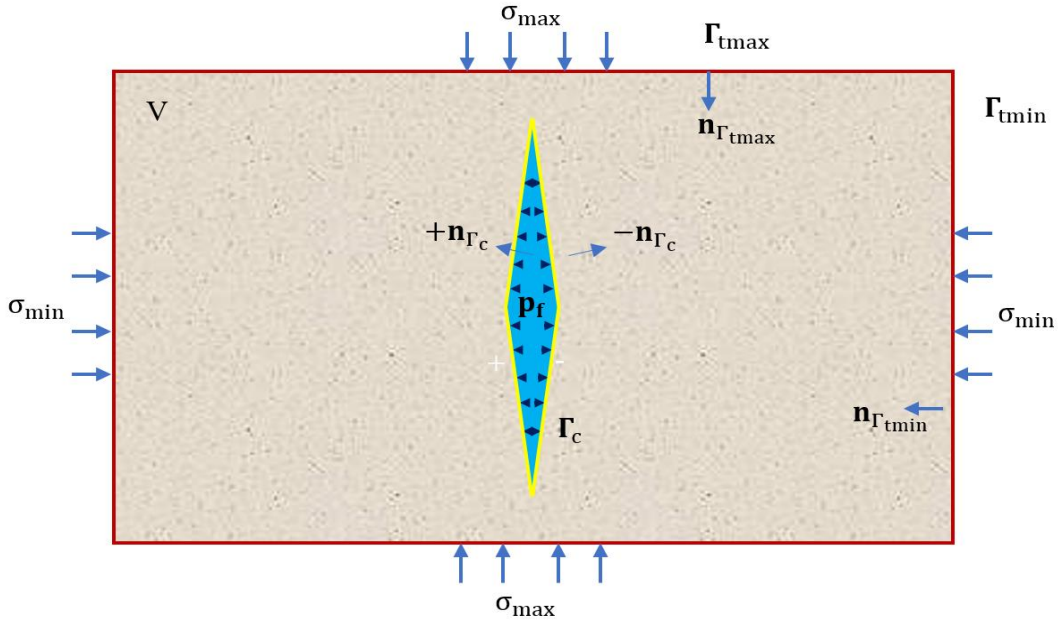


Figure 4-3 Sketch diagram for a two-dimensional body

Each internal displacement can be discretized as a linear combination of node displacements, which is described in Eq. (4.19). Thus, the crack opening displacement can be obtained from the node displacement vector. This expression can be further simplified considering only the Heaviside function and the first asymptotic crack tip function in Eq. (4.19) are discontinuous across the fracture face.

$$\begin{aligned}
 \mathbf{w} = & \left\{ \sum_{i \in I} \mathbf{u}_i h_i^+ + \sum_{j \in J} \mathbf{b}_j h_j^+ H(\mathbf{x}^+) + \sum_{k \in K} h_k^+ \left[\sum_{l=1}^4 \mathbf{c}_k^l F_l(\mathbf{x}^+) \right] \right\} \\
 & - \left\{ \sum_{i \in I} \mathbf{u}_i h_i^- + \sum_{j \in J} \mathbf{b}_j h_j^- H(\mathbf{x}^-) + \sum_{k \in K} h_k^- \left[\sum_{l=1}^4 \mathbf{c}_k^l F_l(\mathbf{x}^-) \right] \right\} \\
 = & 2 \sum_{j \in J} \mathbf{b}_j h_j^+ H(\mathbf{x}^+) + 2 \sum_{k \in K} h_k^+ \mathbf{c}_k^1 \sqrt{r}
 \end{aligned} \tag{4.23}$$

For a given fracture segment, its aperture is the length of the displacement:

$$w_f = |\mathbf{w}| \tag{4.24}$$

The fracture aperture determines the fracture permeability according to the cubic law:

$$k_f = \frac{w_f^2}{12} \quad (4.25)$$

The volume of fracture element, as shown in Eq. (4.5), is related to the width by assuming local width variance in one grid block is negligible:

$$V_f = w_f \cdot l_f \cdot h_f \quad (4.26)$$

where l_f and h_f are the length and height of the fracture element, respectively.

4.3.2 Fluid Flow on Solid Deformation

Fluid flow induces solid deformation by the hydraulic loading acting on crack surfaces. As shown in Figure 4-3, the linear elastic body, which contains fractures filled with fluids, subjects to forces from fluids on crack surfaces. This internal boundary condition can be described as:

$$\sigma = p_f \mathbf{n}_{\Gamma_c} \quad \text{on } \Gamma_c \quad (4.27)$$

where σ is the stress vector; p_f is the fluid pressure in scalar form; Γ_c denotes this inner boundary by fractures; and \mathbf{n}_{Γ_c} is the normal vector of this boundary.

In the weak form of stress equilibrium (Eq. (4.14)), this boundary condition appears in the residual part:

$$\int_{\Gamma_c} \bar{U}^{cT} (p_f \mathbf{n}_{\Gamma_c}) d\Gamma_c = \int_{\Gamma_c^+} \bar{U}^{c+T} (p_f \mathbf{n}_{\Gamma_c^+}) d\Gamma_c^+ + \int_{\Gamma_c^-} \bar{U}^{c-T} (p_f \mathbf{n}_{\Gamma_c^-}) d\Gamma_c^- \quad (4.28)$$

where Γ_c^+ and Γ_c^- are two fracture faces; $\mathbf{n}_{\Gamma_c^+}$ and $\mathbf{n}_{\Gamma_c^-}$ are their associated normal vector pointing outside of the fracture. Since the angle between two fracture faces is close to zero, these two normal vectors can be approximated in opposite directions.

$$\mathbf{n}_{\Gamma_c^+} \approx -\mathbf{n}_{\Gamma_c^-} \quad (4.29)$$

Substitute Eq. (4.22), Eq. (4.23) and Eq. (4.29) into Eq. (4.28), we have:

$$\begin{aligned}
& \int_{\Gamma_c^+} \bar{\mathbf{U}}^{c+T} \left(p_f \mathbf{n}_{\Gamma_c^+} \right) d\Gamma_c^+ + \int_{\Gamma_c^-} \bar{\mathbf{U}}^{c-T} \left(p_f \mathbf{n}_{\Gamma_c^-} \right) d\Gamma_c^- = \int_{\Gamma_c^+} \left(\bar{\mathbf{U}}^{c+T} - \bar{\mathbf{U}}^{c-T} \right) \left(p_f \mathbf{n}_{\Gamma_c^+} \right) d\Gamma_c^+ \\
& = \int_{\Gamma_c^+} \left(2 \sum_{j \in J} \mathbf{b}_j h_j^+ H(\mathbf{x}^+) + 2 \sum_{k \in K} h_k^+ \mathbf{c}_k^l \sqrt{r} \right) \left(p_f \mathbf{n}_{\Gamma_c^+} \right) d\Gamma_c^+
\end{aligned} \tag{4.30}$$

The equation above indicates the pressure force acting on the fracture surface can be transferred to the force acting on element nodes, which can be incorporated directly into the \mathbf{R} matrix in Eq. (4.14). In this way, the effect of fluid flow on solid deformation is captured.

4.3.3 Solid Deformation on Fracture Propagation

According to the theory of linear elastic fracture mechanics (LEFM), a fracture can propagate if the stress intensity factor exceeds the fracture toughness. In this study, we use the maximum circumferential stress criterion for two-dimensional scenarios (Shih and Asaro 1988; Pais et al. 2010). The fracture can grow if the following condition is met:

$$K_{\theta_c} = \cos \frac{\theta_c}{2} \left(K_I \cos^2 \frac{\theta_c}{2} - \frac{3}{2} K_{II} \sin \theta_c \right) \geq K_{IC} \tag{4.31}$$

where K_{θ_c} is the maximum circumferential stress; K_{IC} is the fracture toughness, which is a property of the material; θ_c is the direction of fracture propagation:

$$\theta_c = 2 \tan^{-1} \frac{1}{4} \left[\frac{K_I}{K_{II}} - \text{sign}(K_{II}) \sqrt{\left(\frac{K_I}{K_{II}} \right)^2 + 8} \right] \tag{4.32}$$

In Eq. (4.31) and Eq. (4.32), K_I and K_{II} are the mode I and mode II stress intensity factors, which are defined as:

$$K_I = \lim_{r \rightarrow 0} \sqrt{2\pi r} \sigma_{xx}(r, 0) \tag{4.33}$$

$$K_{II} = \lim_{r \rightarrow 0} \sqrt{2\pi r} \sigma_{xy}(r, 0) \tag{4.34}$$

where σ_{xx} and σ_{xy} are the normal stress in the x-direction and the shear stress, respectively; r denotes the distance to the fracture tip. The length of crack growth can be correlated with the stress intensity factor as well according to Paris' law (Paris and Erdogan 1963).

For 3D cases, the mode I stress intensity factor at the fracture tip can be calculated as (Yew and Weng 2014)

$$K_I = \frac{E}{8(1+v)(1-v)} \left(\frac{2\pi}{r} \right)^{1/2} w(r) \quad (4.35)$$

4.3.4 Fracture Propagation on Solid Deformation and Fluid Flow

The growth of fractures changes solid- and fluid-mechanical behaviors of the system, which are captured by the X-FEM and the EDFM without remeshing. The fracture path can be obtained explicitly by a set of discrete points or implicitly via the level-set method (Sukumar et al. 2001). In X-FEM, as indicated in Eq. (4.19), another two sets of degrees of freedom (DOF) are introduced for fractures. Their associated enrichment functions depend on the fracture path, which can be obtained directly through the geometric calculation (see Eq. (4.20) and Eq. (4.21)). With the growth of fracture, the number of DOFs as well as their associated enrichment functions change correspondingly (Figure 4-4). Ultimately, the global stiffness matrix (matrix \mathbf{K} in Eq. (4.14)) is reconstructed. In the EDFM, the new fracture segment is represented by the addition of one or one assemblage of computational volume elements. Critical parameters for this incorporation are the contacting area and the average distance, which can also be geometrically obtained given the fracture path.

Figure 4-4 illustrates a 2D fracture before and after growth, associated with enrichment nodes for X-FEM and fluid-matrix flow connections for the EDFM. Three types of DOFs in X-FEM are demonstrated with blue dots, black squares and black circles (see annotations in Figure 4-4). The connection between the matrix grid block and the embedded fracture element in EDFM is represented by the black arrow. Comparisons of these two scenarios show the change of DOFs for both fluid flow and solid deformation simulation. Figure 4-5 demonstrates the discretization method for a 3D fracture, in which the fracture is represented by a set of connected 2D

geometries according to the EDFM (Wang et al. 2017) and by two types of enrichment nodes according to the X-FEM (Sukumar et al. 2000).

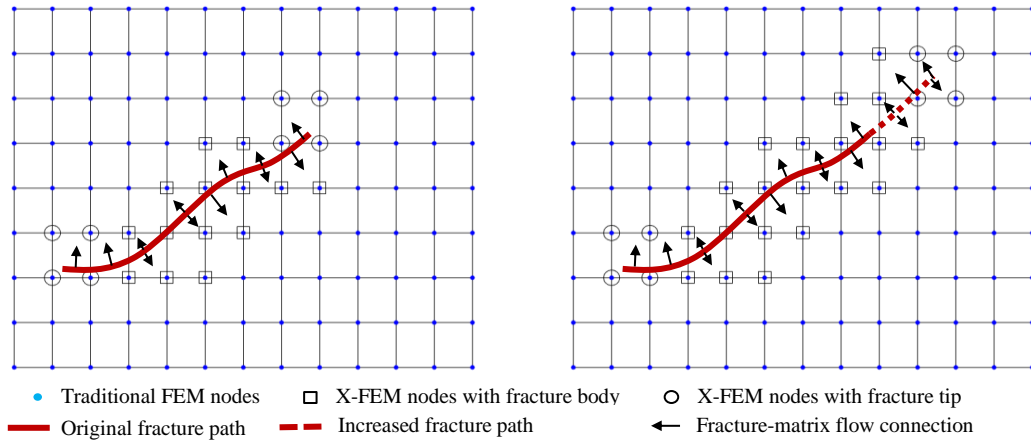


Figure 4-4 The path and discretization nodes of a fracture before (left) and after (right) fracture propagation

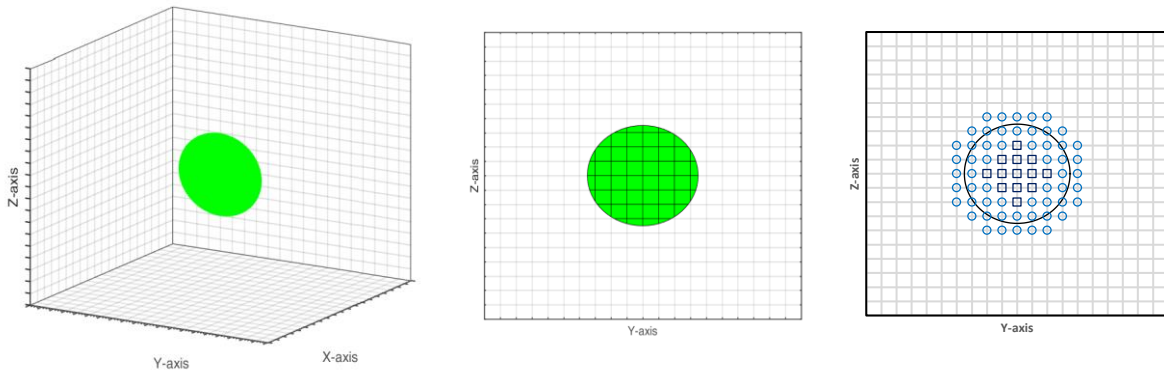


Figure 4-5 A three-dimensional circular fracture (left), its representations by the EDFM (mid) and by the X-FEM (right)

4.3.5 Numerical Coupling Procedures

Three different routines are developed adequately: (1) modeling fluid flow in porous media with fractures based on the EDFM; (2) modeling solid deformation with fractures based on the X-FEM; and (3) determining if fracture propagates (if yes, calculating propagation length and directions). These three strongly interacted modules are coupled in two stages, as demonstrated in Figure 4-7 by two loops. The goal of this two-stage coupling is obtaining a

multi-physics field which satisfies all physics discussed above. This multi-physics field combines pressure field, stress field, and fracture geometry.

The iterative coupling method is selected for the coupling between fluid flow and solid deformation in the inner loop. Fluid flow variables and geomechanics variables are solved separately and sequentially by corresponding routines, and the coupling terms are interacted on at each time step. Data transfer between these two routines is described in sections above. The iterative coupling procedure is repeated until a satisfactory convergent fracture width is obtained. The criterion of convergence is

$$\max \left(\frac{|w_{k+1,i}^n - w_{k,i}^n|}{w_{k+1,i}^n} \right) < \varepsilon \quad (4.36)$$

where ε is an assigned tolerance.

Note that this iterative method uses an initial guess to generate successive approximations to the solution. For the first time step, this initial estimate is obtained by pre-running the iterative coupling with an infinite fracture permeability. For the following time steps, the converged result at the last time step is used.

We also adopt the Picard iteration technique to mitigate numerical oscillations and accelerate the convergence rate.

$$w_{k+1}^{(n)} = \alpha F(w_k^{(n)}) + (1-\alpha)w_k^{(n)}, \quad 0 < \alpha \leq 1 \quad (4.37)$$

where α is the Picard coefficient; $w_k^{(n)}$ is the fracture width in the k th iteration during the n th time step; $F(w_k^{(n)})$ is the calculated fracture width after one loop of calculations based on $w_k^{(n)}$; and $w_{k+1}^{(n)}$ is the updated fracture width for the next iteration. For a 2D numerical test, the iteration number reduces from 142 to 19 by changing the Picard coefficient from 1.0 to 0.5 (Figure 4-6).

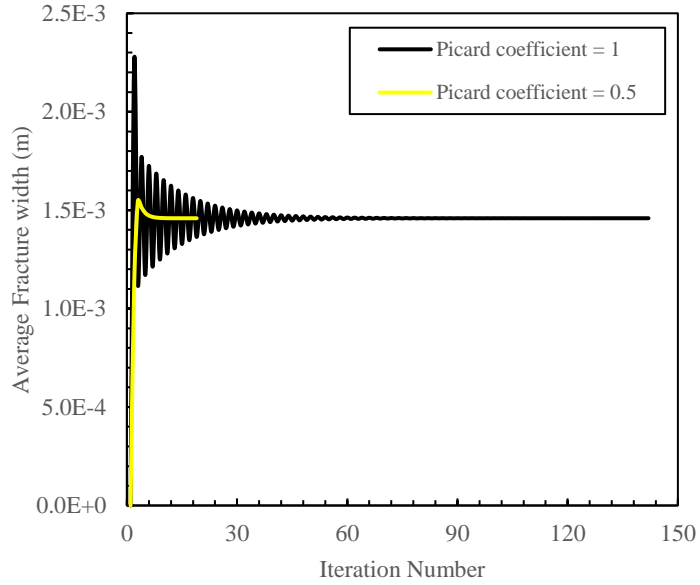


Figure 4-6 Average fracture width as a function of the iteration number with Picard coefficient equals to 0.5 and 1.0

Once the iteration between these two modules is converged, the stress intensity factor is calculated and compared with the fracture toughness to determine if the fracture propagates (Eq. (4.31)). If the fracture propagation criterion is not met, which means the fracture in this condition is stable, the coupling convergence among these three modules is achieved. Otherwise, the fracture propagation fracture geometry is updated for the next large-loop iteration (Figure 4-7).

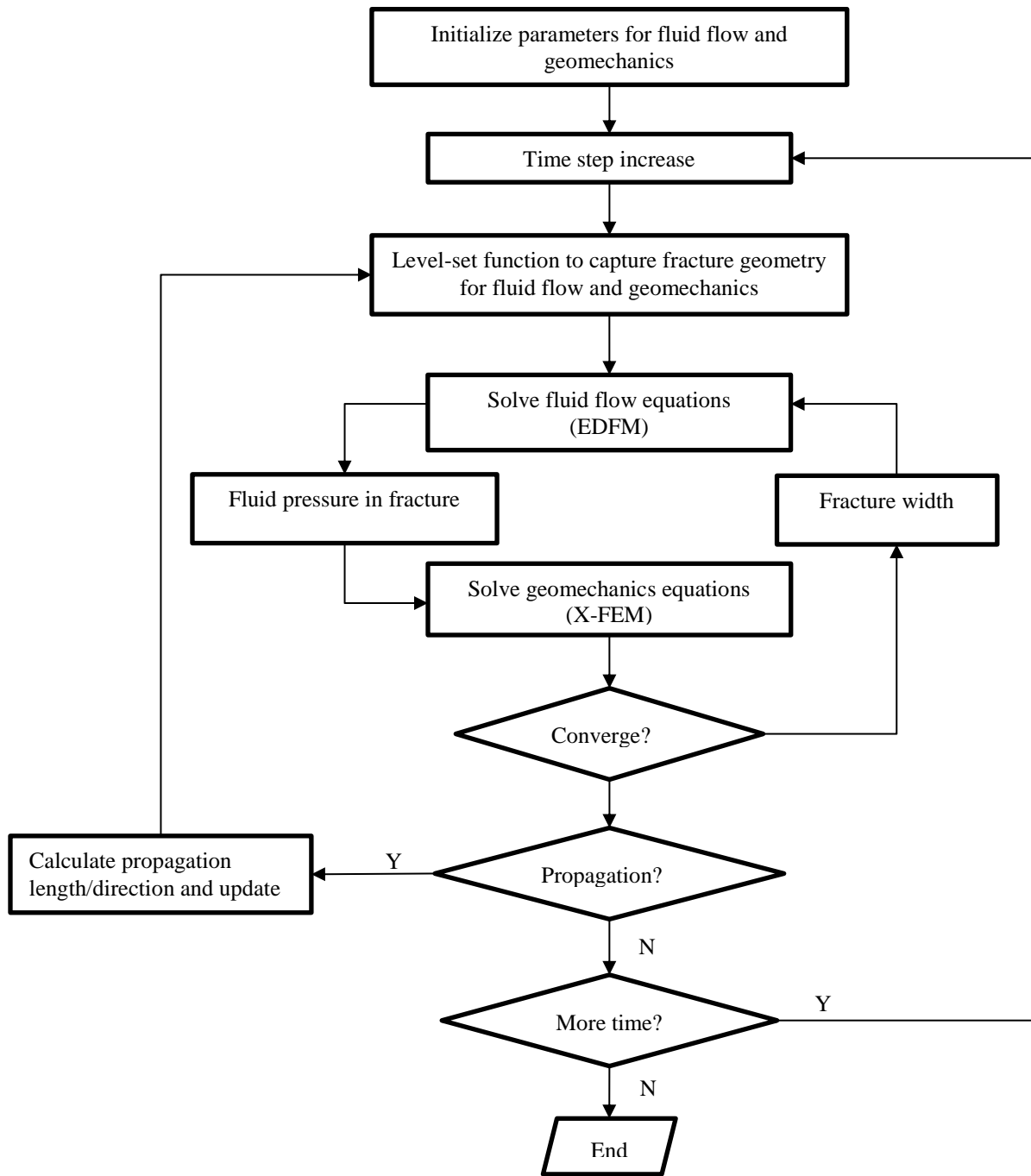


Figure 4-7 The workflow of a two-stage coupling method for fluid flow, solid deformation and fracture growth simulation

4.4 Validations

In this section, two numerical experiments are conducted to evaluate the accuracy of our developed X-FEM and EDFM codes. The in-house program used in this study is written in MATLAB. The code structure is illustrated in Appendix A. The X-FEM codes are developed

based on an open-source 2D MATLAB X-FEM codes (Pais 2011). The validation benchmarks chosen for these two tests are analytical solutions.

4.4.1 Solid Deformation Model Validations

An angled center crack is put inside a plate which is subjected to a far-field uniaxial stress. Values of the plate dimensions, fracture lengths and stresses are demonstrated in Figure 4-8. The plate dimensions are five times larger than the crack length to approximate the infinite setting. The exact stress intensify factors for the infinite plate is given by (Tada et al. 2000)

$$K_I = \sigma \sqrt{\frac{\pi L}{2}} \cos^2(\beta) \quad (4.38)$$

$$K_{II} = \sigma \sqrt{\frac{\pi L}{2}} \sin(\beta) \cos(\beta) \quad (4.39)$$

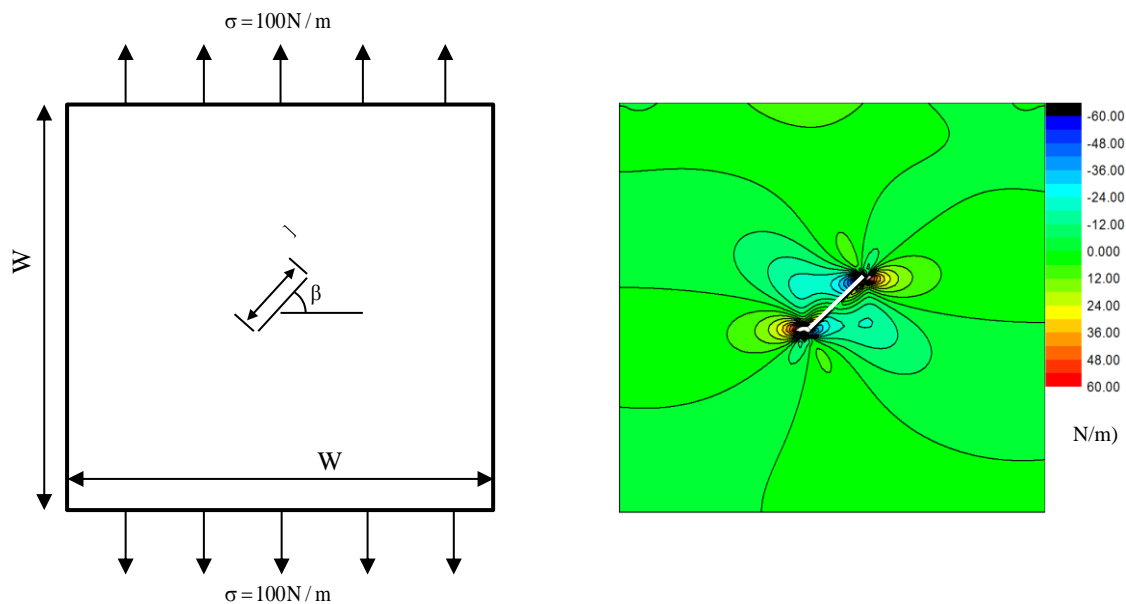


Figure 4-8 Plane with a center fracture at angle β and simulated shear stress contours

Simulations with various fracture angles are performed. The right plot in Figure 4-8 shows the simulated shear stress contour when the fracture angle is $\pi/4$. Figure 4-9 shows numerically calculated stress intensity factors have an excellent agreement with the analytical solution for the entire range of β .

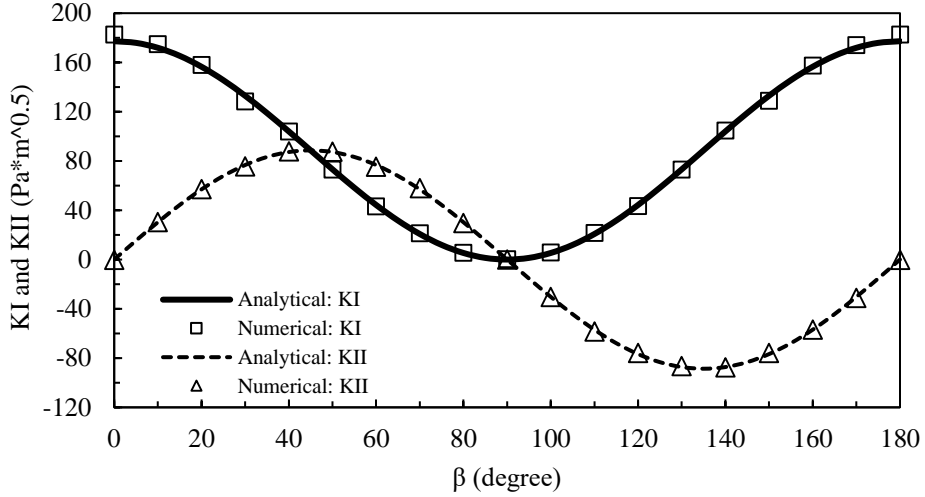


Figure 4-9 Comparisons between numerical and analytical stress intensity factor

4.4.2 Fluid Flow Model Validations

An angled center crack is put inside a closed-boundary 2D reservoir with the unit thickness. Fluid is produced at a constant rate from the fracture center. Gringarten et al. (Gringarten et al. 1974) give the general analytical solution of the well pressure with a “uniform flux” or “infinite-conductivity” vertical fracture:

$$p_D(t_{Dx}, |x_D| < 1) = \frac{\sqrt{\pi t_{Dx}}}{2} \left[\operatorname{erf}\left(\frac{1-x_D}{2\sqrt{t_{Dx}}}\right) + \operatorname{erf}\left(\frac{1+x_D}{2\sqrt{t_{Dx}}}\right) \right] - \frac{1-x_D}{4} \operatorname{Ei}\left[-\frac{(1-x_D)^2}{4t_{Dx}}\right] - \frac{1+x_D}{4} \operatorname{Ei}\left[-\frac{(1+x_D)^2}{4t_{Dx}}\right] \quad (4.40)$$

where erf and Ei denote the error function and exponential integral functions, respectively; $x_D = 0$ for the uniform flux case, and $x_D = 0.732$ for the infinite conductivity vertical fracture case.

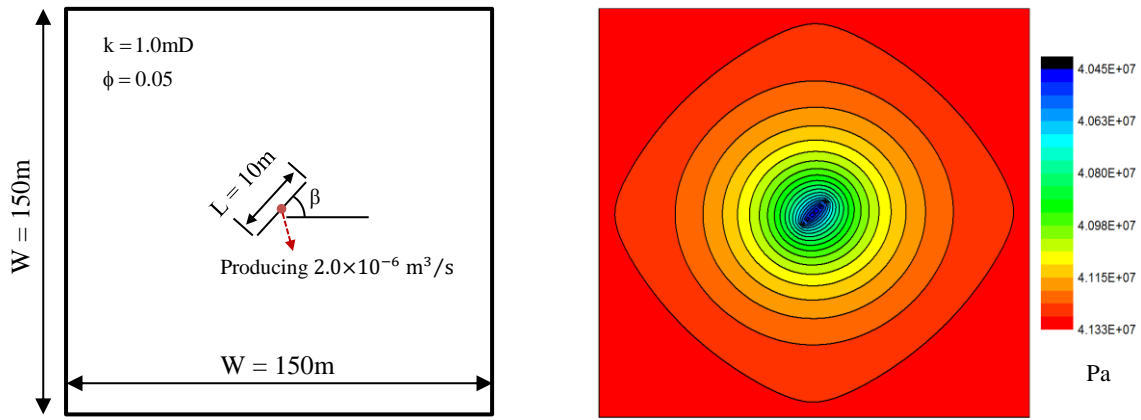


Figure 4-10 Plane with a centered fracture with angle β and simulated pressure contour after one minute of production

Simulations with various fracture angles are conducted. Since the reservoir can be approximated as the infinite set, the pressure data at the production point with various fracture angles keep the same. The right plot in Figure 4-10 shows the pressure contour after one minute of production. Figure 4-11 plots analytical solutions of the dimensionless pressure at the fracture center as well as numerical solutions with various fracture angles. The good agreement verifies our numerical implementations about the EDFM is correct.

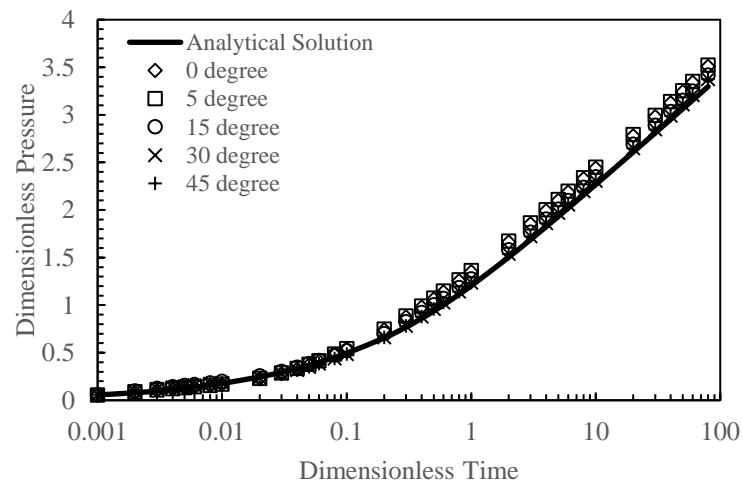


Figure 4-11 Comparisons between numerical and analytical dimensionless pressure

4.5 Numerical Results

The developed coupling method is here applied to two fracture propagation problems in two dimensions and three dimensions, respectively. Models designed for these two problems are based on the classical KGD model and the penny-shaped fracture model. The primary objective of these two examples is to demonstrate the capacity of our developed numerical coupling approach in accurately simulating the complex multi-physics in the fracture propagation process. Note that though fracture geometries in these two illustrative examples are relatively simple, the coupling approach is applicable for complicated-geometry cases because both X-FEM and EDFM can handle fractures with complicated geometries.

4.5.1 Two Dimensional KGD Model

This section simulates a 2D hydraulic fracture propagation problem. The model designed is based on the classical Khristianovic-Geertsma-de Klerk (KGD) model. As demonstrated in Figure 4-12, it composes only one layer of linear elastic medium. Incompressible Newtonian fluid is injected at a constant rate, which initializes and propagates the hydraulic fracture. Both the fracture toughness and the formation permeability are set to be zero following assumptions in the classical KGD model. Rock properties of this layer are summarized in Table 4-1.

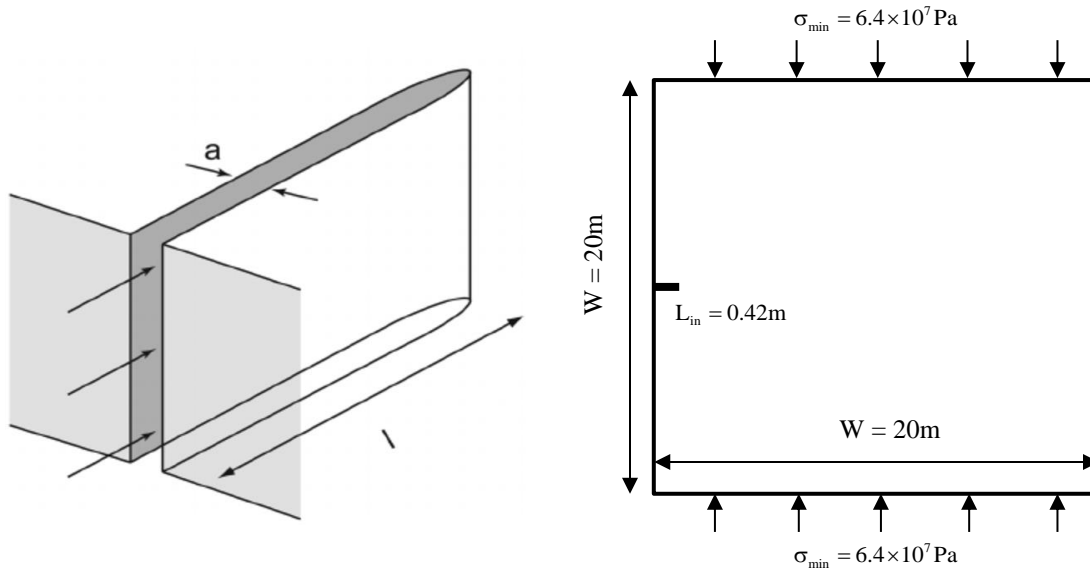


Figure 4-12 Illustration of a KGD model (left modified from Lisjak et al. 2015)) and its numerical setup in this study (right)

Table 4-1 Data in the KGD model

Parameters and Units	Values
Viscosity, Pa*s	1.00
Pumping Time, s	20.0
Pumping Rate, m^3/s	5.00E-05
Thickness of Injection Zone, m	1.00
Minimum Stress, Pa	6.40E+07
Young's modulus, Pa	4.14E+10
Poisson's Ratio	0.20
Toughness, Pa*m^0.5	0
Leakoff Coefficient, m/s^0.5	0

Figure 4-13 - Figure 4-15 present comparisons of fracture half-length, fracture width at the wellbore and net pressure, respectively, which are calculated from numerical and analytical solutions. The analytical solution for the above problem can be found from the textbook (Yew and Weng 2014) as follows:

Fracture length:

$$L = 0.48 \left[\frac{8GQ^3}{(1-v)\mu} \right]^{1/6} t^{2/3} \quad (4.41)$$

Fracture opening width at the wellbore:

$$w_o = 1.32 \left[\frac{8(1-v)Q^3\mu}{G} \right]^{1/6} t^{1/3} \quad (4.42)$$

Wellbore pressure (net):

$$p_{\text{net}} = 0.96 \left[\frac{2G^3 Q \mu}{(1-v)^3 L^2} \right]^{1/4} \quad (4.43)$$

where L is the fracture half-length; w_0 is the maximum opening width of the fracture; p_{net} is the net pressure at the wellbore; G is the shear modulus; Q denotes the pumping rate for the single-wing of the fracture; μ is the viscosity of the fracturing fluids; h is the formation thickness; and t is the pumping time. All parameters in above equations are in SI units.

These comparisons indicate that numerical results are in good agreements with the analytical solution for this problem. The discrepancy in the early time is because the fracture is assumed to grow from an initial length of 0.42m instead of zero. The difference afterward is caused by grid resolutions (cell size) in the numerical approach. Note that the numerical method in this study simulates fracture propagation with a single wing.

The contour of the normal stress in the x-direction, the normal stress in the y-direction and the shear stress when the fracture length is 1.21m is plotted in Figure 4-16. It can be seen that the stress concentration effect at the fracture tip is captured in the simulation result. Fracture half-width profiles at different injection time are shown in Figure 4-17.

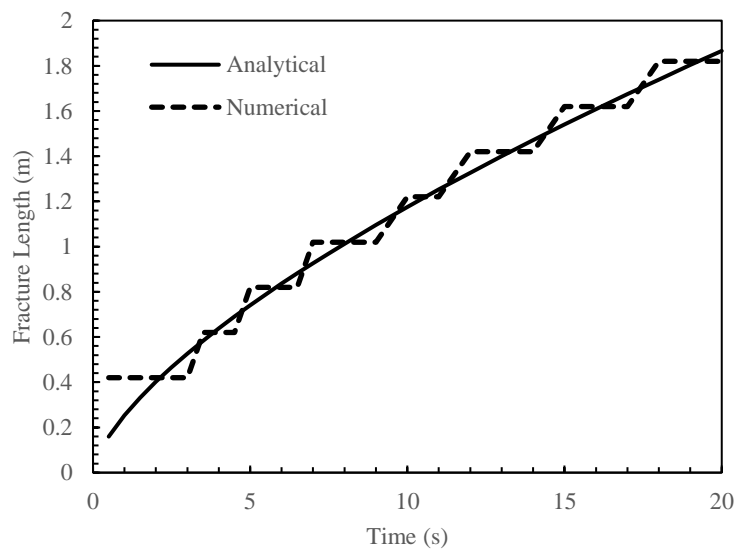


Figure 4-13 Comparisons of the propagated fracture radius vs. time between the analytical solution and the numerical solution for the KGD fracture model

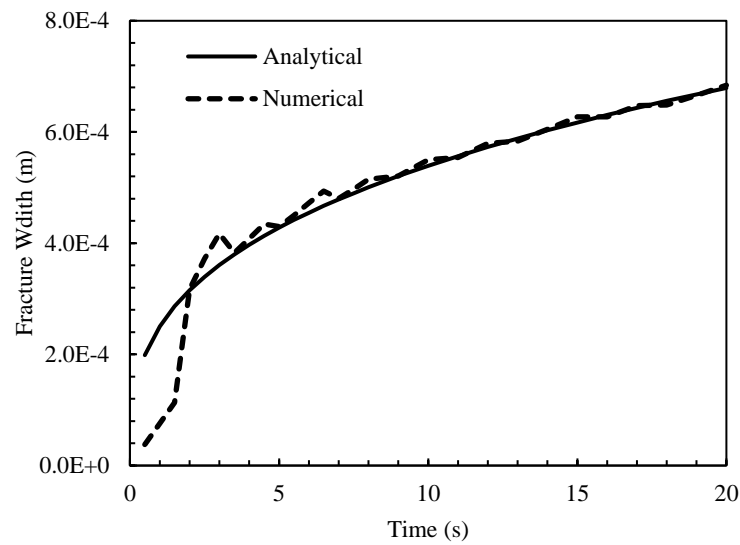


Figure 4-14 Comparisons of the fracture width at inlet vs. time between the analytical solution and the numerical solution for the KGD fracture model

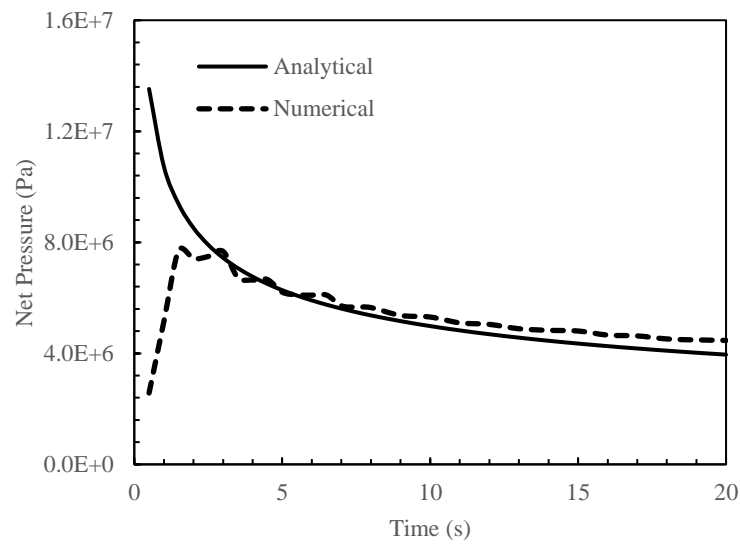


Figure 4-15 Comparisons of the net pressure at inlet vs. time between the analytical solution and the numerical solution for the KGD fracture model

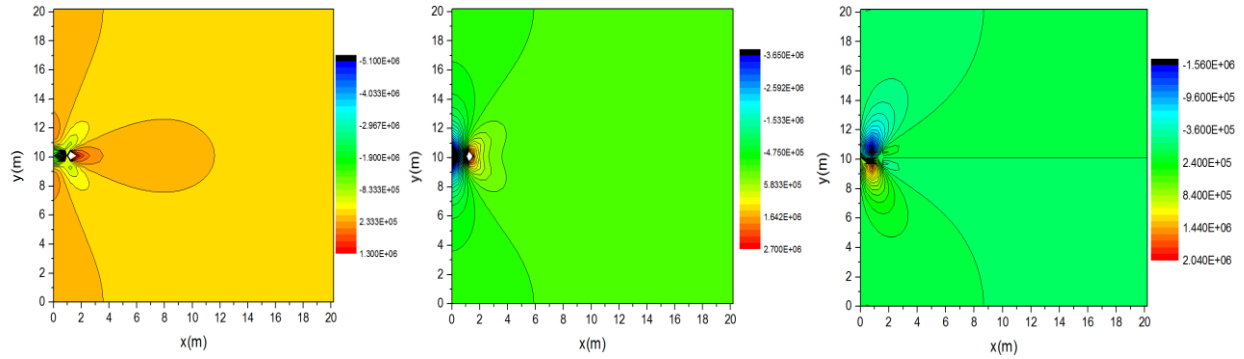


Figure 4-16 From left to right (contours of the normal stress in the x-direction, the normal stress in the y-direction and shear stress) when fracture length is 1.2m

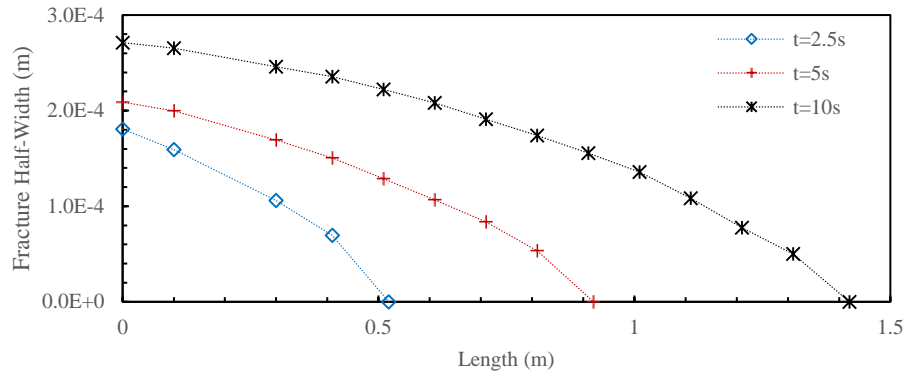


Figure 4-17 Fracture geometry (half-width vs. length) at injection time of 2.5s, 5s and 10s

4.5.2 Three-Dimensional Penny-Shaped Fracture Model

As demonstrated in Figure 4-18, the problem involves an axisymmetric hydraulic fracture propagation in an 3D infinite elastic medium. Incompressible Newtonian fluid is injected at the fracture center with a constant rate, which initializes and propagates the hydraulic fracture. In the base case, the fracture toughness is $4 \times 10^6 \text{ Pa}\sqrt{\text{m}}$, and the formation permeability is zero. Six other cases with various fracture toughness and formation permeabilities are also simulated to conduct the sensitivity analysis. The analytical solution considering both are not available, and only comparisons between the simulation results and analytical results for cases without fluid leak-off are presented. Input parameters for the case are listed in Table 4-2.

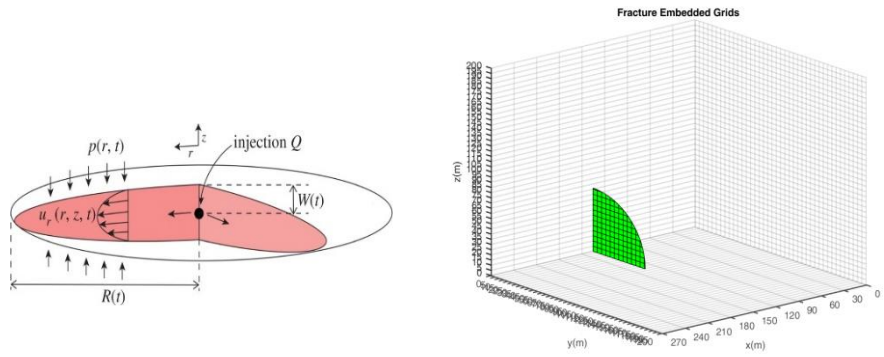


Figure 4-18 Illustration of a 3D penny-shaped fracture (Lisjak et al. 2015) and associated modeling representations

Table 4-2 Input parameters for the 3D penny-shaped fracture modeling

Parameters and Units	Values
Minimum Stress, Pa	6.40E+07
Initial reservoir pressure, Pa	3.40E+07
Young's Modulus, Pa	5.83E+09
Poisson's ratio	0.3
Viscosity, Pa*s	0.1
Constant injection rate, m^3/s	0.106
Toughness, Pa*m^0.5	4.00E+06
Reservoir Permeability, m^2	0

Only a quarter of the model is simulated by considering symmetry in this problem. The fracture is positioned in the mid of the X-axis. This quarter-model has dimensions of $45\text{m} \times 150\text{m} \times 150\text{m}$ which contains 8,100 elements. The size of each element is $5\text{m} \times 5\text{m} \times 5\text{m}$. The reservoir permeability is zero to model the impermeable rock condition as assumed in the analytical solution. If the fracture propagation criteria are met, the increase of fracture radius is set to be 2m. In addition to the base case, three other cases are simulated with different fracture toughness (0 , $6.0 \times 10^6 \text{ Pa}\sqrt{\text{m}}$, and $8.0 \times 10^6 \text{ Pa}\sqrt{\text{m}}$). Both viscosity-dominated and toughness-

dominated scenarios are covered in these four cases. Analytical solutions for the fracture radius of this penny-shaped fracture with viscosity-dominated ($K < 1$) regime and toughness-dominated regime ($K > 4$) are given by (Savitski and Detournay 2002):

$$r = \begin{cases} 0.6976 \left[\frac{Q^3 E}{12(1-v^2)\mu} \right]^{1/9} t^{4/9} & K < 1 \\ \left(\frac{3}{\sqrt{2}\pi} \right)^{2/5} K^{-2/5} \left[\frac{Q^3 E}{12(1-v^2)\mu} \right]^{1/9} t^{4/9} & K > 4 \end{cases} \quad (4.44)$$

where K is the dimensionless fracture toughness as a function of fluid viscosity μ , Young's modulus E , Poisson's ratio v , injection rate Q_0 , injection time t , and fracture toughness K_{IC} .

$$K = 4 \left(\frac{2}{\pi} \right)^{\frac{1}{2}} K_{IC} \left[\frac{t^2 (1-v^2)^{13}}{(12\mu)^5 Q_0^3 E^{13}} \right]^{1/18} \quad (4.45)$$

Figure 4-20 presents comparisons between the numerical solutions and analytical solutions about the fracture radius vs. time with various fracture toughness. It indicates from low toughness ($K_{IC} = 0$) to high ones ($K_{IC} = 8.0 \times 10^6 \text{ Pa}\sqrt{\text{m}}$), all results from the numerical approach are in good agreement with the analytical solutions. Simulated fracture width profiles for the base case at 6 mins and 16 mins are demonstrated in Figure 4-19.

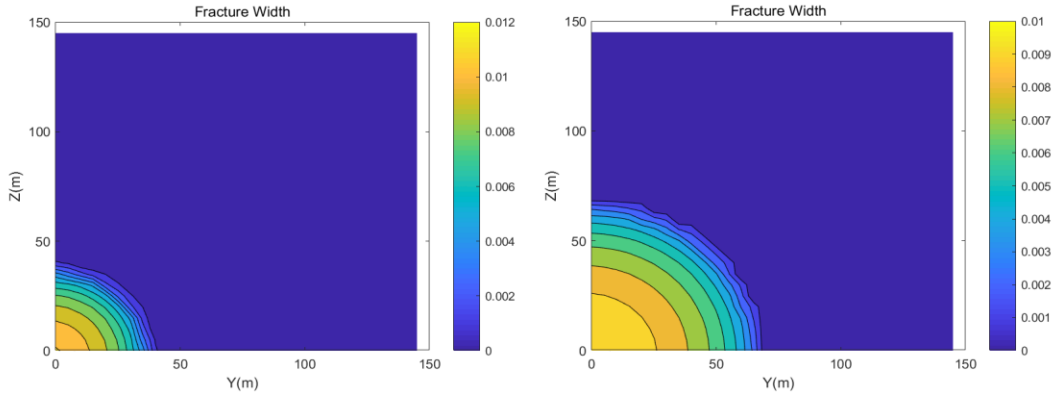


Figure 4-19 Simulated fracture width distributions at six minutes and 16 minutes

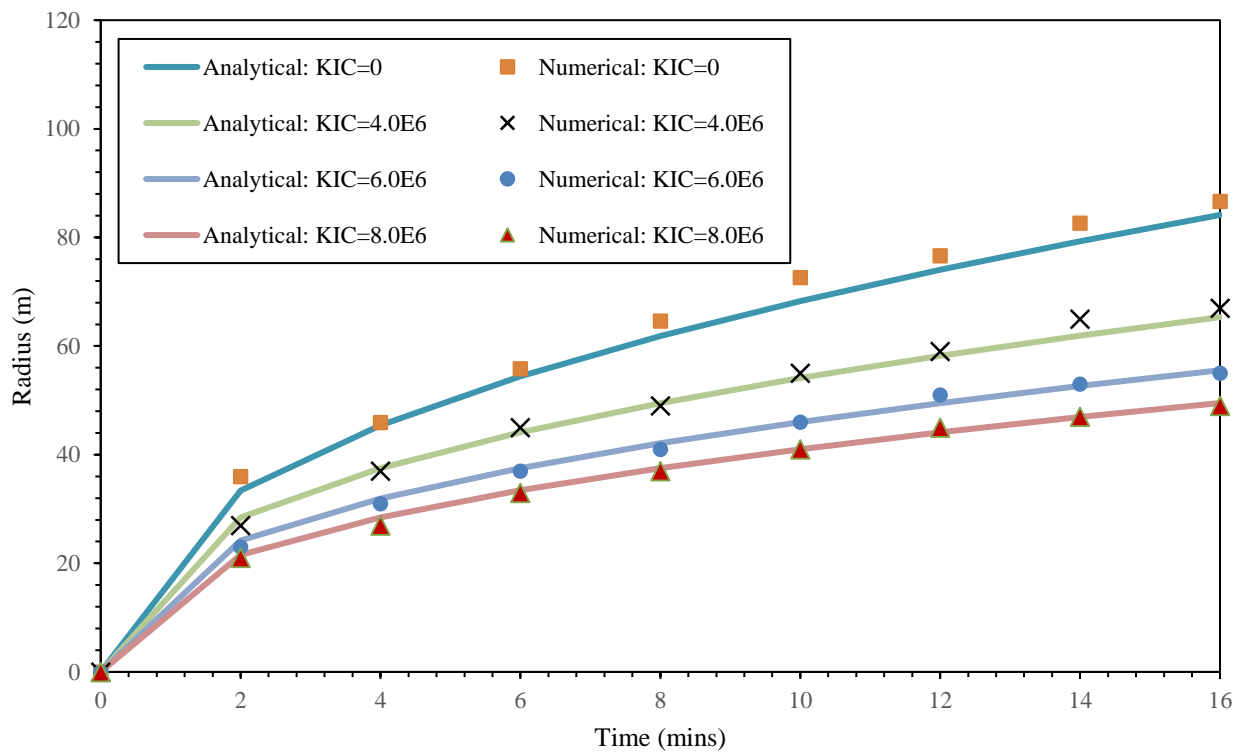


Figure 4-20 Comparisons of the propagated fracture radius vs. time between the analytical solution and the numerical solution with various fracture toughness

We also conducted a sensitivity analysis concerning the reservoir permeability. Three cases with various formation permeability ($1.0 \times 10^{-14} \text{ m}^2$, $5.0 \times 10^{-14} \text{ m}^2$ and $1.0 \times 10^{-13} \text{ m}^2$) are simulated. Simulated fracture radius vs. time in these three cases are compared with the result of the base case, as shown in Figure 4-21. It indicates that the loss of fluid into formations also

governs the fracture extent, like the fracture toughness. The amount of this fluid loss is controlled by the fluid viscosity, formation permeability, fracture-matrix contact area and the fracture-matrix pressure difference. For the highest permeability ($\text{Perm} = 1.0 \times 10^{-13} \text{ m}^2$) case, the fracture radius grows to 31m with 7 minutes of fluid injections. This fracture growth stops afterward because the balance is reached between the fluid injection and the fluid loss into formations. With the decrease of formation permeability, this ultimate fracture radius increases and the time to reach this radius increases as well. One can expect this fracture radius regrows with enough injections when the formation pressure is increased to a value close to the fluid pressure in fractures. But this phenomenon is not observed in the time range of this simulation (16 mins). For the case of zero permeability, the fracture keeps increasing with a gradually slowing down growth rate.

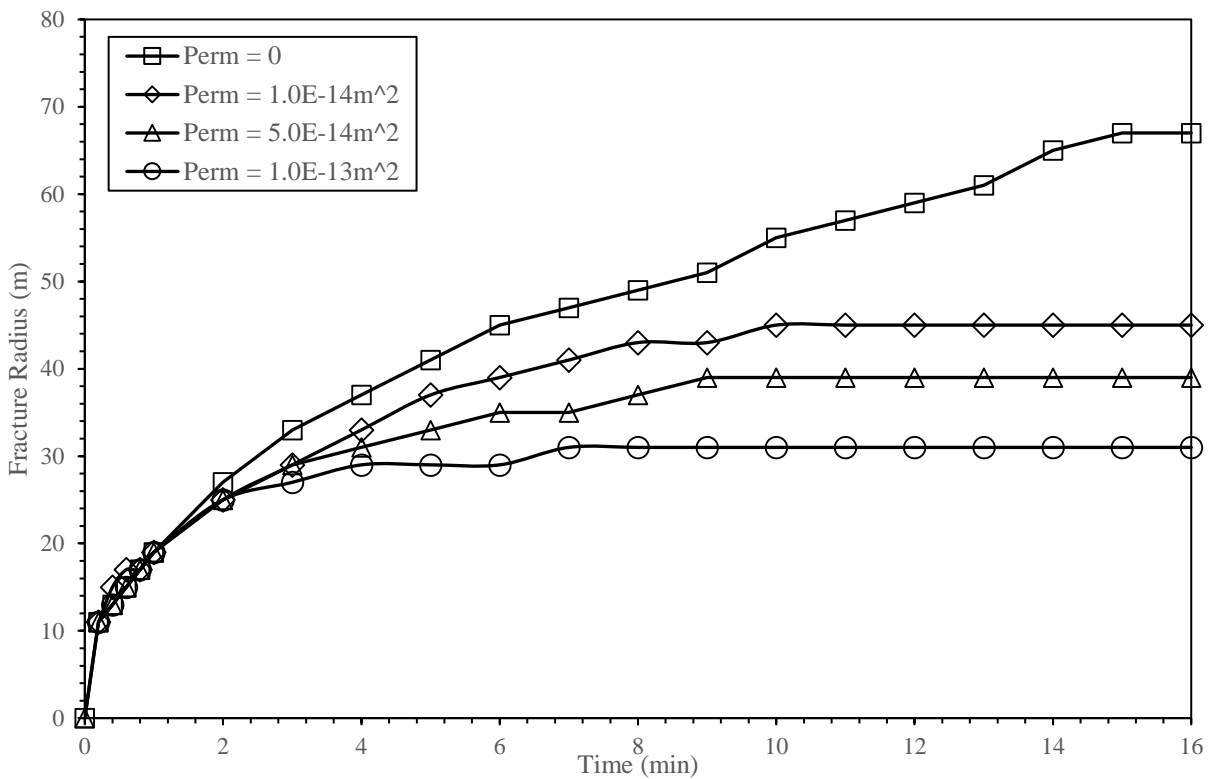


Figure 4-21 Simulated fracture radius vs. time with various reservoir permeabilities

The developed algorithm can calculate six stress components (three normal stresses and three shear stresses) and one fluid pressure with time. Here we show 3D contours of the simulated fluid pressure, xx-normal stress and xy-shear stress after five minutes of injections for

the case with the permeability of $1.0 \times 10^{-13} \text{ m}^2$ (Figure 4-23 - Figure 4-25). Results at four horizontal layers ($z=3\text{m}$, 13m , 23m and 33m) are demonstrated. The simulated radius of the propagated fracture at this time is 29m.

Figure 4-22 - Figure 4-25 demonstrate that this numerical algorithm captures different patterns and scopes for the fields of three coupling physics (fracture propagation, fluid flow and solid deformation) in this problem. Simulation results meet the qualitative expectation as well. The simulated fluid pressure contour cannot be described by the exact linear flow pattern because the time fluid leak-off begins at different fracture locations varies. A slight pressure depletion at the the horizontal layer of $z=33\text{m}$ is observed although the fracture tip hasn't reached this height. This is because fluid flows in the vertical direction with pressure differences in the porous media. The stress concentration effect at the fracture tip, which is a key in the linear elastic fracture mechanics, can be observed in the xy-shear stress contour with different heights.

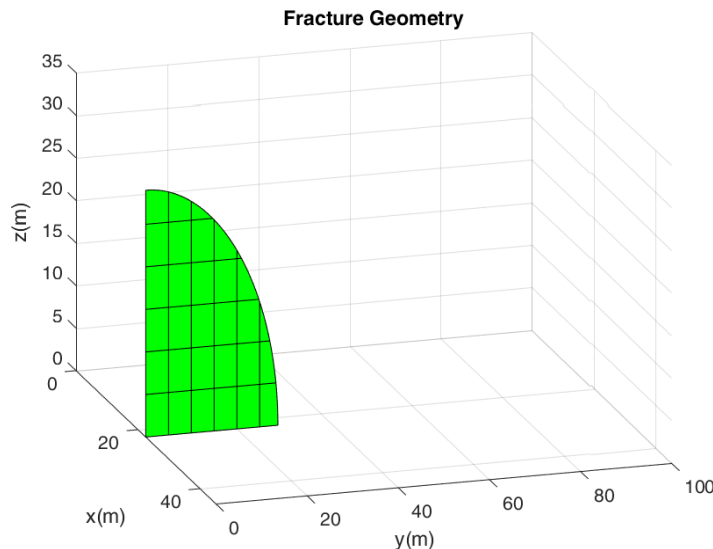


Figure 4-22 Simulated fracture geometry

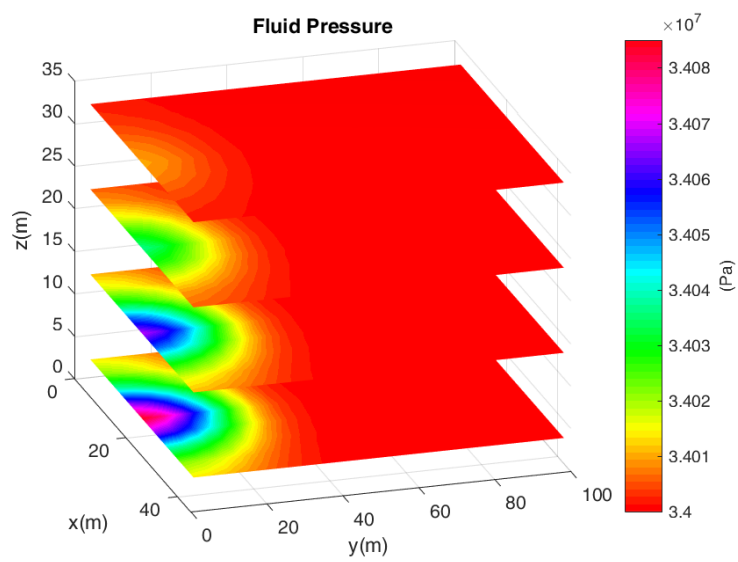


Figure 4-23 Contours of fluid pressure at four horizontal layers

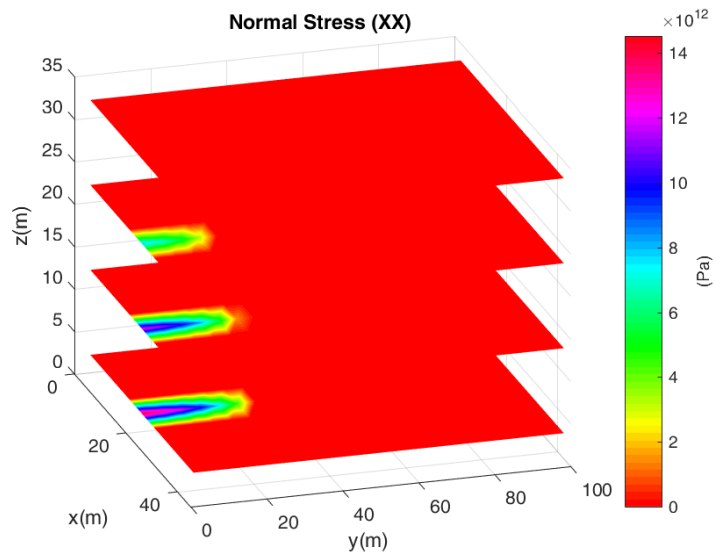


Figure 4-24 Contours of xx-normal stress at four horizontal layers

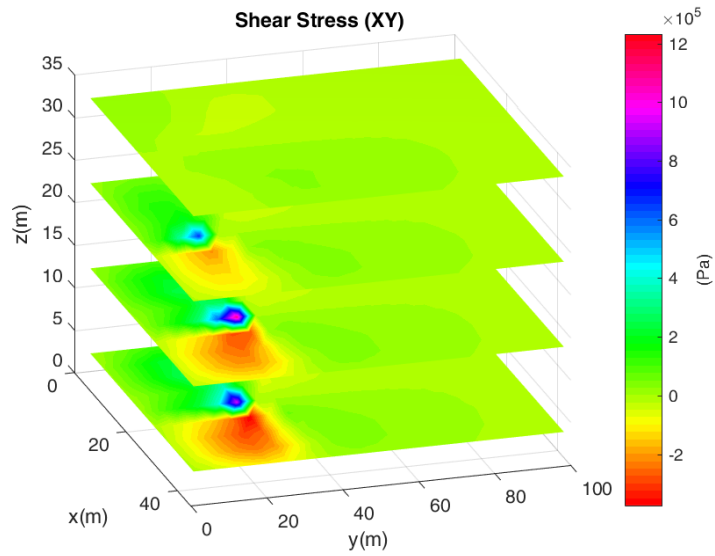


Figure 4-25 Contours of xy-shear stress at four horizontal layers

4.6 Summary

1. We present a coupled simulation strategy combining the embedded discrete fracture method (EDFM) and the extended finite element method (X-FEM) to simulate the fluid-driven fracture propagation process in porous media. Key physics in this process includes three strong coupling mechanics: fluid flow in fractures and porous media, solid deformation with fractures, and fracture propagations can be captured through this numerical approach. Both EDFM and X-FEM avoid the cumbersome construction of unstructured grids to capture fracture paths for fracture-related fluid mechanics and solid mechanics. They also avoid the remeshing for the fracture growth.
2. Mathematical equations on how to link these independent modules as well as numerical techniques on how to accelerate the coupling convergence rate are discussed in detail. The link from fluid flow to solid deformation treats the fluid pressure force on the fracture surface as an internal boundary. The converse link takes the calculated fracture widths and corrects fracture permeability and the fracture volume. The growth of fracture path is calculated based on the stress field from the X-FEM simulation. This fracture growth, in turn, changes solid- and fluid-mechanical behaviors of the system, which are captured by the reconstruction of equations in EDFM and X-FEM.

3. The EDFM and X-FEM are validated via benchmark problems individually and then are coupled to simulate fracture propagation problems in two dimensions and in three dimensions. Simulated multi-physics fields meet understandings qualitatively, and simulated fracture parameters (length, width and net pressure) vs. time match with analytical solutions (KGD for 2D problems and Penny-shaped fracture model for 3D problems) quantitatively.

LIST OF SYMBOLS

Symbol	Description (unit)
A_{ij}	area between connected grid blocks i and j (m^2).
b	Klinkenberg effect factor (Pa)
B_β	formation volume factor for phase β ;
B_w^o	formation volume factor of water at initial bubble point pressure, P_b^o .
C_r	rock compressibility (1/Pa).
d	diameter of wellbore (m).
C_β	compressibility of liquid phase β ($\beta = w$ or o) (1/Pa).
D, D_i	depth of a grid block center (m).
d_1, d_2	distance from center of first and second element, respectively, to their common interface (m).
d_1, d_2	distance from center of first and second element, respectively, to their common interface (m).
g	magnitude of gravitational acceleration (m/s^2).
G	minimum pressure gradient for a Bingham fluid flow (Pa/m).
H	consistence constant of a power-law fluid ($Pa.s^n$)
k	porous medium permeability (m^2).
$k_{r\beta}$	relative permeability to phase β ($\beta = w$ or g).
m	time step level for the AIM scheme (=n for IMPES nodes and =n+1 for fully implicit nodes).
M	molecular weight of air.

n	previous time step level; also used to denote exponential index of a power law fluid.
N	total number of grid blocks of a grid.
P	pressure (Pa).
P^o	reference pressure (Pa).
P_{gw}^{gw}	gas-water capillary pressure in a gas-water, two-phase system (Pa).
P_w	wellbore or water phase pressure (Pa).
P_β	pressure in phase β ($\beta = w, o$, or g) (Pa).
q	mass rate (kg/s) or volumetric rate (m^3/s) of a phase in a source element.
q_β	mass rate of generation of phase β in a source element (kg/s/ m^3).
Q_β	mass rate of generation of component β ($\beta = w, o$, or g) in a source element (kg/s).
$Q_{\beta,w}$	mass rate of component β ($\beta = w, o$, or g) in a well element (kg/s).
R	universal gas constant (mJ/mole K).
r_e	effective grid block radius (m).
R_i^β	residual term of mass balance of component β ($\beta = w, o$, or g) at element i.
R_s	solution gas-oil ratio (m^3/m^3).
r_w	well radius (m).
s	well skin factor, dimensionless.
S_β	saturation of phase β .
$S_{\beta r}$	residual saturation of phase β .
\bar{S}_g	normalized gas saturation.

\bar{S}_L normalized liquid saturation.

\bar{S}_w normalized water saturation.

t time (seconds).

Δt time step (seconds).

T formation temperature ($^{\circ}\text{C}$).

T^0 reference formation temperature ($^{\circ}\text{C}$).

V_i volume of element i (m^3).

\vec{V}_β Darcy's velocity of phase β (m/s).

v_{dg} volume of dissolved gas (m^3).

v_β volume of phase β (m^3).

$(v_\beta)_{RC}$ volume of a given mass of phase β at reservoir conditions (m^3).

$(v_\beta)_{STC}$ volume occupied by the same mass of phase β at standard conditions (m^3).

x, y, z three Cartesian coordinates with z being in the vertical direction (m).

Z gas Z factor to collaborate real gas density from ideal gas density

Creek Symbols

α_{go} biot factor for effective stress correlation

ϕ effective porosity of formation.

ϕ^0 effective porosity of formation at reference conditions.

γ_{ij}	transmissivity between node i and j [Equation (3.1.5)] (m^3).
$\nabla\Phi$	potential gradient (Pa/m).
$\nabla\Phi_e$	effective potential gradient of a Bingham fluid [Equation (3.3.5)], (Pa/m).
$\nabla\Phi_\beta$	potential gradient of phase β , (Pa/m).
η_i	a set of neighboring nodes of node i.
λ_β	mobility of phase β [Equation (3.1.4)].
μ_{nn}	viscosity of a non-Newtonian fluid (Pa•s).
μ_β	viscosity of phase β (Pa•s).
ρ	density (kg/m^3).
ρ_β	density of phase β at reservoir conditions (kg/m^3).
ρ_R	density of rock grains (kg/m^3).
$(\rho_\beta)_{STC}$	density of phase β at standard condition (or storage tank conditions) (kg/m^3).
σ_{gw}	interfacial tension between gas and water (Pa/m).

Subscript

a	air.
e	effective.
f	fracture or fluid.
g	gas.
i	index of grid block i or initial.
j	index of grid block j.
ij	between two connected grid blocks i and j.
ij+½	appropriate averaging between two grid blocks i and j.

ir	irreducible.
k	primary variable index.
L	liquid.
m	matrix or mass.
max	maximum.
min	minimum.
n	NAPL.
o	oil.
p	Newton iteration level.
r	residual, relative, or rock.
rne	relative to a Newtonian fluid.
rnn	relative to a non-Newtonian fluid.
w	water or well.
x	x-direction.
β	phase β .

SUPERSCRIPT

n	previous time step level.
$n+1$	current time step level.
o	reference condition.
w	well.

x x-coordinate.

β phase β .

REFERENCES CITED

- Ahmed, Usman, M. E. Markley, and S. F. Crary. 1991. "Enhanced In-Situ Stress Profiling With Microfracture, Core, and Sonic-Logging Data." *SPE Formation Evaluation* 6 (02):243–51. <https://doi.org/10.2118/19004-PA>.
- Anders, Mark H., Stephen E. Laubach, and Christopher H. Scholz. 2014. "Microfractures: A Review." *Journal of Structural Geology*, Fluids and Structures in Fold and Thrust Belts with Recognition of the Work of David V. Wiltschko, 69, Part B (December):377–94. <https://doi.org/10.1016/j.jsg.2014.05.011>.
- Bathe, Klaus-Jürgen. 2006. *Finite Element Procedures*. Klaus-Jürgen Bathe.
- Blasingame, Thomas Alwin. 2008. "The Characteristic Flow Behavior of Low-Permeability Reservoir Systems." In . Society of Petroleum Engineers. <https://doi.org/10.2118/114168-MS>.
- Bryant, Ian D., and Stephen S. Flint. 2009. *The Geological Modelling of Hydrocarbon Reservoirs and Outcrop Analogues (Special Publication 15 of the IAS)*. John Wiley & Sons.
- Bui, H. D. 1977. "An Integral Equations Method for Solving the Problem of a Plane Crack of Arbitrary Shape." *Journal of the Mechanics and Physics of Solids* 25 (1):29–39. [https://doi.org/10.1016/0022-5096\(77\)90018-7](https://doi.org/10.1016/0022-5096(77)90018-7).
- Cai, Long, Didier-Yu Ding, Cong Wang, and Yu-Shu Wu. 2015. "Accurate and Efficient Simulation of Fracture–Matrix Interaction in Shale Gas Reservoirs." *Transport in Porous Media* 107 (2):305–20. <https://doi.org/10.1007/s11242-014-0437-x>.
- Chan, S. K., I. S. Tuba, and W. K. Wilson. 1970. "On the Finite Element Method in Linear Fracture Mechanics." *Engineering Fracture Mechanics* 2 (1):1–17. [https://doi.org/10.1016/0013-7944\(70\)90026-3](https://doi.org/10.1016/0013-7944(70)90026-3).
- Chen, Li, Lei Zhang, Qinjun Kang, Jun Yao, and Wenquan Tao. 2015. "Nanoscale Simulation of Shale Transport Properties Using the Lattice Boltzmann Method: Permeability and Diffusivity." *Scientific Reports* 5 (January):8089. <https://doi.org/10.1038/srep08089>.
- Chen, Zuorong. 2013. "An ABAQUS Implementation of the XFEM for Hydraulic Fracture Problems." <https://doi.org/10.5772/56287>.
- Cinco-Ley, H., and H.-Z. Meng. 1988. "Pressure Transient Analysis of Wells With Finite Conductivity Vertical Fractures in Double Porosity Reservoirs." In . Society of Petroleum Engineers. <https://doi.org/10.2118/18172-MS>.
- Cinco-Ley, Heber, and Fernando Samaniego-V. 1981. "Transient Pressure Analysis for Fractured Wells." *Journal of Petroleum Technology* 33 (09):1749–66. <https://doi.org/10.2118/7490-PA>.
- Cipolla, Craig L., Elyezer Lolon, and Michael J. Mayerhofer. 2008. "Resolving Created, Propped and Effective Hydraulic Fracture Length." In . International Petroleum Technology Conference. <https://doi.org/10.2523/IPTC-12147-MS>.
- Civan, Faruk, Chandra S. Rai, and Carl H. Sondergeld. 2010. "Shale-Gas Permeability and Diffusivity Inferred by Improved Formulation of Relevant Retention and Transport

- Mechanisms.” *Transport in Porous Media* 86 (3):925–44. <https://doi.org/10.1007/s11242-010-9665-x>.
- Clifton, Rodney J., and Ahmed S. Abou-Sayed. 1981. “A Variational Approach To The Prediction Of The Three-Dimensional Geometry Of Hydraulic Fractures.” In . Society of Petroleum Engineers. <https://doi.org/10.2118/9879-MS>.
- Crosdale, Peter J., B. Basil Beamish, and Marjorie Valix. 1998. “Coalbed Methane Sorption Related to Coal Composition.” *International Journal of Coal Geology* 35 (1–4):147–58. [https://doi.org/10.1016/S0166-5162\(97\)00015-3](https://doi.org/10.1016/S0166-5162(97)00015-3).
- Curtis, Mark E., Brian J. Cardott, Carl H. Sondergeld, and Chandra S. Rai. 2012. “Development of Organic Porosity in the Woodford Shale with Increasing Thermal Maturity.” *International Journal of Coal Geology*, Shale Gas and Shale Oil Petrology and Petrophysics, 103 (December):26–31. <https://doi.org/10.1016/j.coal.2012.08.004>.
- Davis, Philip J., and Philip Rabinowitz. 2007. *Methods of Numerical Integration*. Courier Corporation.
- Detournay, E. 1999. “Fluid and Solid Singularities at the Tip of a Fluid-Driven Fracture.” In *IUTAM Symposium on Non-Linear Singularities in Deformation and Flow*, 27–42. Springer, Dordrecht. https://doi.org/10.1007/978-94-011-4736-1_4.
- Ding, Didier Yu, Y.-S. Wu, Nicolas Farah, Cong Wang, and Bernard Bourbiaux. 2014. “Numerical Simulation of Low Permeability Unconventional Gas Reservoirs.” In *SPE/EAGE European Unconventional Resources Conference and Exhibition*. <http://www.earthdoc.org/publication/publicationdetails/?publication=75116>.
- Donovan, Arthur D., T. Scott Staerker, Aris Pramudito, Weiguo Li, Matthew J. Corbett, Christopher M. Lowery, Andrea Miceli Romero, and Rand D. Gardner. 2012. “The Eagle Ford Outcrops of West Texas: A Laboratory for Understanding Heterogeneities within Unconventional Mudstone Reservoirs.” <http://archives.datapages.com/data/gcags-journal/data/001/001001/pdfs/162.htm>.
- Duguid, James O., and P. C. Y. Lee. 1977. “Flow in Fractured Porous Media.” *Water Resources Research* 13 (3):558–66. <https://doi.org/10.1029/WR013i003p00558>.
- EIA, US. 2011. “Review of Emerging Resources: US Shale Gas and Shale Oil Plays.” *Government. US Energy Information Administration. Http://205.254.135*.
- Fakcharoenphol, Perapon, Mehmet Ali Torcuk, Jon Wallace, Antoine Bertoncello, Hossein Kazemi, Yu-Shu Wu, Matt Honarpour, and others. 2013. “Managing Shut-in Time to Enhance Gas Flow Rate in Hydraulic Fractured Shale Reservoirs: A Simulation Study.” In *SPE Annual Technical Conference and Exhibition*. Society of Petroleum Engineers. <https://www.onepetro.org/conference-paper/SPE-166098-MS>.
- Farah, Nicolas, Didier-Yu Ding, and Yu-Shu Wu. 2017. “Simulation of the Impact of Fracturing-Fluid-Induced Formation Damage in Shale Gas Reservoirs.” *SPE Reservoir Evaluation & Engineering* 20 (03):532–46. <https://doi.org/10.2118/173264-PA>.
- Fisher, M. K., J. R. Heinze, C. D. Harris, B. M. Davidson, C. A. Wright, and K. P. Dunn. 2004. “Optimizing Horizontal Completion Techniques in the Barnett Shale Using Microseismic Fracture Mapping.” In . Society of Petroleum Engineers. <https://doi.org/10.2118/90051-MS>.

- Fisher, M. Kevin, and Norman R. Warpinski. 2012. "Hydraulic-Fracture-Height Growth: Real Data." *SPE Production & Operations* 27 (01):8–19. <https://doi.org/10.2118/145949-PA>.
- Gale, Julia F. W., Robert M. Reed, and Jon Holder. 2007. "Natural Fractures in the Barnett Shale and Their Importance for Hydraulic Fracture Treatments." *AAPG Bulletin* 91 (4):603–22. <https://doi.org/10.1306/11010606061>.
- Geertsma, J., and F. De Klerk. 1969. "A Rapid Method of Predicting Width and Extent of Hydraulically Induced Fractures." *Journal of Petroleum Technology* 21 (12):1,571-1,581. <https://doi.org/10.2118/2458-PA>.
- Geilikman, M. B., Sau-Wai Wong, and J. M. Karanikas. 2015. "Growth of Fractured Zone Around Hydraulic Fracture." In . Society of Petroleum Engineers. <https://doi.org/10.2118/175921-MS>.
- Gringarten, Alain C., Henry J. Ramey, and R. Raghavan. 1974. "Unsteady-State Pressure Distributions Created by a Well With a Single Infinite-Conductivity Vertical Fracture." *Society of Petroleum Engineers Journal* 14 (04):347–60. <https://doi.org/10.2118/4051-PA>.
- Gu, Hongren, and Ching H. Yew. 1988. "Finite Element Solution of a Boundary Integral Equation for Mode I Embedded Three-Dimensional Fractures." *International Journal for Numerical Methods in Engineering* 26 (7):1525–40. <https://doi.org/10.1002/nme.1620260705>.
- Gu, Xin, David F. R. Mildner, David R. Cole, Gernot Rother, Rudy Slingerland, and Susan L. Brantley. 2016. "Quantification of Organic Porosity and Water Accessibility in Marcellus Shale Using Neutron Scattering." *Energy & Fuels* 30 (6):4438–49. <https://doi.org/10.1021/acs.energyfuels.5b02878>.
- Hale, Brent W., and J. F. Evers. 1981. "Elliptical Flow Equations for Vertically Fractured Gas Wells." *Journal of Petroleum Technology* 33 (12):2,489-2,497. <https://doi.org/10.2118/8943-PA>.
- Hart, B., J. Macquaker, and K. Taylor. 2013. "Mudstone ('Shale') Depositional and Diagenetic Processes: Implications for Seismic Analyses of Source-Rock Reservoirs." *Interpretation* 1 (1):B7–26. <https://doi.org/10.1190/INT-2013-0003.1>.
- Heckbert, Paul S. 1994. *Graphics Gems IV*. Morgan Kaufmann.
- Howard, George C., and C. R. Fast. 1957. "Optimum Fluid Characteristics for Fracture Extension." In . American Petroleum Institute. <https://www.onepetro.org/conference-paper/API-57-261>.
- Hu, Litang, Philip H. Winterfeld, Perapon Fakcharoenphol, and Yu-Shu Wu. 2013. "A Novel Fully-Coupled Flow and Geomechanics Model in Enhanced Geothermal Reservoirs." *Journal of Petroleum Science and Engineering* 107 (July):1–11. <https://doi.org/10.1016/j.petrol.2013.04.005>.
- Hui, Mun-Hong, Bin Gong, Mohammad Karimi-Fard, and Louis J. Durlofsky. 2007. "Development and Application of New Computational Procedures for Modeling Miscible Gas Injection in Fractured Reservoirs." In . Society of Petroleum Engineers. <https://doi.org/10.2118/109686-MS>.
- Huy, Phung Quoc, Kyuro Sasaki, Yuichi Sugai, and Satoshi Ichikawa. 2010. "Carbon Dioxide Gas Permeability of Coal Core Samples and Estimation of Fracture Aperture Width."

- Javadpour, F., D. Fisher, and M. Unsworth. 2007. "Nanoscale Gas Flow in Shale Gas Sediments." *Journal of Canadian Petroleum Technology* 46 (10). <https://doi.org/10.2118/07-10-06>.
- Jeffrey, Robert G., and Andrew Bunker. 2009. "A Detailed Comparison of Experimental and Numerical Data on Hydraulic Fracture Height Growth Through Stress Contrasts." *SPE Journal* 14 (03):413–22. <https://doi.org/10.2118/106030-PA>.
- Karimi-Fard, M., L. J. Durlofsky, and K. Aziz. 2004. "An Efficient Discrete-Fracture Model Applicable for General-Purpose Reservoir Simulators." *SPE Journal* 9 (02):227–36. <https://doi.org/10.2118/88812-PA>.
- Kazemi, H. 1969. "Pressure Transient Analysis of Naturally Fractured Reservoirs with Uniform Fracture Distribution." *Society of Petroleum Engineers Journal* 9 (04):451–62. <https://doi.org/10.2118/2156-A>.
- Kim, Jong-Gyun, and Milind D. Deo. 2000. "Finite Element, Discrete-Fracture Model for Multiphase Flow in Porous Media." *AIChE Journal* 46 (6):1120–30. <https://doi.org/10.1002/aic.690460604>.
- Klinkenberg, L. J., and others. 1941. "The Permeability of Porous Media to Liquids and Gases." In *Drilling and Production Practice*. American Petroleum Institute. <https://www.onepetro.org/conference-paper/API-41-200>.
- Langmuir, Irving. 1918. "THE ADSORPTION OF GASES ON PLANE SURFACES OF GLASS, MICA AND PLATINUM." *Journal of the American Chemical Society* 40 (9):1361–1403. <https://doi.org/10.1021/ja02242a004>.
- Lecampion, Brice. 2009. "An Extended Finite Element Method for Hydraulic Fracture Problems." *Communications in Numerical Methods in Engineering* 25 (2):121–33. <https://doi.org/10.1002/cnm.1111>.
- Lee, S. H., M. F. Lough, and C. L. Jensen. 2001. "Hierarchical Modeling of Flow in Naturally Fractured Formations with Multiple Length Scales." *Water Resources Research* 37 (3):443–55. <https://doi.org/10.1029/2000WR900340>.
- Li, Liyong, and Seong H. Lee. 2008. "Efficient Field-Scale Simulation of Black Oil in a Naturally Fractured Reservoir Through Discrete Fracture Networks and Homogenized Media." *SPE Reservoir Evaluation & Engineering* 11 (04):750–58. <https://doi.org/10.2118/103901-PA>.
- Liang, Feng, Mohammed Sayed, Ghaitan A. Al-Muntasher, Frank F. Chang, and Leiming Li. 2016. "A Comprehensive Review on Proppant Technologies." *Petroleum* 2 (1):26–39. <https://doi.org/10.1016/j.petlm.2015.11.001>.
- Lisjak, A., O. K. Mahabadi, B. S. A. Tatone, K. Alruwaili, G. D. Couples, J. Ma. J., and A. Al-Nakhli. 2015. "3D Simulation of Fluid-Pressure-Induced Fracture Nucleation and Growth in Rock Samples." In . American Rock Mechanics Association. <https://www.onepetro.org/conference-paper/ARMA-2015-299>.
- Loucks, Robert G., Robert M. Reed, Stephen C. Ruppel, and Ursula Hammes. 2012. "Spectrum of Pore Types and Networks in Mudrocks and a Descriptive Classification for Matrix-Related Mudrock Pores." *AAPG Bulletin* 96 (6):1071–98. <https://doi.org/10.1306/08171111061>.

- Loucks, Robert G., Robert M. Reed, Stephen C. Ruppel, and Daniel M. Jarvie. 2009. "Morphology, Genesis, and Distribution of Nanometer-Scale Pores in Siliceous Mudstones of the Mississippian Barnett Shale." *Journal of Sedimentary Research* 79 (12):848–61.
- Mengal, Salman Akram, and Robert A. Wattenbarger. 2011. "Accounting For Adsorbed Gas in Shale Gas Reservoirs." In . Society of Petroleum Engineers. <https://doi.org/10.2118/141085-MS>.
- Minkoff, Susan E., C. Mike Stone, Steve Bryant, Małgorzata Peszynska, and Mary F. Wheeler. 2003. "Coupled Fluid Flow and Geomechanical Deformation Modeling." *Journal of Petroleum Science and Engineering* 38 (1–2):37–56. [https://doi.org/10.1016/S0920-4105\(03\)00021-4](https://doi.org/10.1016/S0920-4105(03)00021-4).
- Moës, Nicolas, John Dolbow, and Ted Belytschko. 1999. "A Finite Element Method for Crack Growth without Remeshing." *International Journal for Numerical Methods in Engineering* 46 (1):131–50. [https://doi.org/10.1002/\(SICI\)1097-0207\(19990910\)46:1<131::AID-NME726>3.0.CO;2-J](https://doi.org/10.1002/(SICI)1097-0207(19990910)46:1<131::AID-NME726>3.0.CO;2-J).
- Moinfar, Ali, Abdoljalil Varavei, Kamy Sepehrnoori, and Russell T. Johns. 2014a. "Development of an Efficient Embedded Discrete Fracture Model for 3D Compositional Reservoir Simulation in Fractured Reservoirs." *SPE Journal* 19 (02):289–303. <https://doi.org/10.2118/154246-PA>.
- Moridis, George J., Thomas Alwin Blasingame, and Craig Matt Freeman. 2010. "Analysis of Mechanisms of Flow in Fractured Tight-Gas and Shale-Gas Reservoirs." In . Society of Petroleum Engineers. <https://doi.org/10.2118/139250-MS>.
- Narasimhan, T. N., and P. A. Witherspoon. 1976. "An Integrated Finite Difference Method for Analyzing Fluid Flow in Porous Media." *Water Resources Research* 12 (1):57–64. <https://doi.org/10.1029/WR012i001p00057>.
- Nelson, Philip H. 2009. "Pore-Throat Sizes in Sandstones, Tight Sandstones, and Shales." *AAPG Bulletin* 93 (3):329–40. <https://doi.org/10.1306/10240808059>.
- Neuman, Shlomo P. 2005. "Trends, Prospects and Challenges in Quantifying Flow and Transport through Fractured Rocks." *Hydrogeology Journal* 13 (1):124–47. <https://doi.org/10.1007/s10040-004-0397-2>.
- Olson, Jon Edward, and Arash Dahi Taleghani. 2009. "Modeling Simultaneous Growth of Multiple Hydraulic Fractures and Their Interaction with Natural Fractures." In . Society of Petroleum Engineers. <https://doi.org/10.2118/119739-MS>.
- Pais, Matthew. 2011. "MATLAB Extended Finite Element (MxFEM) Code v1.2." *Www.Matthewpais.Com*.
- Pais, Matthew, Nam-Ho Kim, and Timothy Davis. n.d. "Reanalysis of the Extended Finite Element Method for Crack Initiation and Propagation." In *51st AIAA/ASME/ASCE/AHS/ASC Structures, Structural Dynamics, and Materials Conference*. American Institute of Aeronautics and Astronautics. Accessed October 30, 2017. <https://doi.org/10.2514/6.2010-2536>.
- Paris, P., and F. Erdogan. 1963. "A Critical Analysis of Crack Propagation Laws." *Journal of Basic Engineering* 85 (4):528–33. <https://doi.org/10.1115/1.3656900>.

- Passey, Quinn R., Kevin Bohacs, William Lee Esch, Robert Klimentidis, and Somnath Sinha. 2010. "From Oil-Prone Source Rock to Gas-Producing Shale Reservoir - Geologic and Petrophysical Characterization of Unconventional Shale Gas Reservoirs." In . Society of Petroleum Engineers. <https://doi.org/10.2118/131350-MS>.
- Peaceman, D.W. 1978. "Interpretation of Well-Block Pressures in Numerical Reservoir Simulation(Includes Associated Paper 6988)." *Society of Petroleum Engineers Journal* 18 (03):183–94. <https://doi.org/10.2118/6893-PA>.
- Perkins, T. K., and L. R. Kern. 1961. "Widths of Hydraulic Fractures." *Journal of Petroleum Technology* 13 (09):937–49. <https://doi.org/10.2118/89-PA>.
- Pruess, K., C. M. Oldenburg, and G. J. Moridis. 1999. "TOUGH2 User's Guide Version 2." *Lawrence Berkeley National Laboratory*, November. <http://escholarship.org/uc/item/4df6700h>.
- Pruess, Karsten. 1985. "A Practical Method for Modeling Fluid and Heat Flow in Fractured Porous Media." *Society of Petroleum Engineers Journal* 25 (01):14–26. <https://doi.org/10.2118/10509-PA>.
- Pruess, Karsten. 2004. "The TOUGH Codes—a Family of Simulation Tools for Multiphase Flow and Transport Processes in Permeable Media." *Vadose Zone Journal* 3 (3):738–746.
- Pruess, Karsten, C. M. Oldenburg, and G. J. Moridis. 1999. "TOUGH2 User's Guide Version 2." *Lawrence Berkeley National Laboratory*. <http://escholarship.org/uc/item/4df6700h.pdf>.
- Roy, Subrata, Reni Raju, Helen F. Chuang, Brett A. Cruden, and M. Meyyappan. 2003. "Modeling Gas Flow through Microchannels and Nanopores." *Journal of Applied Physics* 93 (8):4870–79. <https://doi.org/10.1063/1.1559936>.
- Rubin, Barry. 2010. "Accurate Simulation of Non Darcy Flow in Stimulated Fractured Shale Reservoirs." In . Society of Petroleum Engineers. <https://doi.org/10.2118/132093-MS>.
- Rutqvist, J., Y.-S. Wu, C.-F. Tsang, and G. Bodvarsson. 2002. "A Modeling Approach for Analysis of Coupled Multiphase Fluid Flow, Heat Transfer, and Deformation in Fractured Porous Rock." *International Journal of Rock Mechanics and Mining Sciences* 39 (4):429–442.
- Sadrpanah, Hooman, Thierry Charles, and Jonathan Fulton. 2006. "Explicit Simulation of Multiple Hydraulic Fractures in Horizontal Wells." In . Society of Petroleum Engineers. <https://doi.org/10.2118/99575-MS>.
- Salimzadeh, Saeed, Adriana Paluszny, and Robert W. Zimmerman. 2017. "Three-Dimensional Poroelastic Effects during Hydraulic Fracturing in Permeable Rocks." *International Journal of Solids and Structures* 108 (Supplement C):153–63. <https://doi.org/10.1016/j.ijsolstr.2016.12.008>.
- Savitski, A. A., and E. Detournay. 2002. "Propagation of a Penny-Shaped Fluid-Driven Fracture in an Impermeable Rock: Asymptotic Solutions." *International Journal of Solids and Structures* 39 (26):6311–37. [https://doi.org/10.1016/S0020-7683\(02\)00492-4](https://doi.org/10.1016/S0020-7683(02)00492-4).
- Shi, Fang, XiaoLong Wang, Chuang Liu, He Liu, and HengAn Wu. 2016. "A Coupled Extended Finite Element Approach for Modeling Hydraulic Fracturing in Consideration of Proppant."

- Journal of Natural Gas Science and Engineering* 33 (Supplement C):885–97. <https://doi.org/10.1016/j.jngse.2016.06.031>.
- Shih, C. F., and R. J. Asaro. 1988. “Elastic-Plastic Analysis of Cracks on Bimaterial Interfaces: Part I—Small Scale Yielding.” *Journal of Applied Mechanics* 55 (2):299–316. <https://doi.org/10.1115/1.3173676>.
- Shlyapobersky, J. 1985. “Energy Analysis Of Hydraulic Fracturing.” In . American Rock Mechanics Association. <https://www.onepetro.org/conference-paper/ARMA-85-0539-1>.
- Simonson, E. R., A. S. Abou-Sayed, and R. J. Clifton. 1978. “Containment of Massive Hydraulic Fractures.” *Society of Petroleum Engineers Journal* 18 (01):27–32. <https://doi.org/10.2118/6089-PA>.
- Slough, K. J., E. A. Sudicky, and P. A. Forsyth. 1999. “Grid Refinement for Modeling Multiphase Flow in Discretely Fractured Porous Media.” *Advances in Water Resources* 23 (3):261–69. [https://doi.org/10.1016/S0309-1708\(99\)00009-3](https://doi.org/10.1016/S0309-1708(99)00009-3).
- Smith, I. M., D. V. Griffiths, and L. Margetts. 2013. *Programming the Finite Element Method*. John Wiley & Sons.
- Soulaine, Cyprien. n.d. “On the Origin of Darcy’s Law.” Accessed October 24, 2016. http://web.stanford.edu/~csoulain/PORE_SCALE/Chap1_Darcy.pdf.
- Sukumar, N., D. L. Chopp, N. Moës, and T. Belytschko. 2001. “Modeling Holes and Inclusions by Level Sets in the Extended Finite-Element Method.” *Computer Methods in Applied Mechanics and Engineering* 190 (46):6183–6200. [https://doi.org/10.1016/S0045-7825\(01\)00215-8](https://doi.org/10.1016/S0045-7825(01)00215-8).
- Sukumar, N., N. Moës, B. Moran, and T. Belytschko. 2000. “Extended Finite Element Method for Three-Dimensional Crack Modelling.” *International Journal for Numerical Methods in Engineering* 48 (11):1549–70. [https://doi.org/10.1002/1097-0207\(20000820\)48:11<1549::AID-NME955>3.0.CO;2-A](https://doi.org/10.1002/1097-0207(20000820)48:11<1549::AID-NME955>3.0.CO;2-A).
- Sun, Jianlei, and David Stuart Schechter. 2014. “Optimization-Based Unstructured Meshing Algorithms for Simulation of Hydraulically and Naturally Fractured Reservoirs with Variable Distribution of Fracture Aperture, Spacing, Length and Strike.” In . Society of Petroleum Engineers. <https://doi.org/10.2118/170703-MS>.
- Tada, Hiroshi, Paul C. Paris, and George R. Irwin. 2000. *The Stress Analysis of Cracks Handbook, Third Edition*. Three Park Avenue New York, NY 10016-5990: ASME. <https://doi.org/10.1115/1.801535>.
- Walton, Ian, and John McLennan. 2013. “The Role of Natural Fractures in Shale Gas Production.” In . International Society for Rock Mechanics. <https://www.onepetro.org/conference-paper/ISRM-ICHF-2013-046>.
- Wang, Chenchen, Jun Yao, Keliu Wu, Guoxuan Ren, Hai Sun, Yongfei Yang, Ying Gao, and Zhangxin Chen. 2014. “Organic and Inorganic Pore Structure Analysis in Shale Matrix with Superposition Method.” In . Society of Petroleum Engineers. <https://doi.org/10.15530/urtec-2014-1922283>.
- Wang, Cong. 2013. “Pressure Transient Analysis of Fractured Wells in Shale Reservoirs.” COLORADO SCHOOL OF MINES. <http://gradworks.umi.com/15/44/1544672.html>.

- Wang, Cong, Xiaoping Mao, and Yu-Shu Wu. 2017. "A General Three-Dimensional Embedded Discrete Fracture Method for Reservoir Simulation with Complicated Hydraulic Fractures." *SPE Journal*.
- Wang, Cong, and Yushu Wu. 2015. "Characterizing Hydraulic Fractures in Shale Gas Reservoirs Using Transient Pressure Tests." *Petroleum* 1 (2):133–38. <https://doi.org/10.1016/j.petlm.2015.05.002>.
- Wang, Fred P., and Rob M. Reed. 2009. "Pore Networks and Fluid Flow in Gas Shales." In . Society of Petroleum Engineers. <https://doi.org/10.2118/124253-MS>.
- Wang, Moran, Jinku Wang, Ning Pan, and Shiyi Chen. 2007. "Mesoscopic Predictions of the Effective Thermal Conductivity for Microscale Random Porous Media." *Physical Review E* 75 (3):036702. <https://doi.org/10.1103/PhysRevE.75.036702>.
- Warren, J. E., and P. J. Root. 1963. "The Behavior of Naturally Fractured Reservoirs." *Society of Petroleum Engineers Journal* 3 (03):245–55. <https://doi.org/10.2118/426-PA>.
- Wattenbarger, Robert A., Ahmed H. El-Banbi, Mauricio E. Villegas, and J. Bryan Maggard. 1998. "Production Analysis of Linear Flow Into Fractured Tight Gas Wells." In . Society of Petroleum Engineers. <https://doi.org/10.2118/39931-MS>.
- Wong, Sau-Wai, Mikhail Geilikman, and Guanshui Xu. 2013. "Interaction of Multiple Hydraulic Fractures in Horizontal Wells." In . Society of Petroleum Engineers. <https://doi.org/10.2118/163982-MS>.
- Wu, Y. S. 1998. "MSFLOW: Multiphase Subsurface Flow Model of Oil, Gas and Water in Porous and Fractured Media with Water Shut-off Capability, DOCUMENTATION and User's Guide." *Twange Int., Houston, Tex., Walnut Creek, Calif.*
- Wu, Yu-Shu. 2000. "A Virtual Node Method for Handling Well Bore Boundary Conditions in Modeling Multiphase Flow in Porous and Fractured Media." *Water Resources Research* 36 (3):807–14. <https://doi.org/10.1029/1999WR900336>.
- Wu, Yu-Shu. 2002. "Numerical Simulation of Single-Phase and Multiphase Non-Darcy Flow in Porous and Fractured Reservoirs." *Transport in Porous Media* 49 (2):209–40. <https://doi.org/10.1023/A:1016018020180>.
- Wu, Yu-Shu. 2015. "Multiphase Fluid Flow in Porous and Fractured Reservoirs - 1st Edition." 2015. <https://www.elsevier.com/books/multiphase-fluid-flow-in-porous-and-fractured-reservoirs/wu/978-0-12-803848-2>.
- Wu, Yu-Shu, Jianfang Li, Didier Ding, Cong Wang, Yuan Di, and others. 2014. "A Generalized Framework Model for the Simulation of Gas Production in Unconventional Gas Reservoirs." *SPE Journal* 19 (05):845–857.
- Wu, Yu-Shu, H. H. Liu, and G. S. Bodvarsson. 2004. "A Triple-Continuum Approach for Modeling Flow and Transport Processes in Fractured Rock." *Journal of Contaminant Hydrology* 73 (1–4):145–79. <https://doi.org/10.1016/j.jconhyd.2004.01.002>.
- Wu, Yu-Shu, and Karsten Pruess. 1988. "A Multiple-Porosity Method for Simulation of Naturally Fractured Petroleum Reservoirs." *SPE Reservoir Engineering* 3 (01):327–36. <https://doi.org/10.2118/15129-PA>.

- Xiong, Yi, Phil Winterfeld, Cong Wang, Zhaoqin Huang, and Yu-Shu Wu. 2015. "Effect of Large Capillary Pressure on Fluid Flow and Transport in Stress-Sensitive Tight Oil Reservoirs." In . Society of Petroleum Engineers. <https://doi.org/10.2118/175074-MS>.
- Xiong, Yi, Philip H. Winterfeld, Cong Wang, Yu-Shu Wu, Zhao-Qin Huang, and others. 2015. "A Compositional Model Fully Coupled with Geomechanics for Liquid-Rich Shale and Tight Oil Reservoir Simulation." In *SPE Reservoir Simulation Symposium*. Society of Petroleum Engineers. <https://www.onepetro.org/conference-paper/SPE-173261-MS>.
- Xu, G., and M. Ortiz. 1993. "A Variational Boundary Integral Method for the Analysis of 3-D Cracks of Arbitrary Geometry Modelled as Continuous Distributions of Dislocation Loops." *International Journal for Numerical Methods in Engineering* 36 (21):3675–3701. <https://doi.org/10.1002/nme.1620362107>.
- Xu, M., and H. Dehghanpour. 2014. "Advances in Understanding Wettability of Gas Shales." *Energy & Fuels* 28 (7):4362–75. <https://doi.org/10.1021/ef500428y>.
- Yan, Bicheng, Yuhe Wang, and John E. Killough. 2016. "Beyond Dual-Porosity Modeling for the Simulation of Complex Flow Mechanisms in Shale Reservoirs." *Computational Geosciences* 20 (1):69–91. <https://doi.org/10.1007/s10596-015-9548-x>.
- Yan, Xia, Zhaoqin Huang, Jun Yao, Yang Li, and Dongyan Fan. 2016. "An Efficient Embedded Discrete Fracture Model Based on Mimetic Finite Difference Method." *Journal of Petroleum Science and Engineering* 145 (September):11–21. <https://doi.org/10.1016/j.petrol.2016.03.013>.
- Yang, Feng, Zhengfu Ning, Qing Wang, Rui Zhang, and Bernhard M. Krooss. 2016. "Pore Structure Characteristics of Lower Silurian Shales in the Southern Sichuan Basin, China: Insights to Pore Development and Gas Storage Mechanism." *International Journal of Coal Geology* 156 (February):12–24. <https://doi.org/10.1016/j.coal.2015.12.015>.
- Yew, Ching H., and Xiaowei Weng. 2014. *Mechanics of Hydraulic Fracturing*. Gulf Professional Publishing.
- Youn, Dong Joon. 2016. "Hydro-Mechanical Coupled Simulation of Hydraulic Fracturing Using the Extended Finite Element Method (XFEM)." Thesis, Colorado School of Mines. Arthur Lakes Library. <https://dspace.library.colostate.edu/handle/11124/170324>.
- Yu, Xin, Jim Rutledge, Scott Leaney, and Shawn Maxwell. 2016. "Discrete-Fracture-Network Generation From Microseismic Data by Use of Moment-Tensor- and Event-Location-Constrained Hough Transforms." *SPE Journal* 21 (01):221–32. <https://doi.org/10.2118/168582-PA>.
- Zhai, Zongyu, and Ernesto Fonseca. 2015. "History Match Case Study With a Multi-Cluster & Multi-Well Hydraulic Fracture Modeling Tool." <http://archives.datapages.com/data/urtec/2015/2153981.htm>.
- Zhang, Ronglei, Xiaolong Yin, Philip H. Winterfeld, and Yu-Shu Wu. 2016. "A Fully Coupled Thermal-Hydrological-Mechanical-Chemical Model for CO₂ Geological Sequestration." *Journal of Natural Gas Science and Engineering* 28 (January):280–304. <https://doi.org/10.1016/j.jngse.2015.11.037>.
- Zhang, Tongwei, Geoffrey S. Ellis, Stephen C. Ruppel, Kitty Milliken, and Rongsheng Yang. 2012. "Effect of Organic-Matter Type and Thermal Maturity on Methane Adsorption in Shale-

- Gas Systems.” *Organic Geochemistry* 47 (June):120–31. <https://doi.org/10.1016/j.orggeochem.2012.03.012>.
- Zhang, Wen-Ming, Guang Meng, and Xueyong Wei. 2012. “A Review on Slip Models for Gas Microflows.” *Microfluidics and Nanofluidics* 13 (6):845–82. <https://doi.org/10.1007/s10404-012-1012-9>.
- Zheltov, A. Khristianovic. 1955. “3. Formation of Vertical Fractures by Means of Highly Viscous Liquid.” In . World Petroleum Congress. <https://www.onepetro.org/conference-paper/WPC-6132>.
- Zhou, Jing. 2016. “Hydraulic Fracture Propagation Modeling and Data-Based Fracture Identification.” Ph.D., United States -- Utah: The University of Utah. <http://search.proquest.com/docview/1803936953/abstract/A26A78B0038349D6PQ/1>.
- Zhou, Zhou, B. Todd Hoffman, Doug Bearinger, and Xiaopeng Li. 2014. “Experimental and Numerical Study on Spontaneous Imbibition of Fracturing Fluids in Shale Gas Formation.” In . Society of Petroleum Engineers. <https://doi.org/10.2118/171600-MS>.

APPENDIX A: THE CODE STRUCTURE OF THE EDFM AND X-FEM COUPLING

